Degree Project in Engineering Material Science

Second Cycle, 30 credits

Numerical Investigation of Initial filling in Ingot Casting

Focusing on Uphill Teeming in an Octagonal Mould

DIGANTA GAUTAM

TRITA – ITM-EX 2026:345
Stockholm, Sweden 2026

www.kth.se

Abstract

The design and optimisation of gating systems play a crucial role in ensuring the metallurgical quality of cast components. This thesis presents a transient CFD investigation of the initial mould-filling stage in a large-scale, industrial-geometry uphill (bottom-poured) ingot casting system, using the Volume of Fluid (VOF) method implemented in the OpenFOAM framework. A parametric study was conducted across eight runner-entry angles (90°– 45°) and a range of inlet velocities (1.5– 4.0 m/s) on the 90° baseline, characterising free-surface stability, air entrainment, wall shear stress, and dead-zone formation throughout the first 150 mm of mould rise.

The results reveal a strongly non-monotonic relationship between runner angle and flow stability. Contrary to the expectation that progressively steeper angling would yield steadily better performance, the study identifies a severe hydrodynamic anomaly the 55° violence peak where direct jet impingement on the mould wall drives splashing intensity (M4) and wall shear stress to 425.77 mm and 1763 Pa respectively. In contrast, a 45° runner configuration emerges as the clear optimum, reducing the final dead-zone volume by 40.1% relative to the 90° baseline (28.60% vs. 47.76%) while keeping peak wall shear stress within an acceptable range (741 Pa). A velocity sensitivity study on the 90° baseline further establishes a practical operating limit of approximately 3.0 m/s, beyond which splashing and wall erosion increase sharply due to the cubic scaling of kinetic energy flux.

To ensure that the numerical predictions are relatively free from spatial meshing effects, a systematic three-level (Coarse/Medium/Fine) mesh sensitivity study was conducted. Across all grid levels, high geometric cell quality was maintained, keeping average non-orthogonality below 5.2° and maximum skewness to approximately 2.58. A Grid Convergence Index (GCI) analysis confirmed that the solutions exhibit low sensitivity to grid resolution, bounding the spatial discretisation uncertainties to 9.83% for the stagnant dead zone and 7.13% for the theoretical filling height at the fine mesh level. Overall, this study establishes a consistent computational framework and a set of quantitative design guidelines identifying a preferred runner geometry, a practical velocity operating window, and an explicit angle range to avoid that can directly support gating system optimisation in industrial ingot casting

---

Keywords: Computational Fluid Dynamics (CFD), OpenFOAM, Volume of Fluid (VOF), Runner Angle Optimization, Grid Convergence Index (GCI), Surface Topography, Wall Shear Stress, Gating System Design.

Sammanfattning

Utformningen och optimeringen av ingjutningssystem spelar en avgörande roll för att säkerställa den metallurgiska kvaliteten hos gjutna komponenter. Detta examensarbete presenterar en högupplöst, transient CFD-undersökning av det initiala formfyllnadsskedet i ett storskaligt system för undergjutning (stigande gjutning) av göt med industriell geometri, med hjälp av Volume of Fluid-metoden (VOF) implementerad i beräkningsmiljön OpenFOAM. En parametrisk studie genomfördes över åtta inloppsvinklar (90°– 45°) och ett intervall av inloppshastigheter (1,5– 4,0 m/s) på 90°-baslinjen, i syfte att karaktärisera friytans stabilitet, luftmedryckning, väggskjuvspänning samt bildning av döda zoner under de första 150 mm av formstigningen.

Resultaten påvisar ett starkt icke-monotont samband mellan inloppsvinkel och flödesstabilitet. I motsats till förväntningen att en gradvis skarpare vinkling skulle ge kontinuerligt förbättrad prestanda, identifierar studien en kraftig hydrodynamisk anomali 55°-våldstoppen där direkt strålpåverkan mot formväggen driver stänkintensiteten (M4) och väggskjuvspänningen till 425,77 mm respektive 1763 Pa. Däremot framstår en 45°-konfiguration som det tydliga optimumet, vilket minskar den slutliga dödzonsvolymen med 40,1 % i förhållande till 90°-baslinjen (28,60 % mot 47,76 %) samtidigt som den maximala väggskjuvspänningen hålls inom ett acceptabelt intervall (741 Pa). En känslighetsstudie av inloppshastigheten på 90°-baslinjen fastställer vidare en praktisk driftgräns vid cirka 3,0 m/s, över vilken stänk och väggerosion ökar kraftigt till följd av den kubiska skalningen av kinetiskt energiflöde.

En systematisk nätkänslighetsstudie med tre nätupplösningar (grovt, medelgrovt och fint) genomfördes för att säkerställa numerisk tillförlitlighet. Den genomsnittliga icke-ortogonaliteten understeg 5,2° och den maximala skevheten var cirka 2,58. GCI-analysen visade att diskretiseringsosäkerheten vid den finaste nätupplösningen var 9,83 % för den stagnerande zonen och 7,13 % för den teoretiska fyllnadshöjden. Studien ger kvantitativa konstruktionsriktlinjer för löpargeometri, driftshastighet och vinkelintervall för att optimera ingjutningssystem vid industriell götgjutning.

Nyckelord: Numerisk strömningsmekanik (CFD), OpenFOAM, Volume of Fluid (VOF), Optimering av inloppsvinkel, Grid Convergence Index (GCI), Yttopografi, Väggskjuvspänning, Utformning av ingjutningssystem.

Acknowledgments

I would like to express my profound gratitude to my supervisors, Yu-Chiao Lu and Mikael Ersson, for their exceptional guidance throughout this research. I am deeply thankful to Yu-Chiao Lu for her dedicated thesis support; her academic insight and structural guidance were instrumental in shaping the direction of this project. My sincere thanks go to Mikael for providing intense technical support. His deep expertise in numerical modelling was indispensable, helping me navigate the most rigorous technical hurdles and ensuring the accuracy of the complex simulations that form the core of this work.

The environment in which this thesis was written played a vital role in its completion, and I am grateful to the libraries at KTH and SU for their environmental support. These spaces provided the necessary quiet and resources for deep focus and academic growth. On a personal note, I owe an immeasurable debt to my family. To my mom and sister, thank you for the unwavering moral support that fortified my resolve when the challenges seemed insurmountable.

Finally, I want to thank those who supported me beyond the academic sphere. I am truly grateful to my bandmates for their camaraderie and support during the hard times; our sessions provided the perfect creative outlet to recharge my energy. Most importantly, I want to thank my partner. Your support for my health, peace, and clarity was the foundation upon which this achievement was built.

Table of Content

Chapter 1: Introduction ---- 1

1.1 The Global Scale of Ingot Casting ---- 2

1.2 Problem Definition ---- 3

1.2.1 Delivery System and Hydraulic Issues ---- 4

1.2.2 Initial Filling Disturbances ---- 4

1.2.3 Issues Specific to Octagonal Moulds ---- 4

1.3 Technical Challenges in Initial Filling ---- 5

1.3.1 Issues with Current Uphill Ingot Casting ---- 5

1.3.2 Importance of the Initial Filling Stage ---- 5

Chapter 2: Literature Review ---- 6

2.1 Types of Ingot Casting and Industrial Utilization ---- 6

2.2 Mechanics of the Trumpet and Runner System ---- 8

2.2.1 Role of Trumpet-Runner Geometry in Flow Control ---- 8

2.2.2 Role of the Mould Flux in Flow Control ---- 8

2.2.3 Integration of Geometry and Medium for Stability ---- 8

2.3 Review of Previous Computational Studies ---- 9

2.4 Identification of the Specific Research Gap ---- 9

2.5 Research Objectives ---- 11

Chapter 3: Numerical Methodology ---- 12

3.1 Mathematical Framework ---- 12

3.2 Turbulence Modelling: The k−ϵ Approach ---- 14

3.3 Multiphase Flow: Volume of Fluid (VOF) Method ---- 16

3.4 Computational Implementation ---- 18

3.5 Numerical Domain and Boundary Conditions ---- 19

3.5.1 Geometric Simplification and Symmetry ---- 19

3.5.2 Inlet Velocity Derivation ---- 21

3.5.3 Thermophysical Properties at 1500°C ---- 22

3.5.4 Boundary Condition Summary ---- 23

3.6 Simulation Matrix and Parameters ---- 24

3.7 Grid Convergence Test ---- 26

3.7.1 Discretization and Mesh Statistics ---- 26
3.7.2 Grid Convergence Index (GCI) Methodology ---- 27
3.8 Metric Extraction and Data Processing ---- 28
3.8.1 Surface Topography Metrics (The Hump Metrics) ---- 28
3.8.2 Boundary Layer Interaction and Erosion Risk ---- 29
3.8.3 Data Extraction Methodology and Reference Fill Levels ---- 30
3.9 Models Utilized in the simulation ---- 32
Chapter 4: Results and Discussions ---- 34
4.1 Grid Convergence Calculations ---- 34
4.1.1 Global Flow Stability: Dead Zone (%) ---- 34
4.1.2 Theoretical Filling Height (mm) ---- 35
4.1.3 Synthesis and Discussion ---- 35
4.2 Dimensionless Flow Analysis ---- 35
4.2.1 Reynolds Number (Re) ---- 36
4.2.2 Weber Number (W_e) ---- 36
4.2.3 Froude Number (F_r) ---- 36
4.3 Characterization of the Baseline Model (90° Runner, 2.47 m/s) ---- 39
4.3.1 Flow Field Topology and Velocity Vector Dynamics ---- 39
4.3.2 Free-Surface Topography and Multiphase Interface Evolution ---- 40
4.3.3 Boundary Layer Friction and Refractory Protection Mechanics ---- 41
4.3.4 Volumetric Dead Zone Tracking and Thermal Consequences ---- 42
4.4 Comparative Study: Influence of Runner Angle ---- 43
4.4.1 Asymmetric Momentum Transport and Symmetry Breaking ---- 43
4.4.2 Wall Shear Stress Distribution and Relative Refractory Wear Risks ---- 46
4.4.3 Circulation Optimization (The 45° Case) ---- 49
4.5 Comparative Study: Influence of Inlet Velocity (90° Runner) ---- 51
4.5.1 Linear Throughput vs. Cubic Kinetic Energy Flux Scaling ---- 53
4.5.2 Boundary Layer past 3.0 m/s ---- 57
Chapter 5: Concluding discussions ---- 59
5.1 Hydrodynamic Behaviour and Operational Trade-Offs ---- 59
5.2 Practical Design Guidelines for Bottom-Pouring Systems ---- 61
Chapter 6. Conclusions ---- 63

Chapter 7: Sustainability and Future Work ---- 64
7.1 Sustainability and Environmental Impact ---- 64
7.2 Future Work ---- 65
Chapter 8: Utilisation of AI Tools ---- 66
References ---- 67
Appendix A: Models and Raw Transient Datasets ---- 72
A.1 Table Template and Common Vector Metrics ---- 74
A.2 Modified Angle: 85° Runner Configuration ---- 75
A.3 Modified Angle: 80° Runner Configuration ---- 75
A.4 Modified Angle: 75° Runner Configuration ---- 76
A.5 Modified Angle: 60° Runner Configuration ---- 76
A.6 Modified Angle: 55° Runner Configuration ---- 77
A.7 Modified Angle: 50° Runner Configuration ---- 77
A.8 Modified Angle: 45° Runner Configuration ---- 78
Appendix B: Raw Transient Datasets – Velocity Sensitivity Suite ---- 78
B.1 Transient Filling Metrics at a Reduced Velocity of 1.5 m/s ---- 78
B.2 Transient Filling Metrics at a Reduced Velocity of 2 m/s ---- 79
B.3 Transient Filling Metrics at a baseline Velocity of 2.47 m/s ---- 79
B.4 Transient Filling Metrics at increased Velocity of 3 m/s ---- 80
B.5 Transient Filling Metrics at increased Velocity of 3.5 m/s ---- 80
B.6 Transient Filling Metrics at increased Velocity of 4 m/s ---- 81
Appendix C: Computational Post-Processing and Metric Extraction Methodology ---- 81
C.1 Domain Isolation Framework ---- 81
C.2 Mathematical Isolation of Performance Metrics ---- 82
C.3 Automated Python Extraction Script Example ---- 83
Appendix D: Graphical Compendium of Transient Hydrodynamic Simulations ---- 86
D.1 Metrics vs Volume graphs for different angled runners ---- 86
D2. Metrics vs volume for different Inlet Velocities ---- 90

Chapter 1: Introduction

Ingot casting remains a primary manufacturing route for producing heavy steel components used in demanding applications, such as turbine shafts, mill rolls, and pressure vessels. While continuous casting is standard for smaller, high-volume products, ingot casting is still necessary for very large cross-sections that require subsequent forging or rolling. In this process, molten steel is poured into a refractory lined mould where it cools and solidifies. During filling and solidification, fluid flow, heat transfer, phase transformation, and volumetric shrinkage occur simultaneously, all of which directly determine the internal soundness and quality of the final ingot.

Controlling fluid flow during initial mould filling is critical because excessive turbulence can easily entrain air into the liquid metal. This leads to the formation of oxide films and non-metallic inclusions that become trapped in the steel, significantly degrading mechanical properties like fatigue strength and fracture toughness. Poor filling can also create surface defects and uneven temperature distributions that disturb the subsequent solidification front. Beyond filling-related defects, ingots are prone to macro-segregation the non-uniform distribution of alloying elements driven by solute rejection and fluid motion in the mushy zone as well as shrinkage porosity and pipe formation. These issues typically require feeders, hot tops, and optimized mould geometries to ensure proper liquid feeding as the steel contracts.

To investigate and minimize these defect mechanisms, Computational Fluid Dynamics (CFD) is widely used in casting research. CFD allows for detailed examination of mould filling by resolving velocity fields, turbulence levels, and free-surface motion, helping engineers evaluate gating system components such as pouring basins, runners, and ingates to achieve smoother filling. For capturing the multiphase interaction between molten steel and air, the Volume of Fluid (VOF) method is standard practice. It provides an effective way to track the moving free surface and identify localized problems like jet splashing, wave instability, and air entrainment, making it a practical tool for evaluating how gating design influences overall ingot quality.

1.1 The Global Scale of Ingot Casting

Although continuous casting is now the standard route across the commercial steel industry, ingot casting remains essential for producing high-alloy specialty steels and heavy forged parts that require high internal soundness and structural integrity [1, 2]. It is particularly critical for large, demanding components such as power-generation turbine shafts, pressure vessel shells, and industrial work rolls that exceed continuous casting size limits. To highlight the ongoing industrial relevance of the process, Table 1 outlines ingot casting production volumes across global, regional, and national levels for 2024 – 2025.

Table 1: Volumes for steel manufactured via ingot casting

Region	Total Crude Steel Production (2024)	Ingot Casting Share	Estimated Ingot Casting Tonnage
Sweden	~4.02 million tonnes [3, 4]	~10.8% [3]	~434,000 tonnes
Europe (EU27)	~129.5 million tonnes [2]	~3.4% [2]	~4.4 million tonnes
World Total	~1.88 billion tonnes [1, 5]	~2.6% [1]	~48.9 million tonnes

Globally, crude steel production reached approximately 1.88 billion tonnes in 2024 [1, 5]. While continuous casting makes up about 97.4% of this total, ingot casting still accounts for roughly 2.6% amounting to nearly 49 million tonnes annually, mainly for heavy machinery, aerospace, and energy applications [1, 5]. Within the European Union (EU27), total crude steel output was around 129.5 million tonnes in 2024, with ingot casting representing a 3.4% share [2]. This is slightly higher than the worldwide average, reflecting Europe's focus on high-value engineering grades and large forged components [2]. Sweden is a particularly notable case due to its domestic industry's emphasis on advanced steel grades: out of 4.02 million tonnes of annual steel production, about 10.8% (roughly 434,000 tonnes) is manufactured through the ingot route [3, 4]. This higher proportion is primarily driven by Swedish production of tool steels, high-alloy stainless steels, and specialty bars, where bottom-poured ingot casting is preferred to ensure the internal cleanliness, segregation control, and structural uniformity required for critical mechanical parts [3].

The Figure 1 Below highlights how Sweden stands out as a heavy user of this specific manufacturing process relative to its total output.

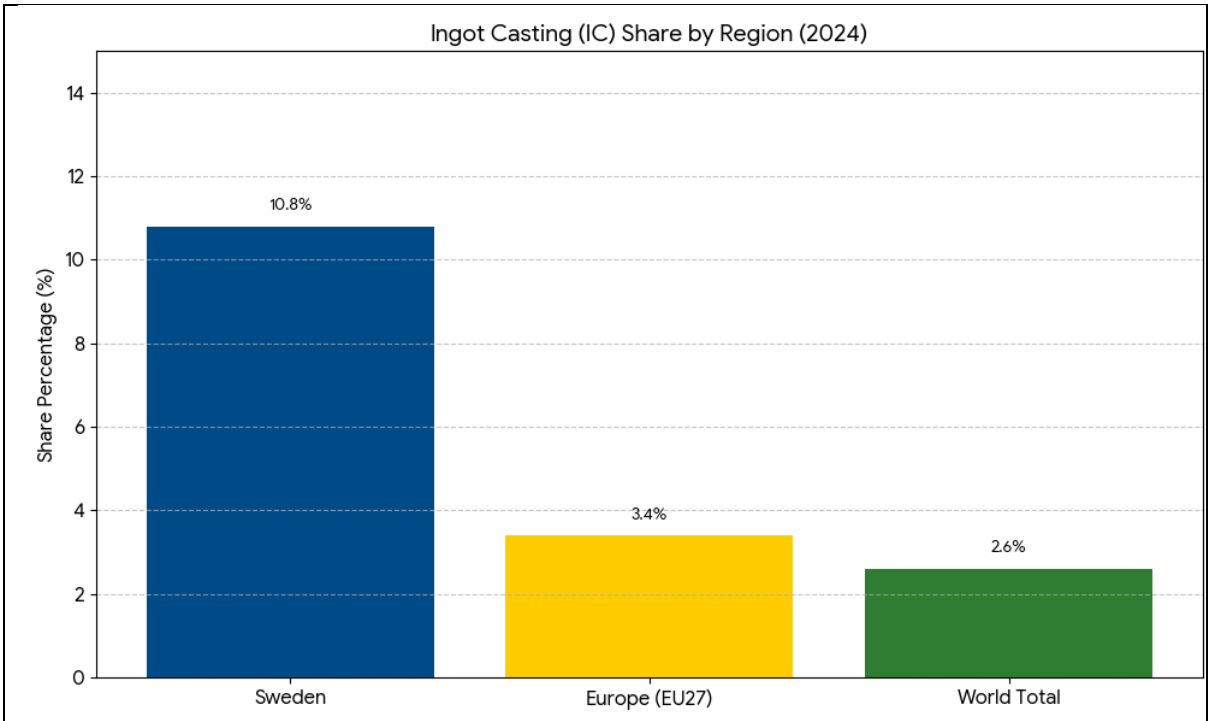

Figure 1: Regional Comparison of Ingot Casting (IC) Market Share (2024)

1.2 Problem Definition

In industrial uphill (bottom-poured) ingot casting, particularly when large-scale geometries like a 3000 mm trumpet and an octagonal mould are used, there are several ongoing challenges. These issues can significantly affect the metallurgical quality as well as the overall yield of the final product [6, 7, 10].

The main industrial challenges can be grouped into three categories: the flow behaviour in the delivery system, disturbances during the initial filling stage, and flow patterns that are specific to the mould geometry.

1.2.1 Delivery System and Hydraulic Issues

The high potential energy in a three-meter trumpet creates significant hydraulic challenges before the metal even reaches the mould. Within the delivery system, the high velocity of the incoming steel stream frequently generates localized low-pressure regions near the top of the trumpet, inducing an aspiration effect that draws ambient air directly into the molten metal. This transient gas entrainment serves as a primary driver of liquid metal re-oxidation and promotes the formation of subsurface porosity defects [6, 10]. Simultaneously, the rapid transit of liquid steel through the well and refractory runner channels generates intense mechanical impact and hydrodynamic shear against the lining boundaries. This refractory erosion is particularly severe at high-momentum geometric transitions, notably at the entrance of the horizontal runner and adjacent to the mould ingates [12]. As the refractory matrix degrades under these aggressive flow conditions, detached ceramic particles wash directly into the moving melt, acting as a prominent source of macroscopic exogenous non-metallic inclusions that compromise the final ingot cleanliness.

1.2.2 Initial Filling Disturbances

The initial 5–10% of the mould-filling sequence represents the most critical and hydrodynamically volatile phase in industrial ingot casting [9, 10]. During this early interval, the incoming surge of molten steel generates a pronounced central fountain-like upwelling, commonly designated as the geyser or core hump effect (M1). When inertial forces overcome surface tension typically occurring once the localized Weber number surpasses a critical threshold ($We > 12.3$) the cohesive interface ruptures into violent splashing, driving atmospheric air and surface additions deep into the bulk melt [6, 9]. This severe interfacial turbulence exacerbates the risk of mould flux entrapment during the opening seconds of teeming, as the high-momentum metal jet readily washes away, fragments, and mechanically entrains the solid powder bed before a stable, continuous liquid slag buffer has sufficient time to form across the rising melt surface [6, 10].

1.2.3 Issues Specific to Octagonal Moulds

Using an octagonal mould introduces distinct hydrodynamic and thermal complexities compared to conventional cylindrical or square mould geometries [6]. From a fluid dynamics standpoint, the geometry forms eight peripheral corner regions where fluid velocity drops below 0.05 m/s, establishing stagnant dead zones that inhibit active convective mixing [12, 13]. Within these quiescent pockets, accelerated heat loss promotes premature dendritic freezing and cold-shut formation, while also trapping floating non-metallic inclusions that degrade the final ingot surface quality [12, 13]. From a thermal perspective, the mould corners act as localized heat sinks that solidify at a considerably faster rate than the adjacent flat faces [3]. This uneven cooling induces severe thermal gradients and differential contraction stresses across the shell, significantly elevating the risk of longitudinal cracking during solidification [3]. Furthermore, octagonal profiles complicate yield and taper management, requiring substantial hot-top feeding volumes to compensate for volumetric shrinkage while demanding

strict control over the mould taper typically around 3–5% to prevent mechanical sticking, hot tearing, or wall cracking as the contracting steel pulls away from the eight-sided perimeter [15]

1.3 Technical Challenges in Initial Filling

The uphill (bottom-up) teeming process is preferred for high-quality steel production because it provides a calmer filling compared to top-pouring [8, 18, 21]. However, it remains susceptible to several critical fluid-dynamic and metallurgical issues, many of which are rooted in the initial filling stage.

1.3.1 Issues with Current Uphill Ingot Casting

Although uphill teeming avoids the splashing of top-pouring, it introduces several fluid flow and cleanliness challenges. High surface turbulence can entrain mould flux into the liquid steel, forming non-metallic inclusions and surface defects [6, 10, 17], while low-pressure vortices near the trumpet top or elbow can pull in ambient air, causing subsurface porosity and re-oxidation [6, 10]. Furthermore, molten steel accelerating down a 3000 mm trumpet head can exceed 7 m/s, producing high wall shear stresses that erode the refractory lining and wash ceramic particles into the mould cavity [12, 18]. In the first few seconds before a protective liquid slag layer forms, the exposed steel surface also reacts directly with the air [6, 10]. Finally, polygonal moulds particularly octagonal or square geometries develop stagnant corner regions where velocities drop below 0.05 m/s, accelerating localized heat loss and worsening macro-segregation during solidification [12, 13].

1.3.2 Importance of the Initial Filling Stage

The first few seconds of mould filling largely determine final ingot quality. Molten steel enters the cavity with peak kinetic energy, forming a strong central upwelling or core hump. When inertial forces overcome surface tension at high localized Weber numbers, this fountain collapses into turbulent splashing that pulls atmospheric air and mould powder into the melt [6, 9]. The resulting velocity fluctuations can also erode or tear the thin solidifying shell along the lower mould perimeter, leading to surface cracking and hot tears [16]. At the same time, air trapped during the priming of the runner system can detach and enter the mould cavity as bubble streams [22]. In addition, molten steel at roughly 1500°C contacting the cold mould walls causes severe thermal shock, making a calm, stable meniscus rise essential to protect the mould lining and support uniform shell growth [12, 18]. To reduce these issues, recent research has focused on alternative gating configurations, such as angled runners or side-teeming, which lower the initial hump height, dissipate vertical kinetic energy, and establish a more stable filling pattern [8, 18].

Chapter 2: Literature Review

This chapter reviews previous research on steel ingot casting and the CFD methods used to simulate transient mould filling. It outlines the fluid dynamic mechanisms that govern flow stability, surface turbulence, and defect formation during teeming. In addition, it compares common industrial casting setups, focusing on how gating geometry and feeding design affect momentum dissipation, meniscus stability, and final ingot cleanliness.

2.1 Types of Ingot Casting and Industrial Utilization

The primary methods are used to fill ingot moulds, each presenting different trade-offs regarding flow stability, equipment complexity, and steel cleanliness: uphill teeming, top pouring, side teeming, and vacuum ingot casting (VIC). Among these, uphill (bottom) teeming is the dominant industrial method for high-quality steel production, accounting for over 90% of quality-critical ingot manufacturing in Sweden and the rest of Europe [6, 7]. In this arrangement, molten steel is poured into a central trumpet and distributed through horizontal refractory runners to enter the mould cavity from the bottom [6, 10]. Compared to pouring directly from above, introducing the melt from below provides a significantly calmer rising meniscus and reduces splashing, making it the standard method for casting the high-alloy and tool steels modelled in this work.

By contrast, traditional top pouring where liquid steel is teemed directly from the ladle into the open top of the mould now represents only about 5–10% of global ingot production [6, 10]. It is largely restricted to commercial carbon grades or smaller ingots where surface finish and internal cleanliness specifications are less demanding. Although top pouring requires lower capital investment and simpler tooling, the falling open stream generates high interfacial turbulence, leading to severe air entrainment, splashing, and oxide inclusion formation [10].

The remaining two routes serve niche or specialized operational needs. Side teeming introduces molten steel through an inclined channel in the mould wall rather than through the bottom floor. While it currently accounts for less than 1% of production and remains mostly experimental, it has attracted research interest because the angled entry can generate rotational flow structures that help suppress central surface humps during filling [8]. Lastly, Vacuum Ingot Casting (VIC) is reserved for extra-large forging ingots weighing up to several hundred tonnes, primarily for critical components in power generation and aerospace [5]. Although VIC represents only 2–5% of global volume, carrying out the teeming process inside an evacuated chamber is necessary to degas dissolved hydrogen from the melt, preventing hydrogen-induced flaking and internal cracking across very thick sections [12].

Table 2: Comparison of Global Steel Ingot Casting Methods

Method	Global Share	Key Advantage	Typical Application
Uphill Teeming [6,7,10]	85-93%	Calm rising surface, low splashing	Alloy & Tool steels (Quality-sensitive)
Top Pouring [6,10]	5-10%	Low capital cost, simple setup	Commercial/Carbon grades
Side Teeming [8]	<1%	Rotational flow control	Niche / Experimental
Vacuum [5,12]	2-5%	Hydrogen removal, structural integrity	XL Forging (Aerospace/ Power)

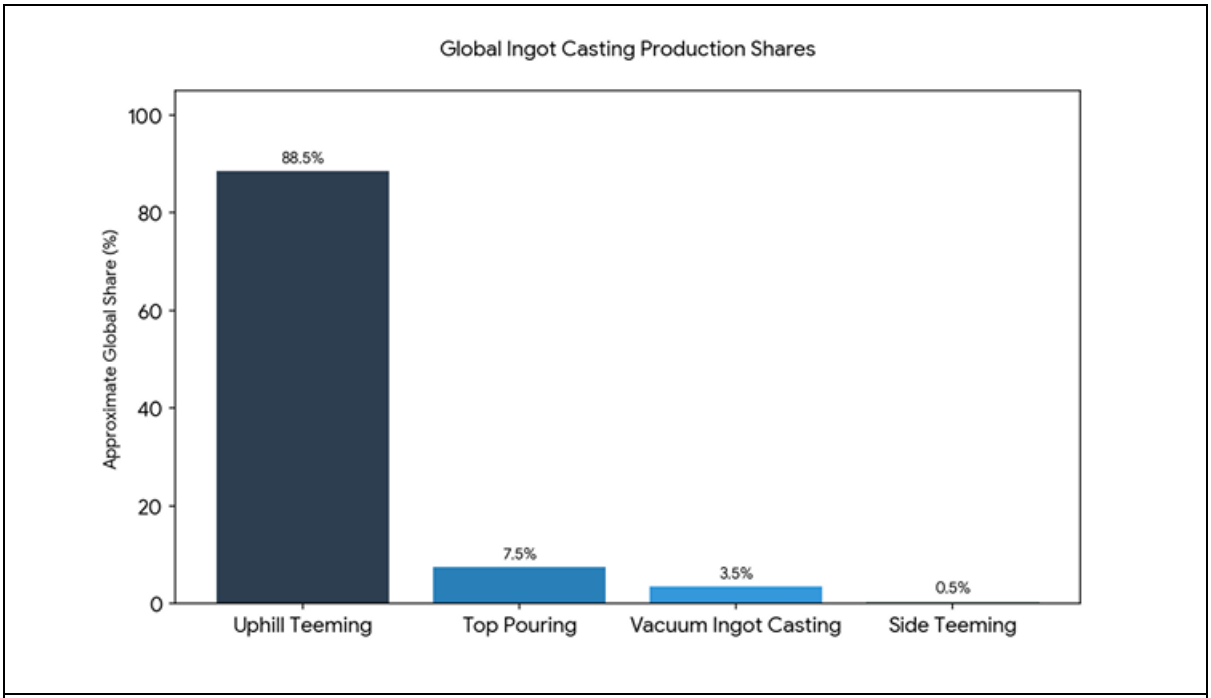

Figure 2: Global Ingot casting production shares

The data reflects a clear industry preference for Uphill Teeming, which accounts for approximately 85% to 93% of the global market due to its ability to produce high-quality, defect-free alloy and tool steels [6, 7, 10]. While Top Pouring offers a lower-cost alternative for standard commercial grades [6, 10], specialized processes like Vacuum Ingot Casting (VIC) remain essential for high-integrity applications in the aerospace and power sectors, where hydrogen removal and structural reliability are critical [5, 12].

2.2 Mechanics of the Trumpet and Runner System

The configuration of the gating system, particularly the geometry of the trumpet and runner, along with the properties of the surface medium (mould flux), act as the main passive flow control tools in uphill ingot casting. Together, these elements govern how the kinetic energy of the molten steel is dissipated as it flows through the system, how stable the free surface remains during filling, and ultimately the level of cleanliness achieved in the final steel product [6, 10, 12].

2.2.1 Role of Trumpet-Runner Geometry in Flow Control

The gating system acts as a hydraulic regulator, converting the potential energy of the molten steel into controlled upward flow inside the mould cavity [12, 23]. In this setup, the trumpet height and diameter determine the ferrostatic head and total flow rate. However, if the liquid level in the trumpet drops or local velocities become too high, low-pressure vortices can form and pull in ambient air, leading to subsurface porosity and re-oxidation inclusions [6, 10]. At the base of the trumpet, the well functions as an energy dissipator, absorbing vertical momentum to feed the runner with a calmer, more stable stream [12]. While standard horizontal runners often produce high-velocity jets that form a pronounced central geyser (M1 core hump), angling the runner (such as at 30°) significantly lowers this hump and promotes a smoother filling rise [18]. In addition, the entry angle into the mould cavity directly controls the formation of toroidal recirculation loops, where an optimized angle helps suppress surface turbulence and reduces mould flux entrapment compared to a standard perpendicular ingate [8].

2.2.2 Role of the Mould Flux in Flow Control

Mould powder melts into a liquid slag layer on top of the rising steel and serves several key metallurgical functions during filling [6, 10, 17]. It acts as a physical barrier that reduces radiant heat loss and shields the molten steel from atmospheric air, helping prevent re-oxidation and oxide inclusion formation [6, 10]. The slag layer also absorbs floating non-metallic inclusions, such as alumina particles and eroded refractory sand, as they reach the surface [10]. In addition, liquid slag infiltrates the gap between the mould wall and the steel shell to provide lubrication, reducing friction and lowering the risk of shell sticking or surface cracking as the metal contracts [12]. However, the effectiveness of this layer depends heavily on fluid flow inside the mould. If surface turbulence or strong upwelling causes the local Weber number (We) to exceed critical limits, hydrodynamic shear forces can break up the slag layer and pull droplets down into the melt, leading to large non-metallic inclusions in the cast ingot [6, 17].

2.2.3 Integration of Geometry and Medium for Stability

Modern casting design focuses on optimising the gating ratio, which refers to the ratio of cross-sectional areas of the trumpet, runner, and ingates, to ensure that the system stays properly primed during filling. A pressurised flow system helps prevent air from being drawn into the melt through refractory joints. At the same time, carefully designed runner angles help maintain

the surface medium as a continuous protective layer, rather than allowing it to break up and become a source of inclusions [21, 23].

2.3 Review of Previous Computational Studies

To control flow disturbances during the initial stage of uphill teeming primarily to lower the central geyser hump (M1), minimize droplet splashing (M2), and prevent the entrapment of mould flux and air. Previous work has combined numerical modelling, physical experiments, and specialized gating hardware [6, 8, 9]. Numerically, mould filling analysis has evolved from simple single-phase approximations to transient multiphase simulations. The Volume of Fluid (VOF) method is widely used to track the moving melt surface and measure hump elevations. However, because interfacial behaviour is sensitive to turbulence closure, second-moment approaches like the Reynolds Stress Model (RSM) are often preferred over isotropic k– ε models for capturing the anisotropic, swirling flows common during the initial surge [12, 38]. Meshless methods such as Smoothed Particle Hydrodynamics (SPH) have also been tested to better resolve droplet breakup and rogue splashing, while commercial packages like MAGMASOFT and ProCAST are used to iteratively evaluate designs that reduce air entrainment and wall shear stress [20, 24, 25].

These simulations are typically supported by 1:1 or 1:3 scale water models, using dye tracers and Ultrasonic Velocity Profiling (UVP) to measure internal velocity fields and validate predicted surface profiles [9, 21]. In plant trials, positioning argon shrouds directly over the trumpet opening rather than at the ladle nozzle has proven notably more effective at preventing steel re-oxidation during the opening surge [14]. On the hardware side, passive flow-control devices are frequently added to the runner system to dissipate excessive kinetic energy. Swirl inserts, such as TurboSwirl, impart tangential velocity to convert vertical momentum into a rotational, more uniform upward flow [15, 21]. Ceramic foam filters (such as zirconia-based STELEX inserts) are also placed in the runners to both filter out inclusions and dampen turbulence before the steel enters the mould [22]. Finally, gating networks often feature refractory spin traps dead-end runner extensions positioned past the ingate to catch the initial turbulent wave and trap loose ceramic debris before it reaches the mould cavity [23].

2.4 Identification of the Specific Research Gap

Despite the considerable progress made in applying the Volume of Fluid (VOF) method to simulate mould filling in steel ingot casting, several critical gaps persist in the existing literature. Addressing these limitations is essential to enhance the predictive fidelity of numerical models and strengthen their practical relevance to industrial process optimisation. A primary shortcoming is that a substantial proportion of prior investigations rely on simplified geometries, laboratory-scale water models, or truncated computational domains. In many cases, critical delivery components such as the vertical downsprue trumpet, the horizontal runner network, and the specific mould geometry are omitted to economise computational cost. While these reduced models offer general fluid-dynamic insights, they fail to replicate the

coupled hydrodynamics of full-scale operations. Notably, there remains a distinct scarcity of grid-converged CFD studies conducted on complete, full-scale octagonal ingot moulds, where the interplay between large liquid steel volumes and eight-corner geometric constraints significantly alters turbulence dissipation, free-surface stability, and defect formation. Furthermore, transient suction and gas entrainment occurring at the trumpet inlet remain poorly captured. As molten steel accelerates down the sprue, localized low-pressure zones readily aspirate ambient air. Most numerical studies circumvent this dynamic by imposing idealized, single-phase liquid-only inlet boundary conditions, thereby underestimating air entrainment and neglecting the formation of oxide films generated during the earliest moments of teeming.

A third notable gap concerns the initial interaction between the advancing metal front and the mould powder bed. Prior to the establishment of a continuous, fully melted liquid slag layer, the opening surge of liquid steel impacts the solid powder directly, causing mechanical displacement, particle fragmentation, and premature entrapment into the melt bulk. This transient opening stage has received minimal systematic attention in both experimental and numerical casting literature, leaving the precise mechanisms governing early inclusion generation largely unquantified. Similarly, while side-teeming configurations have been proposed as an alternative method to suppress vertical jet momentum and generate a calmer meniscus rise, introducing liquid steel horizontally induces direct, high-momentum jet impingement against opposing mould walls and refractory linings. The resulting hydrodynamic trade-off between dampening free-surface turbulence and elevating refractory erosion rates has not been systematically characterized in terms of local wall shear stress distributions and boundary-layer turbulence. Collectively, these research gaps underscore the need for comprehensive CFD investigations that incorporate complete, realistic industrial assemblies and transient multiphase boundary conditions. Within this context, the present study directly addresses the challenges of full-scale industrial geometry and transient gas entrainment by conducting a full-domain parametric investigation across variable runner inclinations and inlet velocities. In contrast, the multiphase interaction with solid mould powder and the evaluation of side-teeming configurations remain outside the primary scope of this work and are identified as priority avenues for future research.

2.5 Research Objectives

The primary goal of this research is to use transient CFD simulations to evaluate fluid flow stability during the initial filling stage of a large-scale uphill teeming process for an octagonal ingot. To achieve this, the study first quantifies free-surface stability during the initial 150 mm of mould rise by tracking core hump height (M1), droplet splashing (M2), and volumetric meniscus distortion (M4). Second, it evaluates deep air entrainment across inlet velocities ranging from 1.5 to 4.0 m/s to identify critical velocity limits linked to cubic kinetic energy scaling ($E_k \propto U^3$). Third, it examines jet trajectory and maps localized wall shear stress against refractory yield thresholds (400–1200 Pa) to identify areas prone to brick erosion and exogenous inclusion pickup. Finally, it calculates the volume fraction of stagnant dead zones ($v < 0.05$ m/s) within the octagonal cavity to assess whether the incoming momentum creates sufficient corner circulation to prevent localized chilling and cold-shut defects.

Chapter 3: Numerical Methodology

This chapter outlines the mathematical framework, governing transport equations, and numerical formulations employed to simulate the transient mould-filling dynamics of bottom-poured steel ingot casting. Formulated within a Eulerian computational fluid dynamics (CFD) framework, the methodology is designed to resolve the unsteady, two-phase interaction between liquid steel and the surrounding gaseous atmosphere across the complete gating and mould domain. Particular emphasis is placed on the governing Navier-Stokes equations, the Volume of Fluid (VOF) interface-capturing technique, and the turbulence closure approximations that dictate interfacial stability, momentum dissipation, and hydrodynamic defect generation throughout the critical opening stages of teeming.

3.1 Mathematical Framework

The numerical model is based on the fundamental conservation equations for mass and momentum, supplemented by appropriate turbulence and multiphase flow models. Together, these equations provide a comprehensive description of the transient flow field and enable accurate simulation of the interaction between molten steel and the surrounding air during the filling process.

The flow of liquid steel during the ingot filling process is governed by the conservation of linear momentum, expressed through the Navier–Stokes equations. Within the casting process at approximately 1500^{o} C, the molten steel is modelled as a continuum Newtonian fluid with high density ($\rho \approx 7000\ kg/m^3$), where inertial effects dominate viscous forces due to the large incoming mass flow rate of 55 kg/s. The resulting flow field is strongly influenced by the interaction between the high-momentum inlet jet and the complex confinement geometry of the well system [28].

To account for turbulence effects, the instantaneous velocity field is decomposed into mean and fluctuating components using Reynolds decomposition:

$$u = u + u' \tag{3.1}$$

Substituting into the Navier–Stokes equations and applying time averaging yields the Reynolds-Averaged Navier–Stokes (RANS) momentum equations:

$$\rho\,(\partial u/\partial t + u\cdot\nabla u) = -\nabla p + \nabla\cdot[\mu(\nabla u + \nabla u^{T})] - \nabla\cdot(\rho u'u') + \rho g + S_M \tag{3.2}$$

The additional term $-\rho u'u'$ represents the Reynolds stress tensor, which arises from turbulent momentum transport and requires closure through a turbulence model, as discussed in Section 3.2.

Each term in the Reynolds-Averaged Navier-Stokes momentum equation represents a distinct physical force governing the transient dynamics of the 55 kg/s liquid steel stream. The transient acceleration term, **$(\partial/\partial\ t\ \rho\ u)$** accounts for the local rate of momentum accumulation as the initially empty downsprue, well, and runner assembly undergo dynamic priming. Concurrently, the convective acceleration term, **$(\nabla \cdot \rho\ u\ u)$** characterizes the spatial transport of momentum

by the mean bulk fluid motion [26]. The directional orientation of this advective transport is strongly coupled to the delivery architecture: in a conventional perpendicular 90° runner geometry, this term is overwhelmingly dominated by vertical axial momentum vectors that drive the central fountain upwelling, whereas inclined runner configurations effectively redistribute a significant fraction of this kinetic energy into horizontal sweeping vectors along the mould floor [8, 18, 30]. Balancing these inertial forces, the filtered pressure gradient, **$(-\nabla \bar{p})$** constitutes the primary mechanical driving force, arising from the cumulative ferrostatic head within the vertical downsprue coupled with the high dynamic impact pressure developed at the refractory well floor. Finally, the turbulent momentum transport is captured by the Reynolds stress divergence, **$(-\nabla \cdot \rho \mathbf{u}\mathbf{u})$** which models the macroscopic diffusion of momentum induced by fluctuating turbulent eddies and is closed in the present computational framework via the two-equation k- ε model detailed in Section 3.2.

The primary role of advanced well geometries is the modification of the convective momentum transport structure within the flow domain. By introducing controlled geometric conditions and guided flow paths, the inlet jet undergoes redistribution of its axial momentum into secondary and tangential components, thereby altering the local momentum flux tensor and promoting enhanced internal mixing.

This can be interpreted in terms of angular momentum generation:

$$L=\int \rho(r\times u)\, dV \tag{3.3}$$

Where the generation of swirl modifies the spatial distribution of kinetic energy and promotes dissipation through increased shear layer development. From a physical standpoint, this mechanism reduces the intensity of coherent downward jet structures and redistributes energy across a larger volume of the well, thereby influencing the velocity field exiting into the mould region.

The momentum equation is inherently coupled with the continuity constraint:

$$\nabla \cdot u=0 \tag{3.4}$$

Because incompressible flows lack an explicit pressure equation, pressure–velocity coupling is handled using OpenFOAM's PIMPLE algorithm. By combining the transient accuracy of PISO with the under-relaxation of SIMPLE, PIMPLE maintains numerical stability across larger time steps while iteratively satisfying both momentum and continuity essential for capturing the rapid changes in free-surface shape and internal recirculation during filling.

Surface tension at the steel–air interface is incorporated into the momentum balance as a source term (S_M) using the Continuum Surface Force (CSF) formulation [43, 48]. This approach converts localized capillary forces into an equivalent volumetric body force based on interface

curvature across the transition cells (Alpha), allowing the solver to model meniscus deformation, surface breakup, and droplet splashing during the initial stage of teeming.

3.2 Turbulence Modelling: The k−ϵ Approach

For the high-velocity teeming conditions investigated ($Re > 10^5$), the flow entering the mould rapidly enters a fully turbulent regime. The Reynolds-Averaged Navier–Stokes (RANS) equations are closed using the Standard two-equation k– ϵ model with standard empirical constants ($C_\mu = 0.09$, $C_{1\varepsilon} = 1.44$, $C_{2\varepsilon} = 1.92$, $\sigma_k = 1.00$, $\sigma_\varepsilon = 1.30$) [36, 38]. This formulation was selected because it provides the numerical robustness, bounded stability, and computational economy required to simulate high-Reynolds-number, transient multiphase flows involving violent free-surface deformations. While higher-order closures such as the Reynolds Stress Model (RSM) or Large Eddy Simulation (LES) capture anisotropic eddy structures and rotational swirling components with greater physical fidelity, their severe computational overhead and susceptibility to numerical divergence across moving VOF interfaces make them impractical for multi-case parametric evaluations [12, 38].

To model near-wall momentum exchange along the refractory walls and mould cavity, standard semi-empirical wall functions are utilized rather than resolving the viscous sublayer directly. Resolving the viscous sublayer ($y^+ \approx 1$) would require extreme near-wall cell clustering, substantially increasing cell counts and rendering systematic spatial mesh sensitivity (GCI) analyses computationally prohibitive. Accordingly, near-wall cell heights are generated such that cell centroids fall within the logarithmic layer ($30 < y+ < 300$) across the examined mesh resolutions, ensuring reliable boundary shear stress predictions without excessive numerical cost [36, 40].

In the OpenFOAM framework, turbulence transport equations are integrated using the transient PIMPLE algorithm (a merged PISO–SIMPLE formulation) to resolve the stiff pressure–velocity coupling during rapid mould filling. Convective terms in the momentum, k and ϵ transport equations are discretised using a bounded second-order upwind scheme to suppress numerical diffusion while preventing non-physical oscillations, while the pressure Poisson equation is discretised using a second-order conservative scheme. To ensure clean solver startup and avoid initial numerical divergence, turbulent kinetic energy (k) and dissipation rate (ϵ) are prescribed at the inlet using a standard turbulence intensity of I = 5% and a characteristic length scale based on the hydraulic runner diameter.

Under this framework, the Reynolds stresses are expressed as:

$$-\rho u_i' u_j' = \mu t(\partial U_i/\partial x_j + \partial U_j \partial x_i) - 2/3 \rho k \delta_{ij} \quad (3.5)$$

Where U_i represents the mean velocity components, k is the turbulent kinetic energy, and δ_{ij} is the Kronecker delta accounting for isotropic normal stress contribution.

The turbulent viscosity is modelled empirically as:

$$\mu_t=\rho C_\mu k^2/\epsilon \tag{3.6}$$

For Turbulent Kinetic Energy (k):

$$\partial (\rho k)/\partial t + \nabla \cdot (\rho u k) = \nabla \cdot [(\mu + \mu_t/(\sigma_k) \nabla k] + G_k + G_\beta - \rho \varepsilon - Y_M + S_k \tag{3.7}$$

For Rate of Dissipation (ε):

$$\partial (\rho \varepsilon)/\partial t + \nabla \cdot (\rho u \varepsilon) = \nabla \cdot [(\mu + \mu_t/ (\sigma_\varepsilon) \nabla \varepsilon] + C_{1\varepsilon} (\varepsilon/k) (G_k + C_{3\varepsilon} G_\beta) - C_{2\varepsilon} \rho (\varepsilon^2/k) + S_\varepsilon \tag{3.8}$$

In these expressions, G_k represents the production of turbulent kinetic energy resulting from mean velocity gradients. G_b is the generation of turbulence due to buoyancy (critical in 1500^o C) steel due to temperature-induced density gradients).The constants $C_{1\varepsilon}$, $C_{2\varepsilon}$, C_μ, σ_k, and σ_ε are empirical values originally derived from experimental studies on air and water flows. However, they are also commonly applied in simulations of liquid metal flows. The turbulence model is closed using these standard empirical constants, which have been validated for a wide range of shear flow conditions [36].

Table 3: Empirical Constants used in the k- ε Turbulence Model

Constant	Value	Description
$\mathbf{C_\mu}$	0.09	Eddy viscosity coefficient
$\mathbf{C_{1\varepsilon}}$	1.44	ε production constant
$\mathbf{C_{2\varepsilon}}$	1.92	ε destruction constant
$\boldsymbol{\sigma_k}$	1.00	Turbulent Prandtl number for k
$\boldsymbol{\sigma_\varepsilon}$	1.30	Turbulent Prandtl number for ε

The turbulent kinetic energy is computed as:

$$k=3/2(U_{avg}I)^2 \quad (3.12)$$

The dissipation rate is estimated using:

$$\epsilon=C\mu^{3/4}\, k^{3/2} / L \quad (3.13)$$

Where U_{avg} is the inlet mean velocity, L is the characteristic turbulent length scale (taken as the runner diameter), and C_μ is the empirical constant of the Standard k−ϵ model. These initial estimates provide physically consistent starting fields that reduce the risk of numerical instability during the early transient iterations. In particular, they prevent divergence associated with non-physical values of k and ϵ, which can otherwise lead to solver instability in high-velocity casting simulations.

3.3 Multiphase Flow: Volume of Fluid (VOF) Method

The transient two-phase flow between the incoming liquid steel (55 kg/s) and the ambient atmosphere is resolved using the Eulerian Volume of Fluid (VOF) method implemented in OpenFOAM's interFoam solver [43]. Global mass conservation is enforced via the incompressible continuity condition ($\nabla \cdot u = 0$), while the immiscible interface is tracked using the scalar phase fraction α (α = 1 for liquid steel, α = 0 for air, and $0 < \alpha < 1$ across the meniscus). Local fluid properties primarily density (ρ) and dynamic viscosity (μ) are evaluated across the interfacial cells using volume-fraction-weighted linear averages [43].

Interfacial surface tension is incorporated into the momentum balance as a volumetric body force using the Continuum Surface Force (CSF) formulation ($f_\sigma = \sigma \kappa \nabla \alpha$) [48], capturing free-surface curvature, droplet fragmentation, and jet disintegration. To maintain numerical stability in this high-inertia, turbulent regime, physical boundedness is strictly guaranteed via the Multidimensional Universal Limiter with Explicit Solution (MULES). This limiter eliminates unphysical phase-fraction overshoots and prevents floating-point divergence (SIGFPE), ensuring robust convergence throughout the initial filling sequence [50].

$$\nabla \cdot u = 0 \quad (3.14)$$

The distribution of the steel phase is governed by an advection equation:

$$\partial \alpha/\partial t + \nabla \cdot (\alpha u) + \nabla \cdot [\alpha (1 - \alpha) u_r] = 0 \quad (3.15)$$

The third term, $\nabla \cdot [\alpha (1 - \alpha) u_r]$, is an artificial compression term unique to OpenFOAM's VOF implementation. It prevents the numerical smearing of the interface a critical requirement for maintaining a sharp 15 mm flux layer in the 10 mm fine mesh study [43].

The physical properties, such as density (ρ) and dynamic viscosity (μ), are calculated as a weighted average based on the local value of α [43]:

$$\rho = \alpha \rho_{steel} + (1 - \alpha) \rho_{air} \quad (3.16)$$

$$\mu = \alpha \mu_{steel} + (1 - \alpha) \mu_{air} \quad (3.17)$$

Given the substantial density ratio between liquid steel and air, accurately resolving interfacial density gradients is critical for capturing free-surface splashing, droplet breakup, and pool stabilization [18, 43, 50]. Interfacial surface tension at 1500^o C is incorporated directly into the momentum balance as a volumetric source term, f_σ, using the Continuum Surface Force (CSF) formulation [48]:

The force is added as a source term f_σ to the momentum equation:

$$f_\sigma = \sigma \kappa \nabla \alpha \quad (3.18)$$

where σ is the surface tension coefficient of the steel and kappa is the interface curvature, defined as:

$$\kappa = -\nabla \cdot (\nabla \alpha / |\nabla \alpha|) \quad (3.19)$$

3.4 Computational Implementation

The transition from theoretical modelling to numerical results requires a highly structured computational strategy. This section details the implementation of the mathematical models specifically the k-ε turbulence framework and the associated transport equations within a digital environment. By establishing a rigorous numerical workflow, this study ensures that complex interactions such as fluid velocity, thermal gradients, and pressure fields are resolved with high fidelity. The following subsections outline the integrated software ecosystem, the construction of the numerical domain, and the specific simulation matrix used to validate the model's performance.

The simulation setup follows an integrated open-source workflow, where cfMesh is used as the main tool for spatial discretisation. This pipeline links parametric geometry creation in FreeCAD with the high-performance solver capabilities of OpenFOAM 12.4.

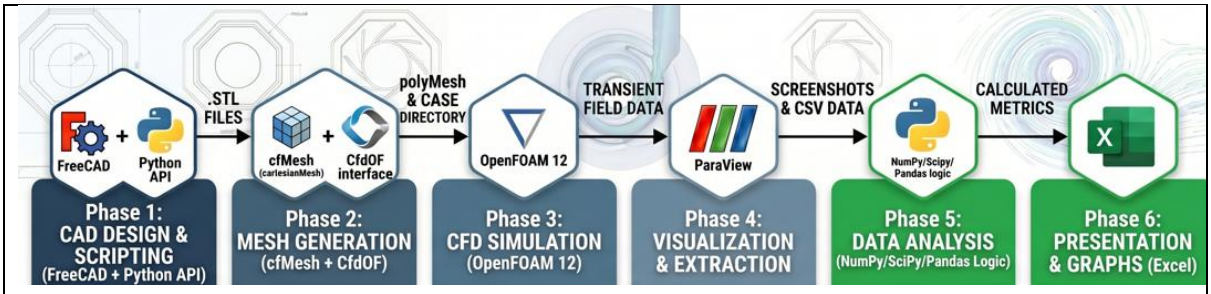

Figure 3: Software Workflow

The computational workflow begins with the three-dimensional geometric modelling of the delivery well and octagonal mould in FreeCAD, where individual boundary surfaces are exported independently to allow targeted local mesh refinement and explicit patch assignment. Volume discretisation is performed using cfMesh via the cartesianMesh utility within the CfdOF framework, generating a predominantly hex-dominant computational grid with template-based cell transitions. Compared to iterative octree-based trimming methods, cfMesh preserves high cell orthogonality along complex internal and helical boundaries, substantially suppressing numerical diffusion and preventing floating-point exceptions (SIGFPE) under the high-momentum 55 kg/s stream. Furthermore, the high regularity of the Cartesian cells in the core flow domain limits grid-induced artificial turbulence, ensuring consistent performance of the Standard k−ϵ model.

The generated mesh is imported into OpenFOAM, where the multiphase interFoam solver resolves the transient hydrodynamics using the PIMPLE pressure–velocity coupling scheme. Post-processing couples qualitative flow field visualisation in ParaView focusing on free-surface evolution and swirl structure development with automated Python routines for

quantitative evaluation. Python scripts extract transient velocity and pressure fields across the well exit to compute the Grid Convergence Index (GCI), bounding the spatial discretisation uncertainty and confirming that the predicted hydrodynamic mechanisms are physically driven rather than numerical artefacts of the mesh.

3.5 Numerical Domain and Boundary Conditions

This section describes the physical and numerical setup of the simulation, including the geometric modelling approach, the derivation of inlet conditions, and the thermophysical properties of the phases at the pouring temperature of 1500°C.

3.5.1 Geometric Simplification and Symmetry

The industrial casting setup, which is modelled after an operational production geometry from a steel company consists of a central pouring basin, or trumpet, which splits to supply molten metal into two identical mould cavities. To improve computational efficiency while maintaining sufficient numerical resolution, a symmetry plane approach was utilized. [53].

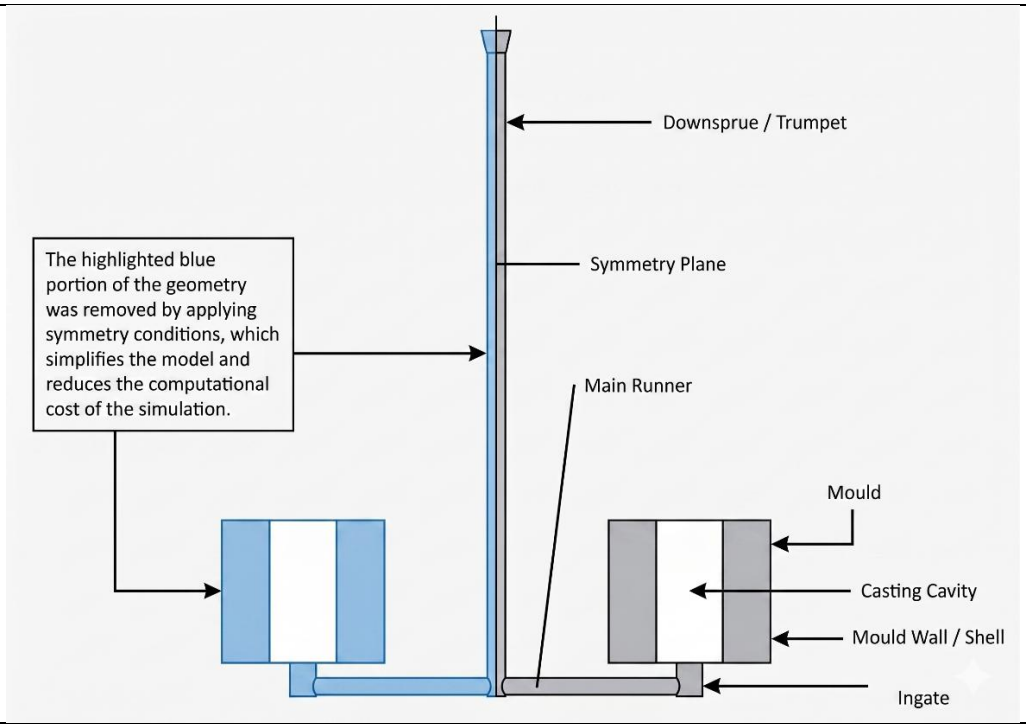

Figure 4: Schematic of the casting assembly and mould geometry

The domain was divided along the longitudinal central axis of the trumpet, effectively reducing the model to 50% of the full geometry. This simplification is considered valid because the flow is expected to be approximately mirror-symmetric under ideal operating conditions.

A symmetry boundary condition is applied on the cut plane, which enforces zero normal velocity and zero-gradient conditions for scalar variables. In effect, this boundary behaves like a reflective plane, allowing the flow behaviour of the full system to be represented using only half of the computational domain [54].

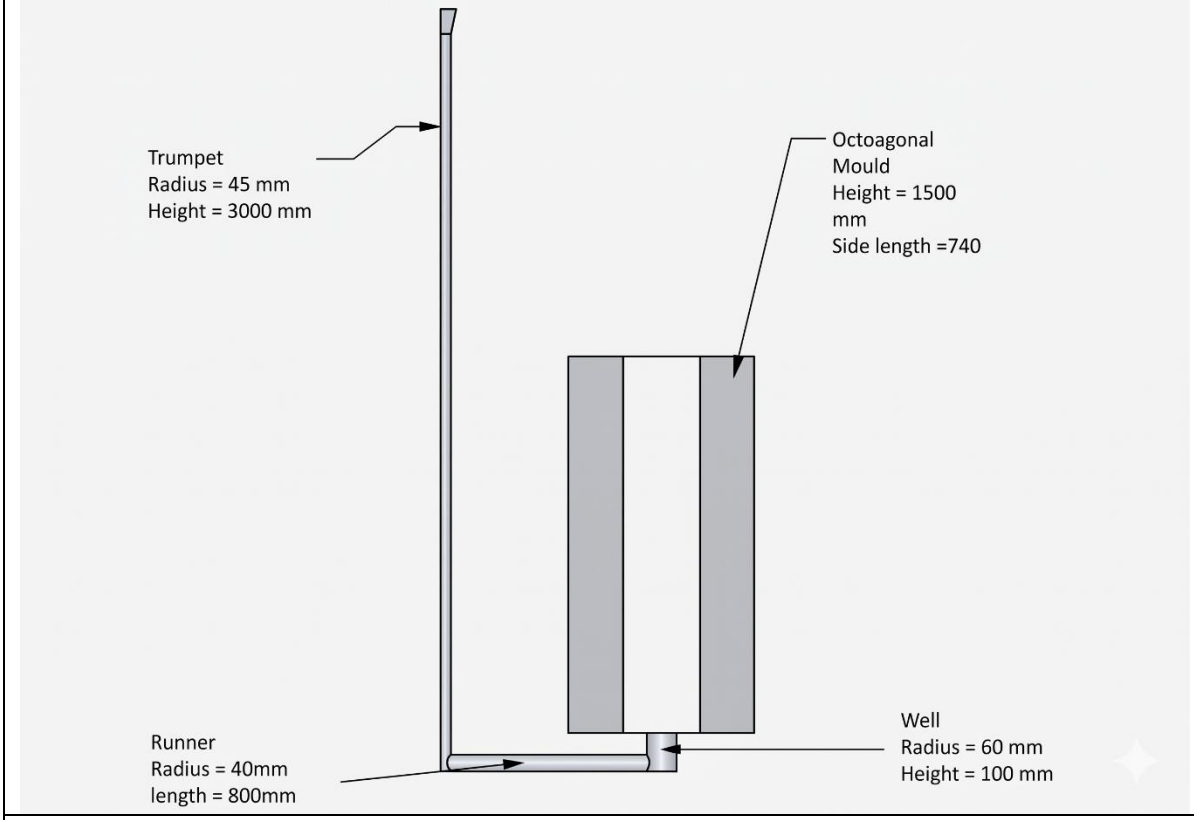

Figure 5: Longitudinal side view of the computational domain

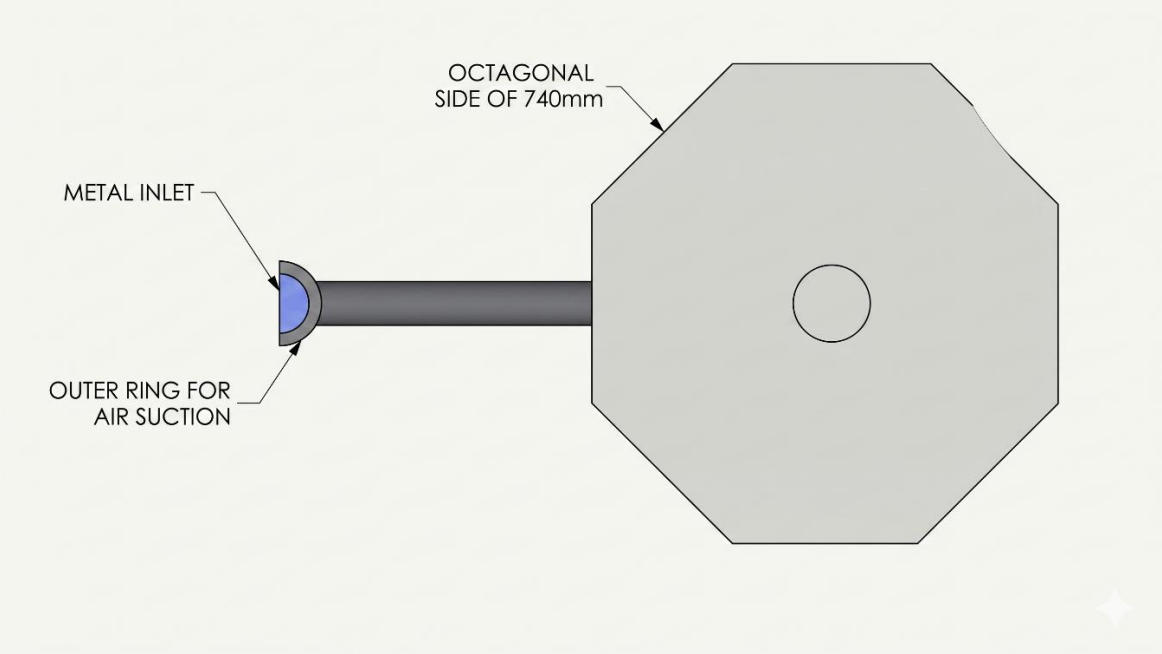

Figure 6: Top-down plan view of the casting assembly illustrating the dual-inlet system (Metal Inlet and Aspiration Ring) and the octagonal mould geometry

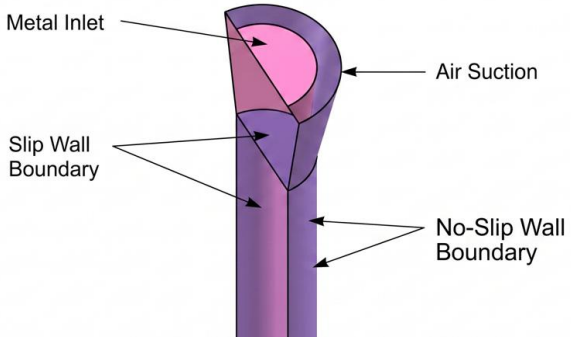

Figure 7: Trumpet Inlet Conditions

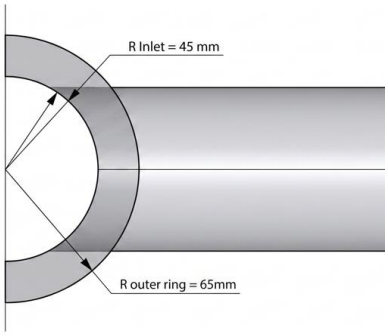

Figure 8: Top View of Trumpet

3.5.2 Inlet Velocity Derivation

The inlet velocity (v) is calculated to match the industrial pouring rate. Given that the simulation models a half-section, both the simulation mass flow rate (m^*_{sim}) and the inlet area (A_{sim}) are 50% of the physical total. The velocity magnitude, however, remains consistent.

Parameters:

- Total Mass Flow Rate (m^*): 110 kg/s [Based on an industrial plant operating data]
- Full Trumpet Radius (R): 45mm = 0.045 m [Based on an industrial plant operating data]
- Metal Density (ρ_{metal}): 7000 kg/m^3 [52, 55]

Total Inlet Area (A_{total}):

$$A_{total} = \pi R^2 = \pi (0.045)^2 = 0.0063617 \text{ m}^2$$

Continuity Equation:

$$v = m^*_{total} / (\rho_{total}. A_{total}) \quad (3.20)$$

Final Prescribed Velocity:

$$v = 110 / (7000 * 0.0063617) = 2.47 \text{ m/s}$$

The simulation prescribes a uniform fixedValue velocity of 2.47 m/s at the base of the trumpet half-section [4].

3.5.3 Thermophysical Properties at 1500°C

Following the Ideal Gas Law, assuming constant atmospheric pressure, the density of air at 1500°C (1773.15 K) is calculated from Standard Air Density (ρ_0) at the International Standard Atmosphere (ISA) sea-level reference temperature of 15°C (288.15 K) [52, 55].

The density of air decreases significantly at casting temperatures. Following the Ideal Gas Law, assuming constant atmospheric pressure, the density is inversely proportional to the absolute temperature (K):

$$\rho_1 = \rho_0 (T_0/T_1) \quad (3.21)$$

Where:

- Standard Air Density (ρ_0) at the International Standard Atmosphere (ISA) sea-level reference temperature of 15°C (288.15 K) = 1.225 kg/m
- Target Temperature (T_1) at 1500°C = 1773.15 K

$$\rho_{1500} = 1.225 (288.15/1773.15) = 0.20 \text{ kg/m}^3$$

The value utilized in the simulation dictionary is 0.19 kg/m^3, accounting for localized superheating and environmental humidity variations.

The solver requires kinematic viscosity (ν), derived from the dynamic viscosity (μ) and density (ρ):

$$\nu = \mu / \rho \quad (3.22)$$

Table 4: Material Properties and Transport Parameters [52, 55]

Property	Symbol	Metal (Liquid)	Air (Superheated)
Density ($kg/m^{3)}$	ρ	7000	0.19
Dynamic Viscosity (Pa. s)	μ	0.007	$5.7.\ 10^{-5}$
Kinematic Viscosity (m^2s)	ν	$1.0.\ 10^{-6}$	$3.0\ 10^{-4}$
Surface Tension (N/m)	σ	1.6	1.6

3.5.4 Boundary Condition Summary

The numerical constraints were defined to simulate a gravity-fed open system where air is displaced by the melt [54].

Table 5: Boundary Conditions

Patch	Velocity (U)	Pressure	Phase Fraction (α)
Inlet	fixedValue (2.47m/s)	fixedFluxPressure	fixedValue (1.0)
Outlet (Top)	pressureInletOutletVelocity	totalPressure (0 Pa)	inletOutlet (0.0)
Walls	noSlip	fixedFluxPressure	zeroGradient
Symmetry	symmetryPlane	symmetryPlane	symmetryPlane

3.6 Simulation Matrix and Parameters

This section provides a technical breakdown of the performance metrics used to evaluate the gating system and mould-filling characteristics. These indicators are crucial for predicting casting defects such as sand wash, porosity, and cold shuts.

To validate the numerical results obtained from the k-ε turbulence model, specific evaluation metrics are employed to characterize the filling phase.

Free-surface stability serves as a primary determinant of casting quality, as violent meniscus disturbances promote the mechanical entrainment of surface oxide films and air [56]. To evaluate interfacial behaviour during the initial filling transient, three hydrodynamic metrics are monitored: M1, M2, and M4. The core hump height (M1) measures the vertical displacement of the central liquid rise directly above the inlet, reflecting the magnitude of residual vertical kinetic energy entering the mould cavity. The extreme splash (M2) captures the absolute peak elevation attained by the melt, isolating the most violent transient surging event. Finally, the volumetric hump delta (M4) quantifies the height differential between this peak splash and the theoretical quiescent fill level. In accordance with criteria established by Campbell [56], a stable, defect-free meniscus rise requires an M4 value below 50 mm, whereas excursions exceeding 200 mm denote severe, fountain-like flow that directly promotes the folding and entrapment of deleterious oxide bifilms.

Wall Shear Stress (τ) quantifies the frictional force exerted by the molten metal on the mould walls. It is calculated based on the turbulent kinetic energy (k) near the boundary:

$$\tau = 0.3.\ \rho.\ K \tag{3.23}$$

High Wall Shear Stress indicates zones where the fluid velocity gradient is extremely steep, leading to mechanical scouring of the sand mould. Typically, 0-100 Pa is considered safe. Values exceeding 400-500 Pa pose a significant risk of Sand Wash, where sand particles are peeled off and entrained as inclusions in the casting [58].

Table 6: Materials and their safe operation limit

Material / Lining Type	Safe Operating Wall shear stress (Pa)	Critical Yield / Failure Limit (Pa)	Failure Mechanism & Consequence
Green Sand Mould Walls [58][56]	0 to 100 Pa (ideally <100–200Pa)	>400–500 Pa	Mechanical scouring and sand wash; loose sand grains wash into the melt as exogenous macro-inclusions.
Silica-Alumina Refractory Bricks Al_2O_3–SiO_2) [10][58][59]	< 800Pa	1,000 to 1,200 Pa (at 1500° C)	Tangential shear strips the softened silicate binder phase, releasing ceramic particles into the high-momentum stream.

The dead zone percentage quantifies the volume fraction of molten steel moving below a critical velocity threshold of 0.05 m/s. While meniscus quiescence is desired, excessive stagnation impedes global circulation and thermal homogeneity, increasing the risk of premature freezing and cold shut defects [59], optimized filling systems typically target a dead zone volume below 20%. Concurrently, deep air entrapment evaluates the volume fraction of gas bubbles drawn below the pool surface. Unlike transient surface-breaking aeration, deeply entrained gas cannot readily escape the rising column and is prone to capture during solidification, manifesting as subsurface blowholes and internal porosity; while ideally maintained at 0%, entrapment levels exceeding 15% are strongly correlated with elevated scrap rates [60]. Finally, the jet exit angle defines the orientation of the incoming melt relative to the mould floor. A conventional 90° (perpendicular) entry concentrates kinetic energy axially toward the meniscus, exacerbating fountain surging and refractory wall-climbing, whereas shallower entry angles (0° to 30°) redirect momentum horizontally along the base, allowing the developing liquid pool to dissipate incoming kinetic energy and promote stable, bottom-up filling [57].

3.7 Grid Convergence Test

To make sure the thesis follows proper numerical verification standards, this section presents a detailed mesh sensitivity analysis. It includes step-by-step calculations of the Grid Convergence Index (GCI), focusing on results that show good stability and low numerical error, in line with the ASME V&V 20-2009 standard [61].

3.7.1 Discretization and Mesh Statistics

The accuracy of the Computational Fluid Dynamics (CFD) results mainly depends on how the domain is discretized. To check mesh independence, three unstructured meshes were created: Fine (N_1), Medium (N_2), Coarse (N_3) and with a systematic refinement between them [61]. The main mesh details and the corresponding linear refinement ratios (r) are listed in Table 7.

Table 7: Mesh Analysis Metrics

Mesh Level	Cell Count (N)	Linear Refinement Ratio (r)	Average non-orthogonality	Max Skewness
Fine (N1)	338,337	$r_{21} = 1.275$	4.42°	2.58
Medium (N2)	163,162	$r_{32} = 1.177$	4.78°	2.41
Coarse (N3)	100,014	-	5.19°	2.34

The Linear Refinement Ratio is a scalar value that quantifies the change in spatial resolution between two different mesh densities (e.g., a Fine mesh vs. a Medium mesh). In a systematic grid convergence study, it is the primary factor used to scale discretization errors.

While the total number of cells changes cubically in 3D space, the GCI (Grid Convergence Index) methodology requires a linear measure of how much the edge length of a typical cell has changed. For unstructured or complex meshes, this is calculated as:

$$r = (N_1/N_2)^{1/d} \tag{3.24}$$

Where N_1 is the number of cells in the finer mesh, N_2 is the Number of cells in the coarser mesh and d is the dimensionality of the problem (typically 3 for mould simulations).

The linear refinement ratio is calculated as the cube root of the cell count ratio [63]:

$$r_{21} = (N_1/N_2)^{1/3} = (338{,}337/163{,}162)^{1/3} = 1.275$$

$$r_{32} = (N_2/N_3)^{1/3} = (163{,}162/100{,}014)^{1/3} = 1.177$$

Both ratios exceed the minimum threshold of 1.1, as recommended by Roache [63], ensuring that the discretization levels are sufficiently distinct to capture convergence trends.

Non-orthogonality is a geometric quality metric that measures the alignment between the vector connecting two adjacent cell centres (d) and the normal vector of the shared face (n). In a perfectly orthogonal mesh (like a perfect cube), these two vectors are perfectly parallel, resulting in an angle of 0^o. The non-orthogonality angle is defined by the dot product:

$$\theta = \cos^{-1} (d.n/|d|. |n|) \quad (3.25)$$

Average non-orthogonality is the arithmetic mean of the angles (theta) across all internal faces in the mesh. In OpenFOAM, high non-orthogonality increases numerical diffusion and forces the solver to apply non-orthogonal correctors to maintain stability. An average below 10^o-15^o is considered excellent for complex 3D gating systems, indicating that the pressure-velocity coupling in your simulation is highly accurate and requires minimal numerical correction.

Maximum skewness is a parameter that measures how distorted or asymmetric a cell is. It is defined by the distance between the geometric center of a face and the point where the line connecting the centres of the two neighbouring cells intersects that face. In an ideal case, such as a perfectly orthogonal cube, this line passes exactly through the face center, giving a skewness value of zero. For practical CFD simulations, a maximum skewness below 4.0 is generally considered very good, while values above 20.0 usually require local mesh refinement to avoid stability issues. Based on the check Mesh results, the meshes used in this study show very low skewness values, indicating good geometric quality (see Table 7).

3.7.2 Grid Convergence Index (GCI) Methodology

The Grid Convergence Index (GCI) is used to quantify the numerical uncertainty by estimating the error band within which the true continuum solution resides [61, 62]. The calculations are based on the Dead Zone (%) and Theoretical Filling Height (mm) at t = 4.0 s, which represent the global circulation and mass balance of the solver.

The GCI for the fine mesh is defined as:

$$CGI_{fine} = (F_s . e_{a,21)} / (r^p_{21} - 1) \quad (3.26)$$

In these formulations, F_s = 1.25 represents the recommended safety factor for a three-grid convergence study [61, 62], $e_{a,21}$ denotes the relative approximate error evaluated between the fine and medium mesh solutions, and p = 2.0 is the theoretical formal order of accuracy corresponding to the second-order spatial discretisation schemes implemented in the VOF solver [61, 62].

3.8 Metric Extraction and Data Processing

3.8.1 Surface Topography Metrics (The Hump Metrics)

To quantify surface stability and splashing, we developed three distinct Hump metrics. These metrics are critical for identifying the risk of cold shuts or surface bifilms caused by excessive turbulence.

M1 (Statistical Core Hump) Quantifies the vertical elevation of the coherent liquid metal core above the mean pool surface. By evaluating the 99th percentile of the liquid phase distribution, this metric filters out isolated numerical spray and detached airborne droplets, isolating the macroscopic bulk surge of the advancing melt front.

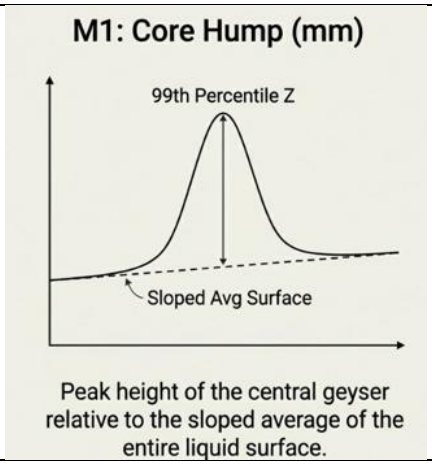

Figure 9: Statistical Core Hump (M1)

M2 (Extreme Splash Height) is the maximum vertical reach of the metal during transient sloshing

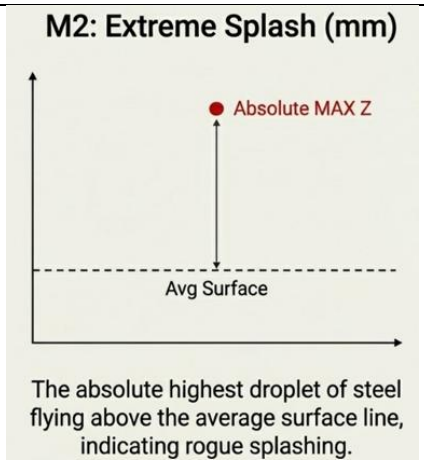

Figure 10: Extreme Splash Height (M2)

M4 (Volumetric Hump) is total deviation from an ideal, perfectly flat fill based on injected volume.

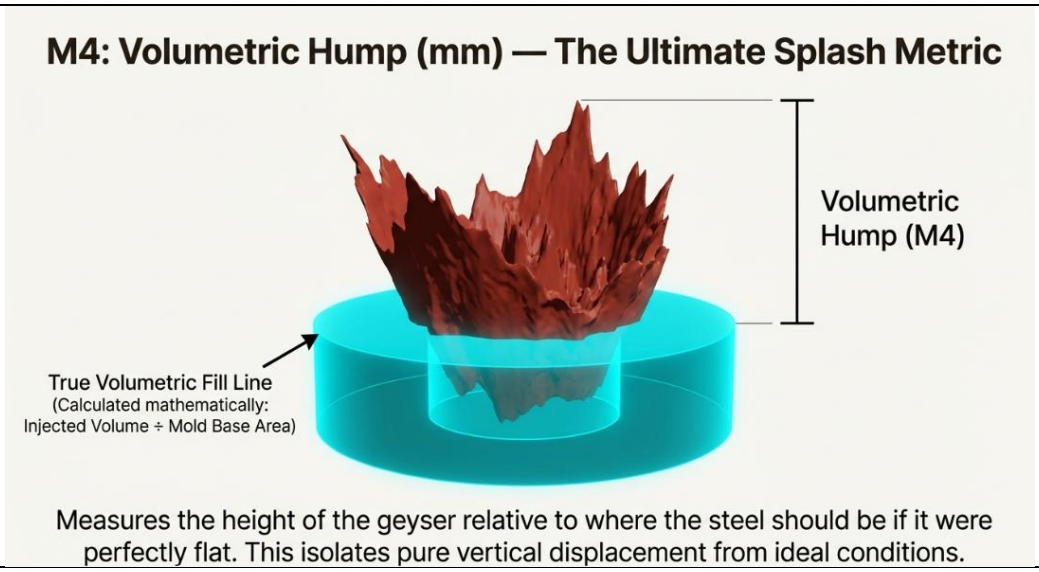

Figure 11: Volumetric Hump (M4)

3.8.2 Boundary Layer Interaction and Erosion Risk

Refractory erosion risk and boundary layer interactions are evaluated using the wall shear stress (τ_w) and maximum near-wall velocity. Within the Standard k– ε framework under logarithmic-layer local equilibrium, τ_w quantifies the tangential frictional force exerted by the flowing steel on the refractory lining, which should ideally remain below 100–200 Pa to suppress refractory degradation and sand wash. Concurrently, the maximum wall velocity captures the peak fluid speed within the 20 mm near-wall boundary layer, where velocities exceeding 1.0 m/s significantly elevate the likelihood of mechanical erosion.

Internally, the bulk flow structure and casting quality are governed by the jet exit trajectory, dead zone percentage, and deep air entrapment. The jet exit angle defines the orientation of the incoming melt core relative to the mould base, dictating whether momentum drives vertical fountain formation or dissipates horizontally across the developing pool. Within the melt volume, the dead zone percentage identifies stagnant regions moving below 0.05 m/s, where insufficient convective mixing exacerbates thermal gradients and increases susceptibility to premature freezing defects. Finally, deep air entrapment quantifies the volume fraction of entrained gas ($\alpha < 0.5$) submerged at least 50 mm below the free surface; because these deep-seated bubbles cannot readily disengage before the solidification front advances, they serve as the primary catalyst for internal oxide bifilms and gas porosity.

$$\tau_w = C_\mu^{1/2}\, 1/2\rho k \quad (C_\mu = 0.09) \qquad (3.27)$$

3.8.3 Data Extraction Methodology and Reference Fill Levels

When comparing different runner angles and inlet velocities, evaluating flow metrics at fixed points in time is not reliable. Because changes in gating geometry and inlet velocity alter the volumetric flow rate (Q) and local acceleration into the cavity, identical timestamps do not correspond to the same amount of steel delivered into the mould.

To remove this time bias and compare the hydrodynamic behaviour of each case on equal footing, a volumetric normalization approach was used instead. Data was extracted at ten discrete milestones based on the theoretical fill height (H_{theo}) of the liquid metal inside the mould cavity. These reference heights span from an initial shallow pool of 30 mm up to an established 120 mm pool depth, sampled at 10 mm intervals. The target reference volumes (V_{ref}) were determined assuming an idealized flat, stationary liquid pool based on the mould cavity geometry:

$$V_{ref} = A_{mould} \times H_{theo} \tag{3.28}$$

where A_{mould} represents the cross-sectional area of the mould cavity, defined as 0.454 m^2 based on the internal mould dimensions. During the transient multiphase simulation, the cumulative volume of the metal phase delivered to the mould was monitored continuously. Whenever the volume of metal reached one of the ten target volumes outlined in Table 8, a full spatial data snapshot was compiled and extracted for post-processing.

Table 8: Theoretical Reference Heights and Corresponding Liquid Metal Volumes

Sample Point	Reference Fill Height ($H_{theoretical}$) [mm]	Theoretical Metal Volume ($V_{reference}$) (m^3)	Physical Filling Stage
1	30	0.01362	Initial Impingement / Stream Break-in
2	40	0.01816	Jet Deflection and Base Cushioning
3	50	0.0227	Transition to Wall-Climbing Regime
4	60	0.02724	Developed Boundary Layer Layering
5	70	0.03178	Intermediate Recirculation Cell Setup
6	80	0.03632	Mid-stage Equilibrium Filling
7	90	0.04086	Steady-State Pool Damping
8	100	0.0454	Upper Ingot Core Development
9	110	0.04994	Deep-Pool Mass Circulation
10	120	0.05448	Final Monitored Steady Filling Stage

3.9 Models Utilized in the simulation

Figure 12: Side view of the 90º Runner Model.

Figure 13: Side view of the 85º Runner Model.

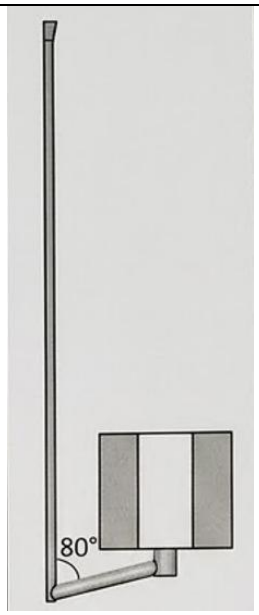

Figure 14: Side view of the 80º Runner Model.

Figure 15: Side view of the 75º Runner Model.

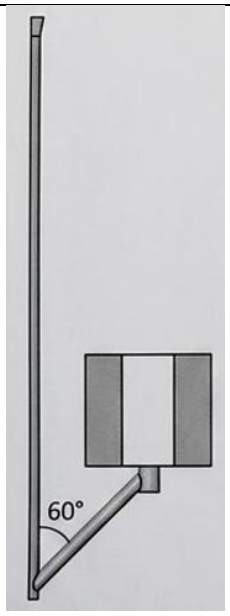

Figure 16: Side view of the 60º Runner Model.

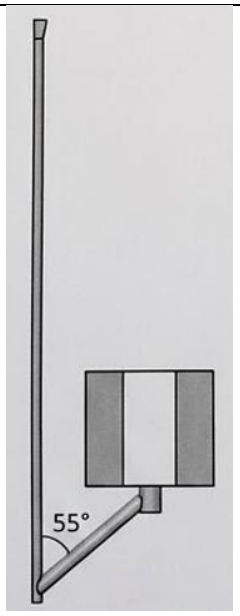

Figure 17: Side view of the 55º Runner Model.

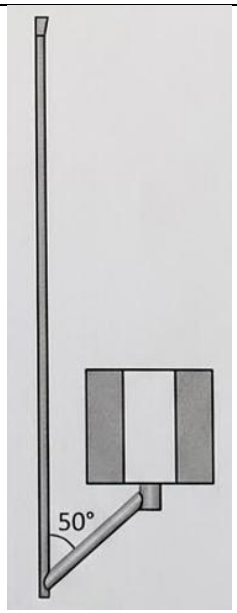

Figure 18: Side view of the 50º Runner Model.

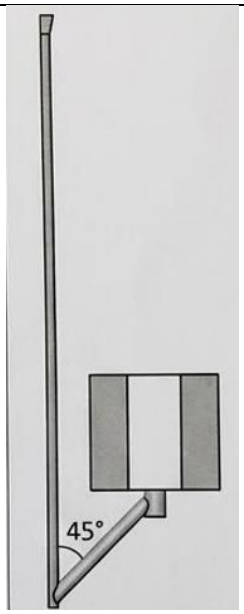

Figure 19: Side view of the 45º Runner Model.

Chapter 4: Results and Discussions

The chapter is structured into five sequential sections that progress from numerical verification to baseline analysis and parametric optimization. Numerical verification through Grid Convergence Index (GCI) calculations across three grid levels, Characterization of the hydrodynamic flow regime through dimensionless analysis of Reynolds, Weber, and Froude numbers, establishing the supercritical and turbulent nature of the incoming melt stream, Details about the flow field topology, surface topography, boundary layer wall shear stress, and stagnant volume accumulation for the standard 90° perpendicular baseline configuration at 2.47 m/s and a comparative investigation across eight runner entry angles, documenting the hydrodynamic anomaly termed the 55° violence peak and demonstrating the circulation optimization achieved by the 45° acute runner.

4.1 Grid Convergence Calculations

Calculations are done using the data obtained from the simulation done for fine, medium and coarse mesh as shown in the table 9.

Table 9: the data obtained from the simulation done for different mesh

Mesh	Dead Zone %	Theoretical Fill Height (mm)
Coarse	38.71	57.41
Medium	40.99	60.66
Fine	43.11	62.90

4.1.1 Global Flow Stability: Dead Zone (%)

The Dead Zone metric identifies the volume percentage of metal with stagnant velocity (U < 0.05 m/s). The data from the simulation gave us the following values:

$\varphi_1 = 43.11$ (Fine), $\varphi_2 = 40.99$ (Medium) and $\varphi_3 = 38.71$ (Coarse)

Relative Approximate Error ($e_{a,21}$):

$$e_{a,21} = | (\varphi_1 - \varphi_2)/ (\varphi_1) | = | (43.11 - 40.99) / (43.11) | = 4.92\%$$

Fine Grid Uncertainty (GCI_{21}):

$GCI_{21} = (1.25 * 0.0492)/ (1.275^2 - 1) = 0.0615/0.6256 = 9.83\%$

4.1.2 Theoretical Filling Height (mm)

This metric evaluates the consistency of the poured volume relative to the mould area. The data from the simulation gave us the following values:

$$\varphi_1 = 62.90 \text{ (Fine)}, \varphi_2 = 60.66 \text{ (Medium) and } \varphi_3 = 57.41 \text{ (Coarse)}$$

Relative Approximate Error $e_{a,21}$):

$$e_{a,21} = | (\varphi_1 - \varphi_2)/ (\varphi_1) | = | (62.90 - 60.66) / (62.90) | = 3.56\%$$

Fine Grid Uncertainty (GCI_{21}):

$$GCI_{21} = (1.25 \times 0.0356)/ (1.275^2 - 1) = 0.0445/0.6256 = 7.13\%$$

4.1.3 Synthesis and Discussion

The GCI analysis shows that the overall filling parameters are numerically stable. Both the Dead Zone (%) and Theoretical Level values lie within a relatively small uncertainty range of about 10-12%, indicating that the solution has become largely independent of the mesh for global flow behaviour [63]. Although the volumetric results showed some non-monotonic variation between the coarse and medium meshes, the results from the medium and fine meshes are much closer. This suggests that the Fine mesh (338,337 cells) is starting to capture more detailed transient interface effects, which are important for predicting air entrainment and local splashing. Based on this, the Fine mesh was chosen for all final simulations to ensure better accuracy and representation of the physical phenomena.

4.2 Dimensionless Flow Analysis

This section characterizes the flow regime within the gating system by calculating the primary dimensionless numbers. These ratios allow for a quantitative comparison of the relative importance of inertial, viscous, surface tension, and gravitational forces, providing a firm theoretical basis for the observed surface instabilities and turbulence. To quantify the physics at the inlet, the Hydraulic Diameter (D_h) of the half-trumpet geometry must first be established. For a non-circular or bisectional duct, D_h is defined according to Campbell [56] as:

$$D_h = 4A/P \quad (4.1)$$

Parameters:

- Area (A): 0.00318 m^2 (Half-circle with R = 45 mm)
- Wetted Perimeter (P): $\pi R + 2R = \pi (0.045) + 2(0.045) = 0.231$ m
- Hydraulic Diameter (D_h): 4 (00318/0.231) = 0.055 m

4.2.1 Reynolds Number (Re)

The Reynolds number represents the ratio of inertial forces to viscous forces, serving as the primary criterion to determine whether a flow is laminar or turbulent [66].

$$R_e = \rho v D_h / \mu \quad (4.2)$$

Using the metal properties at 1500°C (ρ = 7000 kg/m^3, μ = 0.007 Pa. s) and the inlet velocity of 2.47 m/s:

$$R_e = (7000 \times 2.47 \times 0.055)/0.007 = 135{,}850$$

With Re >> 4000, the flow entering at the inlet is fully turbulent [66]. This high degree of turbulence validates and necessitates the application of two-equation Reynolds-Averaged Navier–Stokes (RANS) closure models, such as the standard k-ε framework, to accurately capture energy dissipation, eddy viscosity, and complex recirculation zones within the runner system [29], [36].

4.2.2 Weber Number (W_e)

The Weber number evaluates the ratio of inertial forces to surface tension forces, which is critical for predicting the physical breakup of a liquid metal interface, liquid shearing, and subsequent droplet formation [56].

$$W_e = (\rho v^2 D_h)/ \sigma \quad (4.3)$$

Using the prescribed surface tension (σ = 1.6 N/m):

$$W_e = (7000. (2.47)^2 0.055)/ (1.6) = 1{,}467$$

In metal casting systems, a Weber number exceeding a critical threshold (We > 100) indicates that inertial forces heavily dominate surface tension, rendering the liquid interface highly unstable [28], [56]. A value of 1,467 demonstrates that the metal stream is intensely susceptible to splashing, atomization, and fragmentation upon hitting the mould cavity, directly dictating the severe volumetric hump (M4) fluctuations observed during the initial filling phase [56].

4.2.3 Froude Number (F_r)

The Froude number represents the ratio of inertial forces to gravitational forces, describing the hydrodynamic behaviour of free-surface flows and the capacity for wave propagation [66].

$$Fr = v/ ((g\ D_h)^{1/2}) \quad (4.4)$$

Using gravitational acceleration ($g = 9.81\ m/s^2$):

$$Fr = 2.47/ (9.81 \cdot 0.055)^{1/2} \approx 2.47/0.734 \approx 3.36$$

A Froude number greater than 1.0 indicates the flow regime as supercritical or rapid [66], [67]. In this regime, surface waves cannot propagate upstream against the current. A value of 3.36 confirms that the momentum of the incoming melt will result in a pronounced mounding or geyser effect at the center of the mould, as gravity alone is insufficient to instantly flatten the intense, high-momentum incoming fluid surge [56].

Table 10: Dimensionless Numbers and their Values

Number	Value	Regime	Physical Implication
Reynold (R_e)	135,850	Fully Turbulent	High eddy viscosity; requires turbulence modelling.
Weber (W_e)	1,467	Unstable Interface	High risk of splashing and droplet formation.
Froude (F_r)	3.36	Supercritical	High momentum surge; uneven surface levelling

4.3 Characterization of the Baseline Model (90° Runner, 2.47 m/s)

The baseline case establishes the reference behaviour for the standard perpendicular gating configuration. The evolution of the filling metrics as the mould level rises from 30 mm to 120 mm is summarised below in the table.

Table 11: Performance Metrics for Baseline Model by Theoretical Fill Height

Theo. Height (mm)	M1 (Core Hump) (mm)	M2 (Splash Height) (mm)	M4 (Volumetric Hump) (mm)	Max Wall Shear Stress (Pa)	Dead Zone (%)	Air Percent (%)
30	99.86	159.84	284.76	0	75	46.25
40	95.42	155.4	274.9	36.84	61.03	46.76
50	91.71	181.69	294.96	41.7	59.78	52.65
60	87.37	177.26	276.43	47.24	51.34	50.81
70	114.92	174.94	264.2	44.24	54.36	42.41
80	104.91	194.93	285.64	49.05	51.37	47.94
90	98.46	158.47	236.06	36.98	48.52	46.26
100	89.54	179.53	255.17	48.7	52.63	46.84
110	115.58	175.58	247.9	43.13	54.54	45.5
120	112.24	202.24	268.82	40.65	47.76	24

4.3.1 Flow Field Topology and Velocity Vector Dynamics

When the liquid steel leaves the horizontal runner and passes through the vertical ingate, it shoots straight up along the center axis ($\theta = 90°$) [12]. This vertical jet moves directly upward through the rising pool of metal [10]. Once it hits the top surface, a high-pressure stagnation points forms right above the ingate, which slows the jet down and turns its kinetic energy into pressure [28]. Because the metal is trapped inside the octagonal mould, this pressure pushes the fluid outward across the mould floor like a wall-jet [7]. When this outward flow hits the outer corners and walls [13], it has nowhere else to go and gets forced upward along the sides [6]. This creates a fast upward-moving stream of metal along the mould walls [11], while the area in the middle around the central jet stays relatively slow and forms a recirculation zone

[13]. Basically, this sets up a flow pattern where liquid rushes up the outer walls while the central area around the jet remains slow and stagnant.

4.3.2 Free-Surface Topography and Multiphase Interface Evolution

Because fluid momentum in the 90° baseline is directed toward the perimeter, the liquid–air interface deforms heavily instead of rising as a flat, level pool. The phase boundary was tracked using the Volume of Fluid method (α_metal), focusing on the perimeter peak height, mean pool surface height, and transient splash overshoot (M4). Right from the initial stage (H_{theo} = 30 mm), the metal climbs the outer walls much faster than it accumulates in the core, with the perimeter peak reaching 159.84 mm while the mean surface height is only 99.86 mm. During this early stage, the incoming vertical jet also causes severe initial splashing, with M4 reaching 284.76 mm at 30 mm fill height and peaking at 294.96 mm at the 50 mm mark before collapsing back into the bath. As filling progresses through the 60–100 mm milestones, this height difference does not smooth out; instead, the continuous upward flow along the walls keeps the meniscus locked into a deep, bowl-shaped profile. By the 120 mm milestone, the perimeter reaches 202.24 mm while the mean pool level is only 112.24 mm.

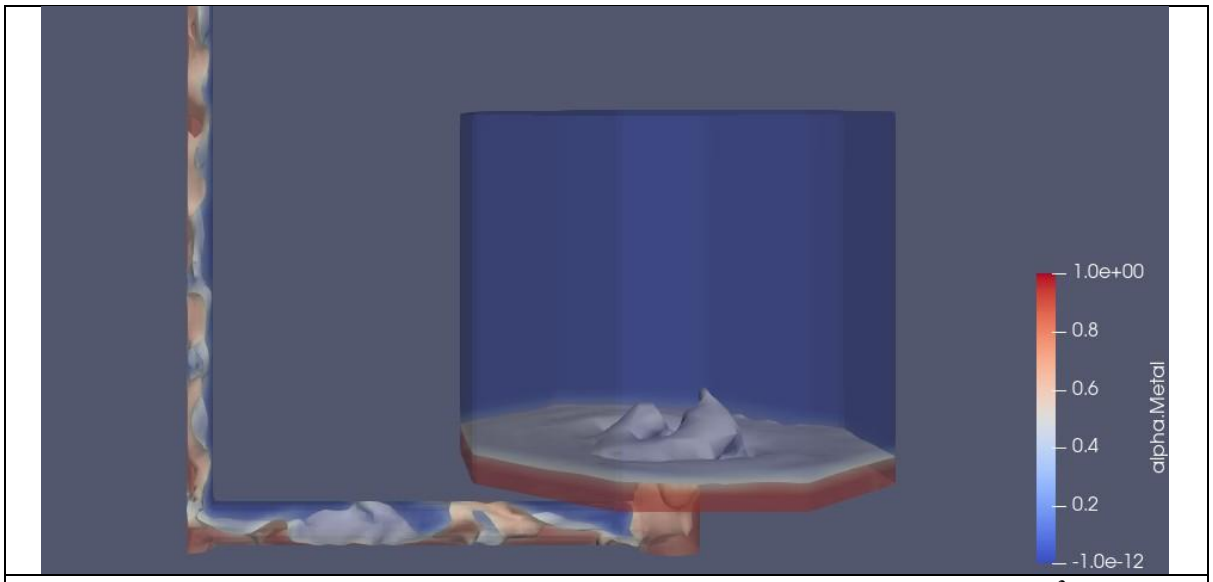

Figure 20: Metal interface (α = 0.5) at the mold filling volume = 0.0227 m^3

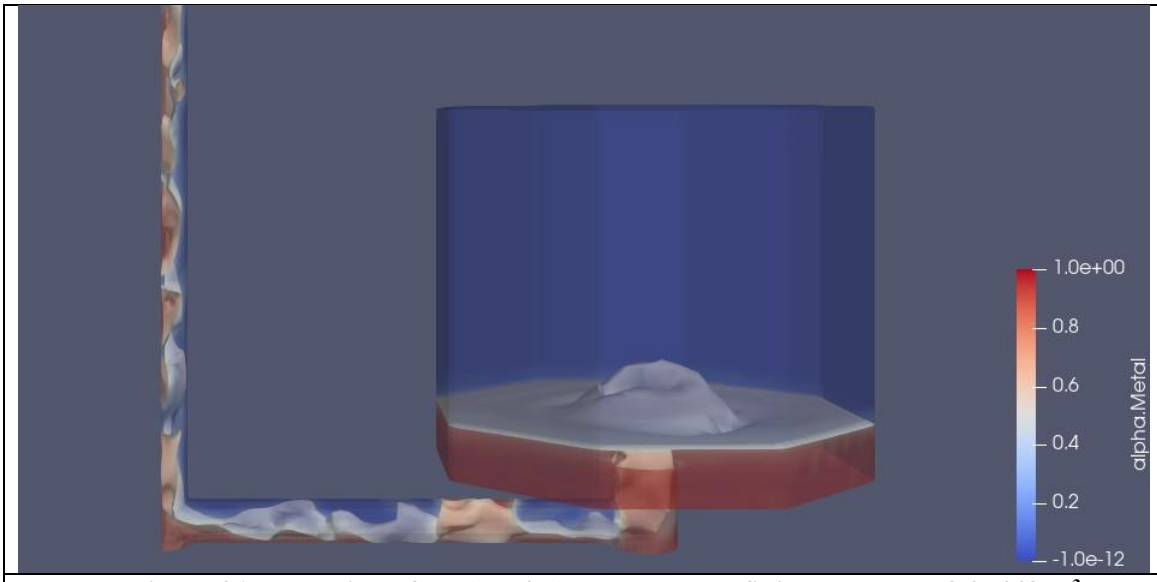

Figure 21: Metal interface (α = 0.5) at the mould filling volume = 0.05448 m^3

Figures 20 and 21 show the evolution of the metal free surface (α_{metal}=0.5) in the octagonal mould at theoretical fill heights of 50 mm and 120 mm. At 50 mm (V = 0.0227 m^3), the incoming vertical jet strikes the shallow liquid bath directly, creating a strong central fountain. The metal then spreads outward across the mould floor and begins climbing the outer walls. By 120 mm (V = 0.05448 m^3), the surface still has not settled into a flat, planar pool. Instead, the continuous flow from the 90° ingate keeps the meniscus locked in a pronounced bowl shape, with the interface reaching 202.24 mm along the perimeter while the center remains at only 112.24 mm. A 90.0 mm height difference across the surface. This height gap confirms that vertical momentum is steadily funnelled toward the walls, sustaining an upward perimeter fluid curtain and steep velocity gradients near the surface. In an actual casting operation, this flow pattern creates a constant risk of shearing and entraining the protective mould flux layer into the melt, showing the hydrodynamic instability of the standard 90° ingate.

4.3.3 Boundary Layer Friction and Refractory Protection Mechanics

Although the 90° baseline produces noticeable surface turbulence, its main operational advantage is minimal refractory wear [23]. Because the incoming jet enters perpendicularly, its momentum splits symmetrically across the mould floor without directly striking any single vertical wall at an angle [12, 30]. As a result, the localized wall shear stress (WSS) stays very low throughout filling, reaching a peak transient value of only 49.05 Pa. This low stress level occurs because a slow recirculation zone develops around the ingate perimeter, acting as a fluid cushion that shields the refractory lining from the high-velocity jet core [13, 58]. Since 49.05 Pa is well below the 1000–1200 Pa mechanical yield limit for typical silica–alumina refractory bricks at 1500 °C [58, 59], the incoming stream does not generate enough mechanical force to cause refractory damage. Consequently, the 90° configuration carries virtually no risk of sand-wash erosion or ceramic inclusion pickup from the mould boundaries [10].

4.3.4 Volumetric Dead Zone Tracking and Thermal Consequences

The main drawback of the 90° baseline setup becomes clear when evaluating the internal fluid circulation across the mould cavity [30]. Here, a dead zone is defined as any region within the liquid steel volume ($\alpha_{metal} \geq 0.9$) where the local velocity magnitude drops below 0.05 m/s [66]. By the final evaluation milestone (H_{theo} = 120mm), volumetric integration shows that 47.76% of the accumulated steel remains stagnant. This lack of bulk movement is a direct result of the symmetric upwelling pattern, which isolates the lower-core regions of the octagonal mould from active convective transport [7].

From a metallurgical perspective, having nearly half the metal volume sit stagnant creates a serious defect risk [16]. Liquid steel relies on convective circulation to distribute heat evenly throughout the mould [28]. In these stagnant regions, the melt quickly loses superheat through conduction to the cold mould walls without being replenished by fresh, hot metal from the incoming jet [12, 51]. This localized chilling can cause premature dendritic freezing and crust formation below the rising surface [16]. As filling continues, incoming liquid metal can fold over these semi-solidified layers, forming cold-shuts or laps that weaken the internal structure of the final forged ingot [51, 56].

While a configuration with a high dead-zone fraction might look safe on the surface because splashing (M4) is low and refractory wear is minimal (WSS = 49.05 Pa), achieving a quiet meniscus through widespread stagnation simply trades surface disturbances for internal thermal and structural defects. An optimized geometry, such as the 45° runner (which lowers the dead-zone volume to 28.60%), demonstrates that effective bottom circulation can be established without compromising refractory protection.

4.4 Comparative Study: Influence of Runner Angle

Varying the runner angle from the 90° baseline down to an acute 45° angle substantially alters filling behaviour. Table 12 summarises the peak intensities recorded across the full filling duration (30–120 mm).

Table 12: Master Comparison of Peak Filling Metrics for Variable Runner Angles

Runner Angle (°)	Peak M4 (mm)	Peak Wall Shear Stress (Pa)	Final Dead Zone (%)	Max Exit Angle (°)
90 (Baseline)	294.96	49.05	47.76	47.87
85	330.87	593.61	43.71	79.57
80	389.53	757.34	46.1	68.69
75	375.08	1347.47	34.14	77.1
60	401.23	1197.9	33.13	58.54
55	425.77	1763.11	35.9	70.8
50	370.58	860.64	30.19	59.21
45	354.69	741.35	28.6	35.45

4.4.1 Asymmetric Momentum Transport and Symmetry Breaking

Lowering the runner entry angle below 90° breaks the flow symmetry at the ingate [18]. Instead of spreading out evenly across the floor upon entry, the liquid steel exits as an angled, asymmetric jet that keeps much of its horizontal momentum [8]. This alters how kinetic energy distributes inside the mould cavity [30]. Rather than pushing fluid upward along all outer walls simultaneously, the angled runner steers the main stream along a specific path, sweeping across the mould floor before beginning to rise [18].

To track the resulting surface disturbances, the M4 metric was used to measure the maximum vertical overshoot relative to the theoretical fill height [9]. The results show a clear non-monotonic trend between runner angle and surface stability, highlighted by a sharp peak at 55°. As the runner angle decreases from 90° to 75° and 65°, the jet trajectory angle (θ) drops to 73.12° and 64.55°, respectively [8]. This shift directs upward momentum toward the far mould walls, steadily increasing initial splashing [18]: M4 rises from the 294.96 mm baseline to 375.08 mm at 75° and 442.80 mm at 60°. At 55°, the flow becomes particularly unstable [60].

At this angle, the incoming jet trajectory happens to point straight toward the adjacent vertical wall instead of striking the mould floor first where its momentum would normally dissipate.

This direct wall impingement forces the steel violently upward along the mould face [6], pushing M4 to 425.77 mm during the early stages of filling. As this large surging wave folds back into the pool, it entrains significant amounts of air, creating a strong risk of gas porosity and re-oxidation defects [10, 51].

Decreasing the angle further to 45°, however, shifts the flow into an entirely different regime [18]. At 45°, the trajectory angle flattens to $\theta = 35.45^{o}$, forcing the incoming stream to run parallel to the mould floor as a stable, horizontal sheet [8]. Because momentum is spread across the broad base rather than focused on a vertical wall, the initial splash height drops back down to an M4 of 354.69 mm. While this is still moderately higher than the 90° baseline, it safely avoids the severe peak seen around 55°.

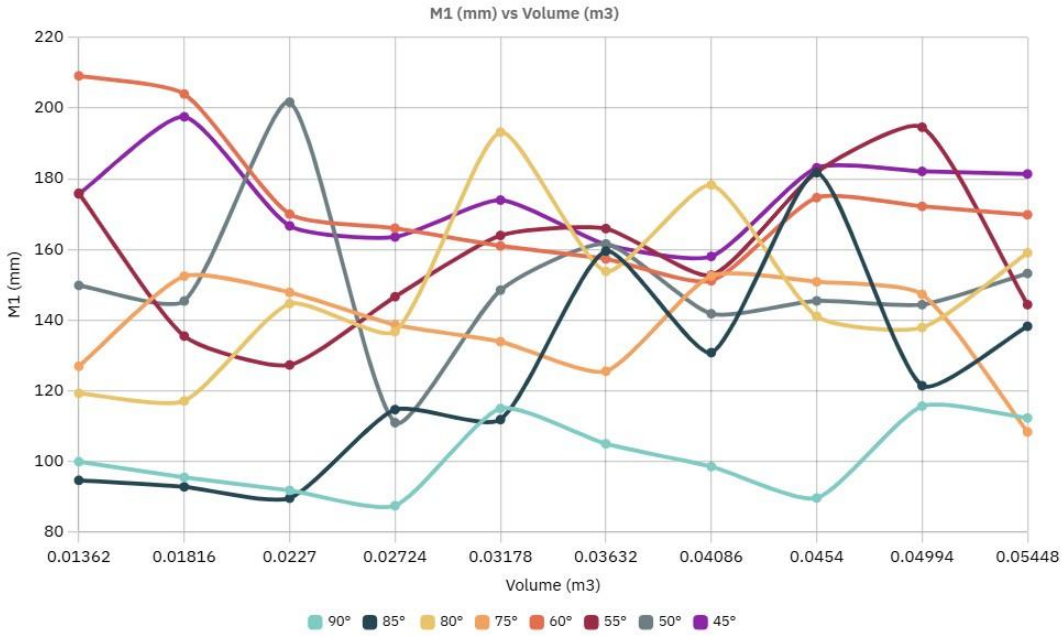

Figure 22: M1 (Core Hump) vs Volume (For different angled runners)

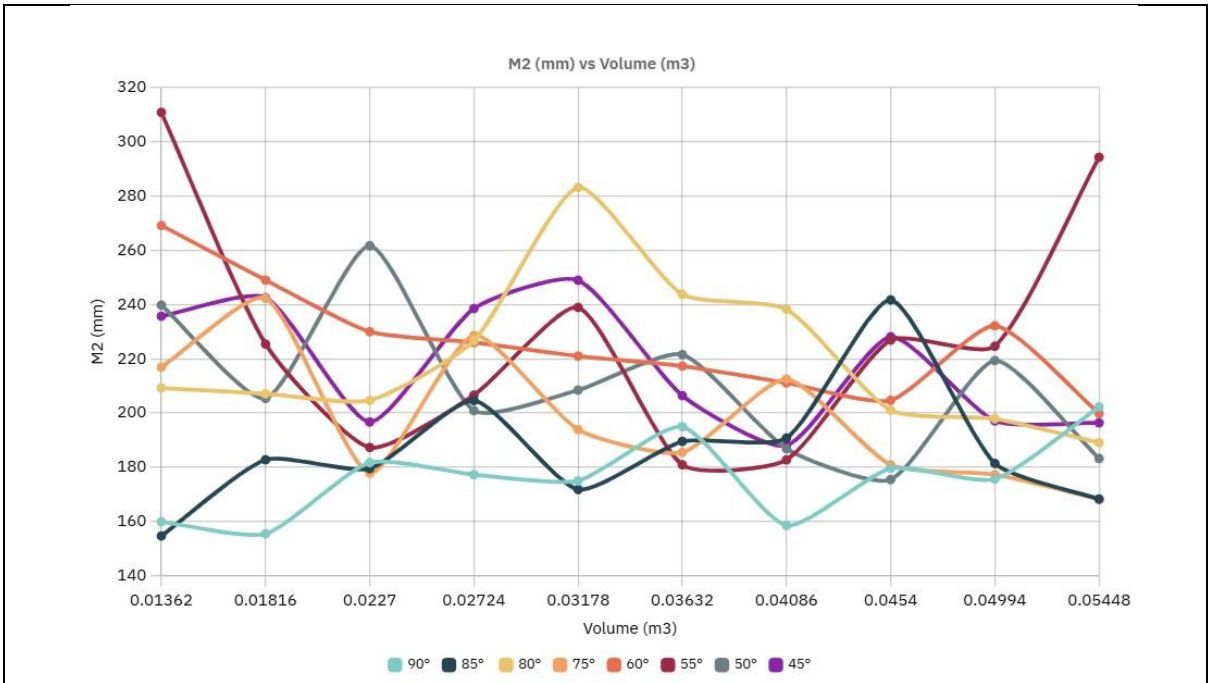

Figure 23: M2 (Splash) vs Volume (For different angled runners)

Figures 22 and 23 plot the transient evolution of the 99th-percentile peak interface height (M1) and the arithmetic mean pool level (M2) across ten volumetric filling steps for runner angles from 90° down to 45°. For M1, the 90° and 85° setups maintain relatively low peak heights, generally staying below 120 mm during the early stages of filling. In contrast, the intermediate 60° and 55° angles show noticeable fluctuations, with wave surges reaching between 190 mm and 209 mm. The mean surface level (M2) exhibits similar oscillations during the initial 0.013–0.031 m^3 filling window, where the 55° case hits a maximum mean elevation of 310.88 mm before damping out as the metal depth increases. These trends reflect the flow asymmetry that develops when reducing the runner angle from 90°. While the perpendicular runner creates a fairly symmetric upwelling around the perimeter, angled runners push fluid momentum in a preferred direction, setting up sweeping waves that slosh back and forth across the mould cavity until the deepening liquid bath dampens the surface motion at higher fill volumes.

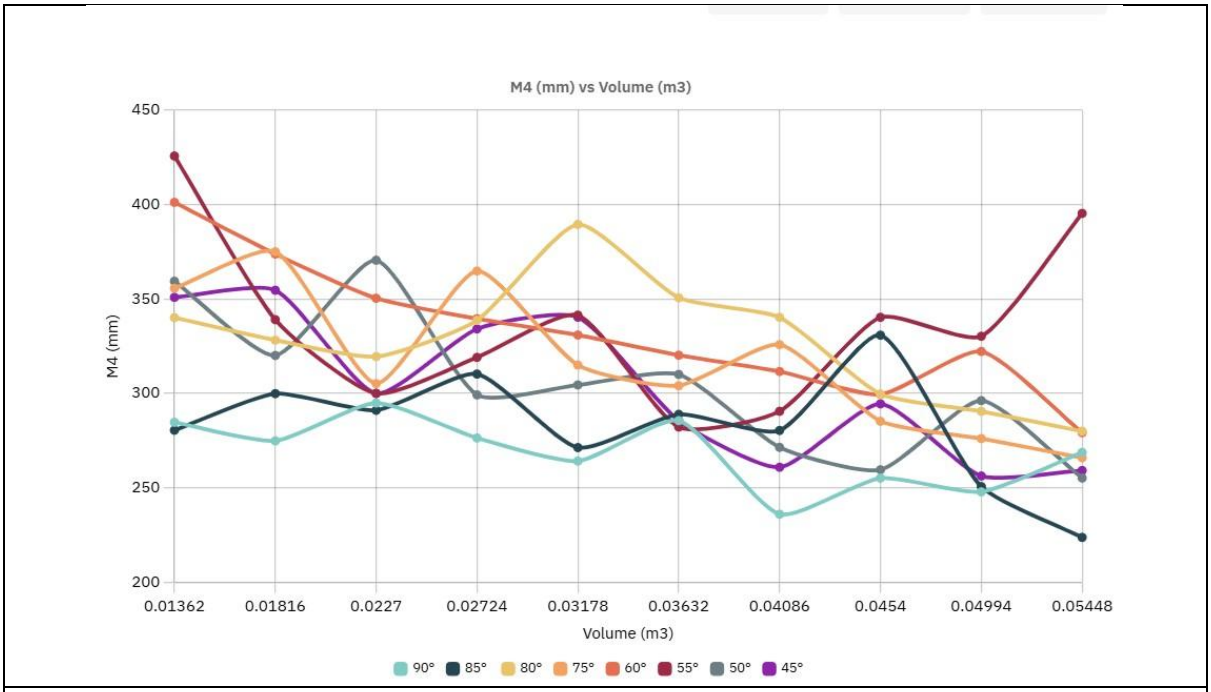

Figure 24: M4 (Volumetric Hump) vs Volume (For different angled runners)

Figure 24 compares the volumetric hump metric (M4) across the tested runner configurations, quantifying transient surface deformation and splashing relative to an ideal flat filling pool. For almost all angles, the M4 values follow a downward trend as the filling volume increases from 0.01362 m^3 to 0.05448 m^3, reflecting the damping effect of the deepening metal bath on surface disturbances. However, the 55° configuration displays a pronounced anomaly: it spikes to an extreme initial overshoot of 425.77 mm at V = 0.0133 m^3, fluctuates erratically, and surges again to roughly 395 mm near the end of the evaluated sequence. In contrast, the 45° runner exhibits a much more stable response, starting with a bounded initial overshoot of 354.69 mm that decays smoothly down to 256.31 mm, demonstrating that this angle effectively limits surface turbulence after the opening surge.

4.4.2 Wall Shear Stress Distribution and Relative Refractory Wear Risks

The localized Wall Shear Stress (WSS) data follows a non-monotonic trend similar to the surface metrics, indicating an elevated friction zone between 75° and 55° [58, 64]. As the runner angle is reduced from the 90° baseline (49.05 Pa), peak localized wall shear stress increases substantially to 593.61 Pa at 85° and 1347.47 Pa at 75°. This increase is driven by the asymmetric flow alignment, which concentrates fluid momentum along the solid boundaries [30]. At the 55° configuration, direct impingement of the jet core onto the nearby vertical wall creates steep velocity gradients ($\partial Ut/\partial n$), driving the peak localized Wall shear stress to a maximum of 1763.11 Pa.

In an industrial casting environment, localized stress concentrations of this scale point toward a heightened risk of refractory wear, where high fluid friction could strip the binder matrix from refractory bricks and release ceramic particles into the melt as exogenous inclusions [10,

56, 58]. However, these numerical wall shear stress values should be interpreted as relative tendencies rather than absolute predictions of refractory failure. Because CFD calculations do not capture high-temperature chemo-mechanical wear or varying brick grades directly, these stress peaks mainly serve to highlight relative risk across the geometries. Experimental validation or plant trials would be necessary to confirm actual erosion rates under operational conditions at 1500 °C. Decreasing the runner angle further to 45° reverses this trend [18]. Because the stream travels parallel to the mould floor rather than striking the vertical wall directly, incoming kinetic energy is dissipated more gradually through fluid–fluid shear [66]. Consequently, the maximum WSS drops back to 741.35 Pa roughly a 58% reduction compared to the 55° peak. While this value remains higher than the perpendicular baseline, the 45° design presents a noticeably lower risk profile than the intermediate angles, demonstrating how directional bottom flow can be established while keeping boundary stresses comparatively low.

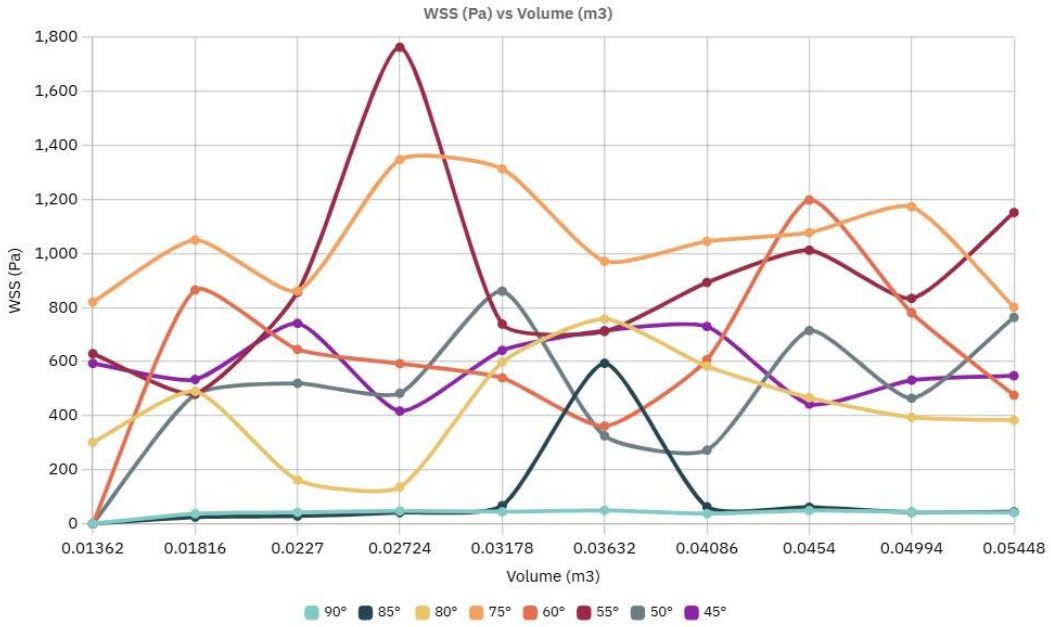

Figure 25: Wall shear stress vs mould filling Volume (For different angled runners)

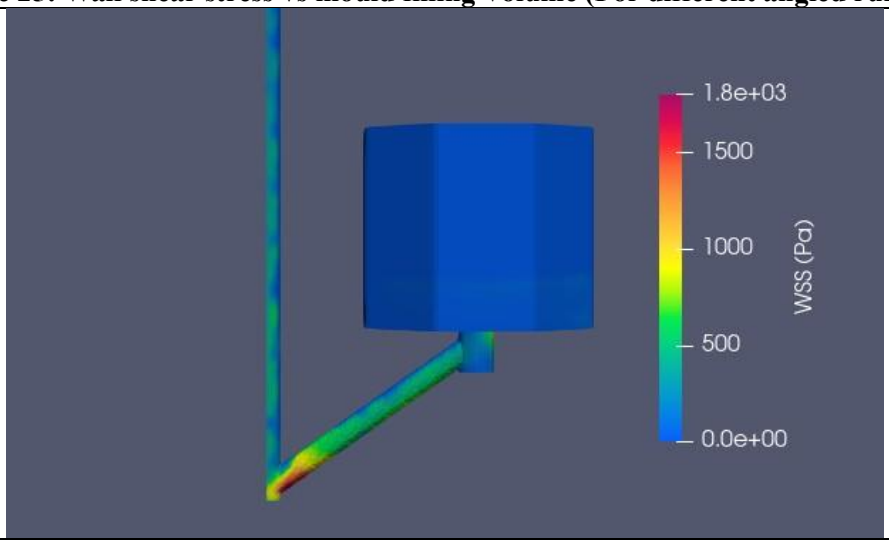

Figure 26: contour map of Wall Shear Stress 55º runner

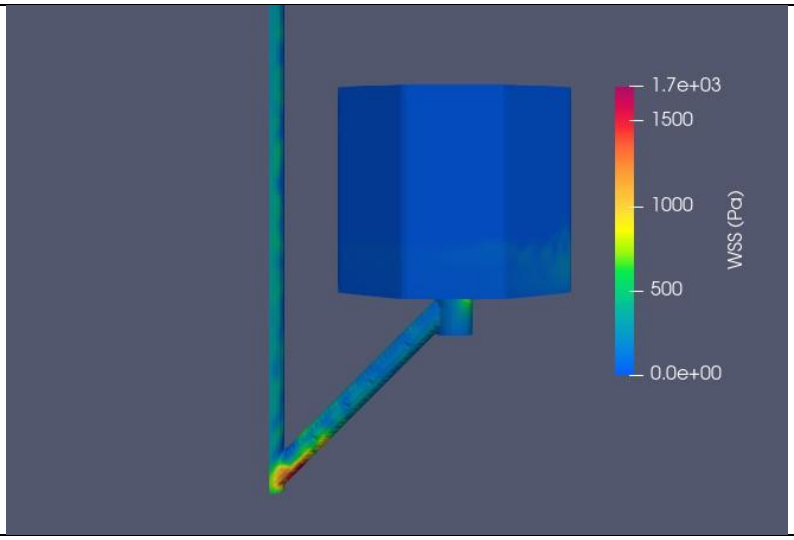

Figure 27: Contour map of wall shear stress 45º runner

Figures 25–27 present the evolution of maximum wall shear stress (WSS) against accumulated filling volume, alongside spatial WSS contour maps for the 55° and 45° runner designs. The 90° baseline maintains a consistently low and stable profile, with maximum shear stress remaining below 50 Pa throughout filling, indicating minimal boundary friction. In contrast, the 55° configuration exhibits a sharp increase in shear stress, reaching a maximum of 1763.11 Pa at V = 0.0276 m^3. The corresponding contour map reveals a concentrated high-stress zone at the runner-to-wall intersection, confirming direct impingement of the incoming jet onto the vertical mould surface.

For the 45° runner, the shear stress response is considerably more moderate and stable, fluctuating between 416 Pa and 741.35 Pa. The spatial contours show that the boundary shear is distributed more evenly across the mould floor rather than focused onto the vertical wall. This non-monotonic behaviour highlights the geometric shift in the flow field: transitioning from symmetric radial deflection at 90°, to direct wall impingement at 55°, and finally to near-tangential flow along the base at 45°.

While the 1763.11 Pa peak in the 55° case exceeds the 1000–1200 Pa range commonly cited in literature for silica–alumina refractory wear, these numerical values should be viewed primarily as relative indicators of boundary friction rather than exact predictions of mechanical failure. Nevertheless, this comparison clearly identifies the 55° angle as a high-risk configuration for refractory erosion and sand-wash inclusion pickup. The 45° design provides a much better balance, substantially lowering localized wall stress while still maintaining the desired directional circulation across the mould base.

4.4.3 Circulation Optimization (The 45° Case)

The strongest argument for adopting the 45° runner configuration lies in the significant reduction of volumetric dead zones [18]. While the 90° baseline leaves 47.76% of the melt volume stagnant, the 45° runner directs the incoming jet along the mould floor at a shallow exit angle ($\theta = 35.45°$) [8], creating a continuous horizontal sweeping action across the base of the octagonal cavity [18].

This bottom-sweeping motion sets up a large toroidal recirculation loop across the lower core and corners of the mould [30]. By keeping the metal actively circulating, the final dead-zone fraction drops to 28.60%. A 40.1% relative reduction in stagnant volume compared to the perpendicular baseline. Metallurgically, this improved circulation promotes better thermal and chemical mixing, which helps reduce temperature stratification along the cold mould walls and lowers the risk of macro-segregation during early solidification [28, 51].

Importantly, choosing the 45° runner represents an intentional engineering trade-off rather than a setup that outperforms the baseline on every single metric. It accepts a moderate increase in initial surface splashing (M4 of 354.69 mm compared to 294.96 mm for the 90° baseline) in exchange for a substantial improvement in internal circulation, while keeping wall shear stress at a manageable level for refractory wear. This practical balance between surface calm, lining integrity, and bulk mixing forms the core basis for the final gating recommendations presented in Chapter 5.

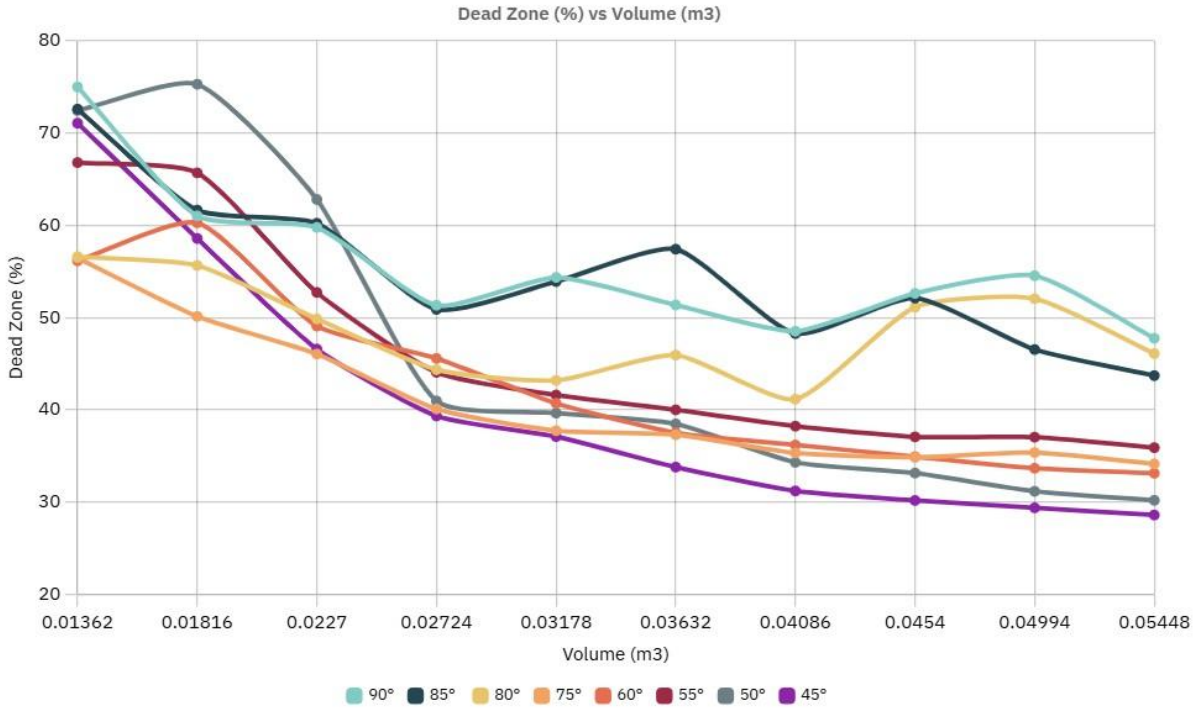

Figure 28: Dead Zone vs Volume (For different angled runners)

Figure 28 shows curves showing the percentage of developed liquid steel volume ($\alpha_{metal} \geq 0.9$) moving at stagnant velocities ($U < 0.05$ m/s) over the filling sequence. All geometries start with high dead zone percentages (56%-75%) at $V = 0.01362m^3$ and decay monotonically as volume accumulates. The 90° baseline trendline plateaus early and remains elevated, ending at a high 47.76% stagnant volume. In contrast, the 45° runner exhibits a steep, continuous downward slope, reaching an absolute global minimum of 28.60%. The initial peak reflects localized momentum confinement within the narrow entering jet before shear layers can entrain surrounding fluid. As filling progresses, the 45° design activates a large-scale toroidal recirculation cell that sweeps the stagnant corners of the octagonal mould, achieving a 40.1% relative improvement in bulk mass circulation over the 90° control.

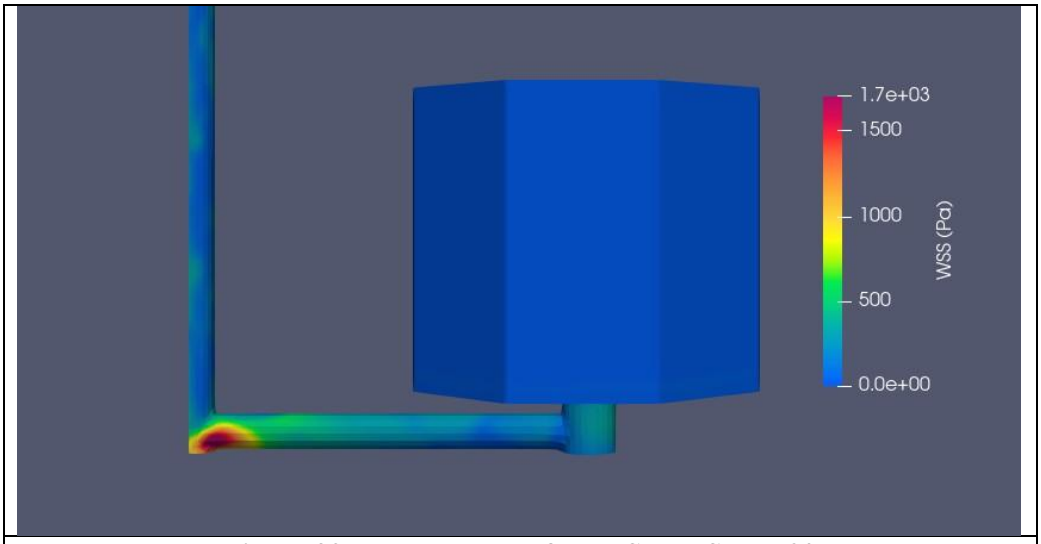

Figure 29: contour map of Wall Shear Stress 90

Figure 29 shows 3D spatial contour mapping the distribution of localized Wall Shear Stress across the runner, ingate well, and lower mould boundaries for the 90° perpendicular geometry. The contour field is dominated by deep blue regions across the mould cavity walls, confirming that peak localized shear stresses remain below 49.05 Pa throughout the filling process.

4.5 Comparative Study: Influence of Inlet Velocity (90° Runner)

To map the operational boundaries of the bottom-pouring process, a velocity sensitivity analysis was performed on the standard 90° perpendicular geometry as a controlled baseline. The inlet velocity magnitude (U) was varied across six discrete values: 1.5, 2.0, 2.47 (baseline), 3.0, 3.5, and 4.0 m/s.

Table 13: Mass flow rate for different velocities

Inlet Velocity (U) [m/s]	**Mass Flow Rate ($\dot{m}$) [kg/s]**
1.5	66.8
2	89.07
2.47	110
3	133.6
3.5	155.87
4	178.14

Table 14: Master Comparison of Peak Filling Metrics for Variable Velocities

Inlet Velocity (m/s)	Peak M4 (mm)	Peak Wall Shear Stress (Pa)	Final Dead Zone (%)	Max Exit Angle (°)
1.5 +	285.67 *(↓ 9.29 mm)* +++	33.89 *(↓ 15.16 Pa)* +++	60.92% *(↑ 13.16%)* +	90°
2 +	335.65 *(↑ 40.69 mm)* +++	466.61 *(↑ 417.56 Pa)* ++	56.40% *(↑ 8.64%)* +	90°
2.47 (Baseline) ++	**294.96** *(Baseline Reference)* +++	**49.05** *(Baseline Reference)* +++	**47.76%** *(Baseline Reference)* +	47.87°
3 +++	375.32 *(↑ 80.36 mm)* ++	62.86 *(↑ 13.81 Pa)* +++	41.50% *(↓ 6.26%)* ++	90°
3.5 +	394.89 *(↑ 99.93 mm)* ++	745.81 *(↑ 696.76 Pa)* +	*41.30% (↓ 6.46%)*	75.85°
4 +	553.89 *(↑ 258.93 mm)* +	933.79 *(↑ 884.74 Pa)* +	38.17% *(↓ 9.59%)* ++	71.56°

(+++): Recommended Window (3.0 m/s): Represents the highest productivity velocity for standard 90° systems where localized Wall Shear Stress remains safely buffered beneath critical refractory erosion boundaries (Wall shear stress = 62.86 Pa, safely below the ~1000 Pa erosion threshold)

(++): Acceptable / Baseline Window (2.0 to 2.47 m/s): Operable and non-damaging to mould linings, but hydrodynamically sub-optimal due to large dead zone fractions (47.76%-56.40%).

(+): (1.5 m/s and > 3.5 m/s): Velocities are rejected due to excessive thermal stagnation and cold shut vulnerabilities, while velocities greater than 3.5 m/s are prohibited due to boundary layer collapse, severe wave-folding air entrainment, and high refractory erosion.

4.5.1 Linear Throughput vs. Cubic Kinetic Energy Flux Scaling

In bottom-pouring systems, the mass flow rate (m*) exiting the ingate scales linearly with changes to the inlet velocity magnitude (U) [66]:

$$m^* = rho * A_{in} * U \quad (4.1)$$

However, the kinetic energy flux (E_k) injected into the mould cavity scales cubically as a function of velocity [67]:

$$E_k = ½\ m^* U^2 \quad (4.2)$$
$$E_k = 1/2 * rho * A_{in} * U^3 \quad (4.3)$$

This cubic scaling means that increasing velocity to raise production rate introduces disproportionately large amounts of kinetic energy and turbulence, which the system cannot easily dissipate substantially altering free-surface stability [26, 40].

At the lowest evaluated velocity, 1.5 m/s, the incoming mass throughput is limited to 66.81 kg/s, injecting a modest kinetic energy flux of just 75.16 W into the cavity. While this low-momentum regime maintains an unusually quiet free surface (M4 = 285.67 mm) and negligible wall shear stress (33.89 Pa), it produces an unacceptably high dead-zone fraction exceeding 60%. This level of stagnation causes rapid thermal decay of the melt, making the condition non-viable for commercial operation due to the resulting cold-shut risk [16, 51].

As velocity increases through 2.0 m/s and the nominal baseline (2.47 m/s), the system operates within a stable hydrodynamic window. Once inlet velocity reaches the 3.0 m/s transitional threshold, however, the cubic scaling law begins to drive system instability [30]. At 3.0 m/s, the kinetic energy flux climbs to 601.20 W, and the vertical momentum of the perpendicular jet drives the initial transient splash (M4) up to 375.32 mm [9].

Table 15: Mass Flow rate and Kinetic Energy Flux at different velocities

Inlet Velocity U (m/s)	**1.5**	**2**	**2.47**	**3**	**3.5**	**4**
Mass Flow Rate (kg/s)	66.80	89.07	110.00	133.60	155.87	178.14
Kinetic Energy Flux (W)	75.16	178.14	335.55	601.20	954.70	1425.12

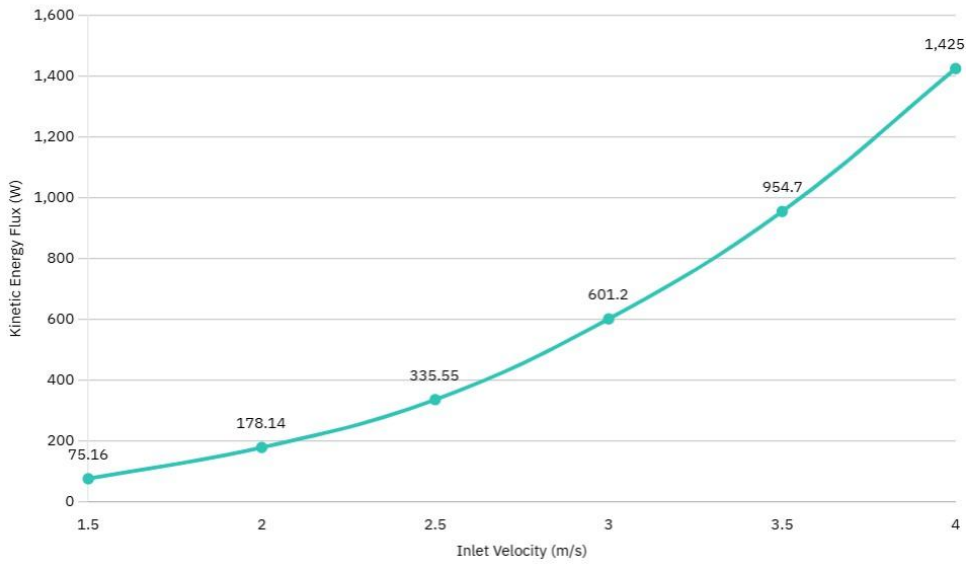

Figure 30: Inlet Velocity vs Kinetic Energy Flux

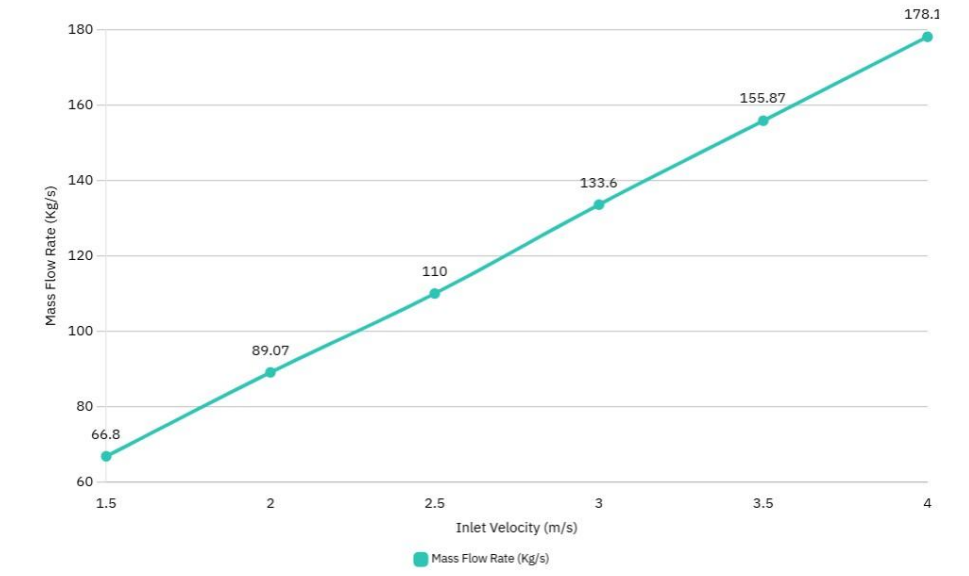

Figure 31: Inlet Velocity vs Mass Flow Rate

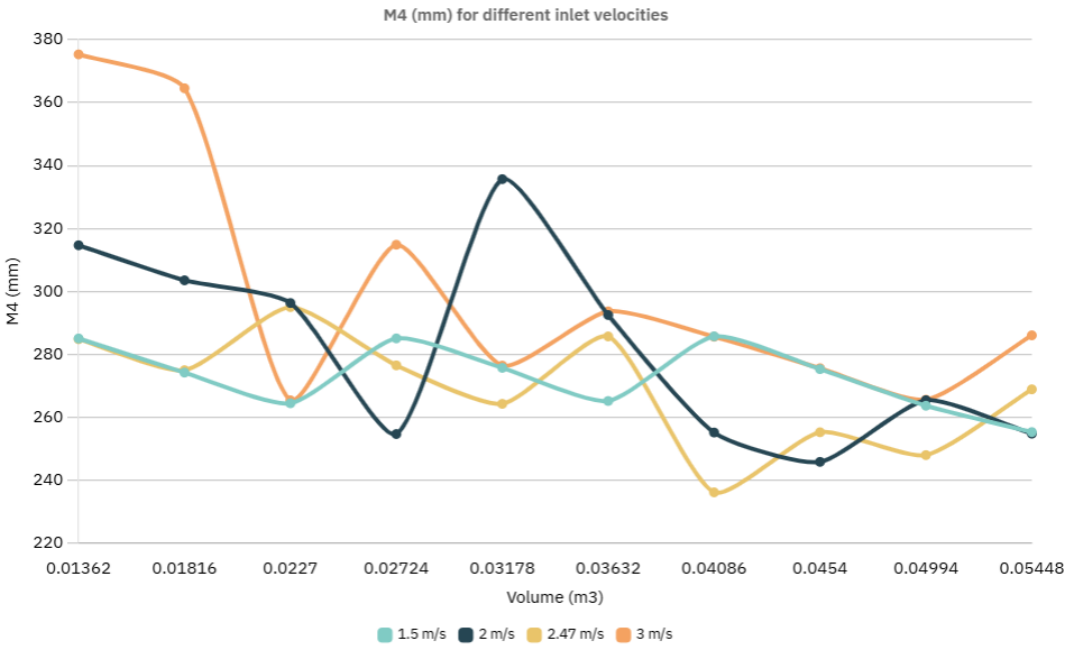

Figure 32: M4 vs Volume for different inlet velocities

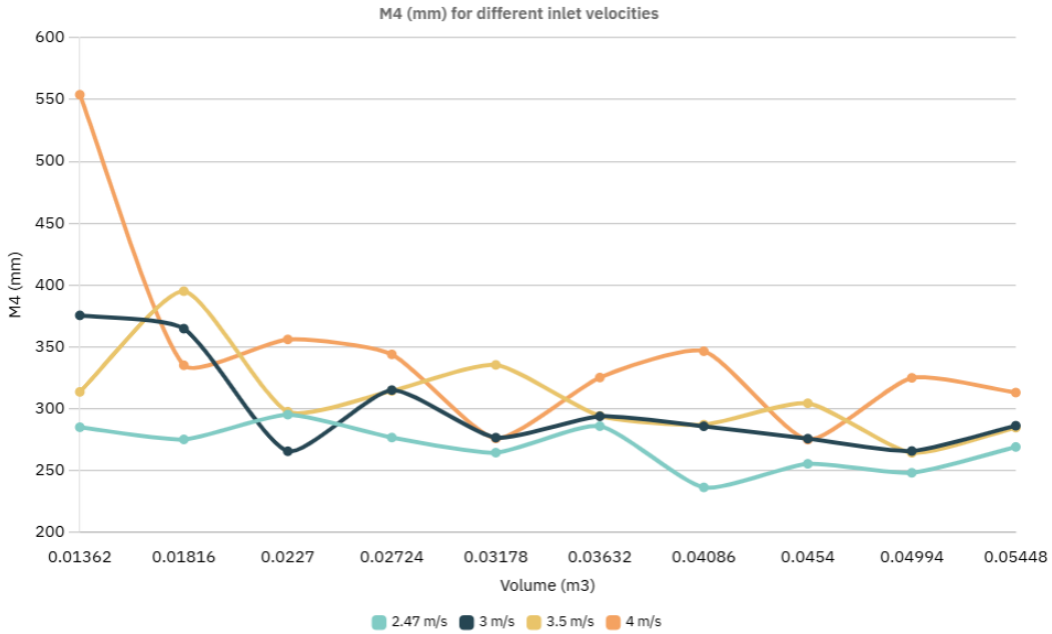

Figure 33: M4 vs Volume for different inlet velocities

Figure 32 and 33 show Line plots comparing M4 transient overshoot across six inlet velocities: 1.5, 2.0, 2.47, 3.0, 3.5, and 4.0 m/s. At sub-critical velocities (2.47 m/s), the M4 trendlines remain tightly grouped between 236mm and 335mm. At 3.0 m/s, the initial splash level shifts upward to 375.32 mm. At 4.0 m/s, the trendline starts with an extreme vertical spike reaching 553.89 mm before decaying toward 300 mm. While throughput scales linearly ($m^* \propto U$), kinetic energy flux scales cubically ($E_k \propto U^3$). At 4.0 m/s, the energy influx reaches 1425.12

W, overwhelming gravity and driving violent surface eruptions that trap deep atmospheric air pockets (Air % = 2.85%).

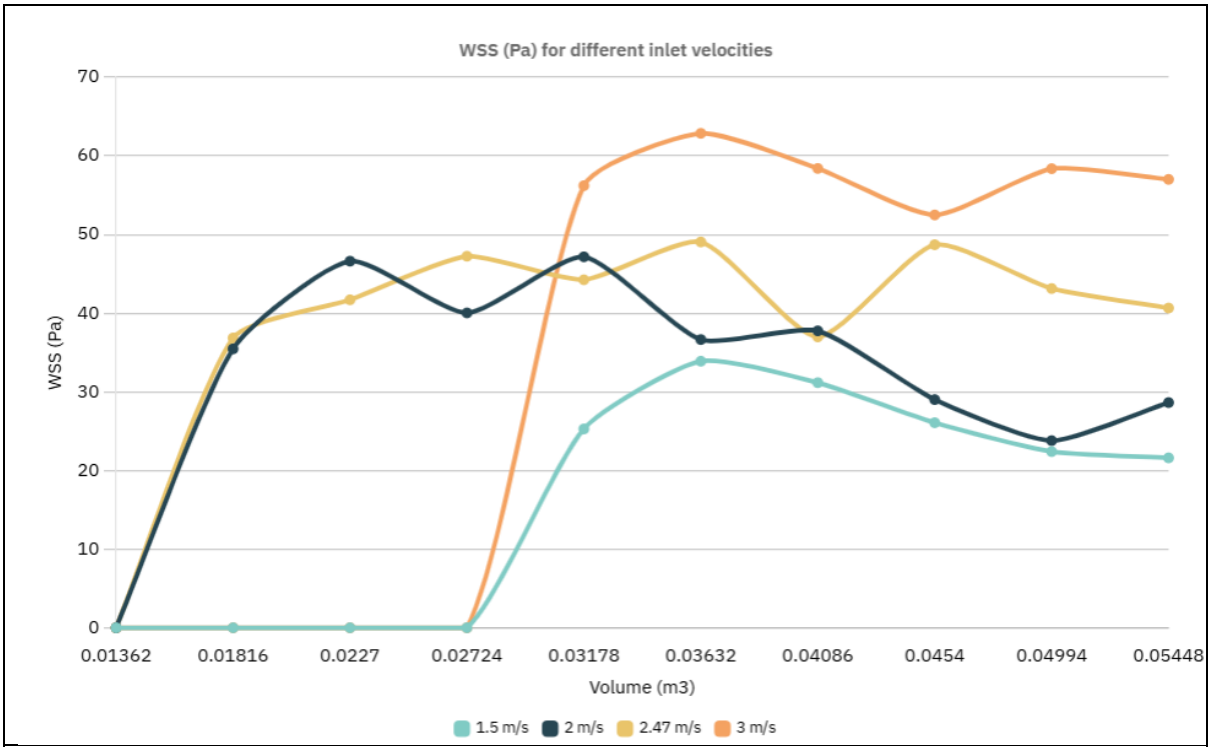

Figure 34: Wall Shear Stress vs Volume for different inlet velocities

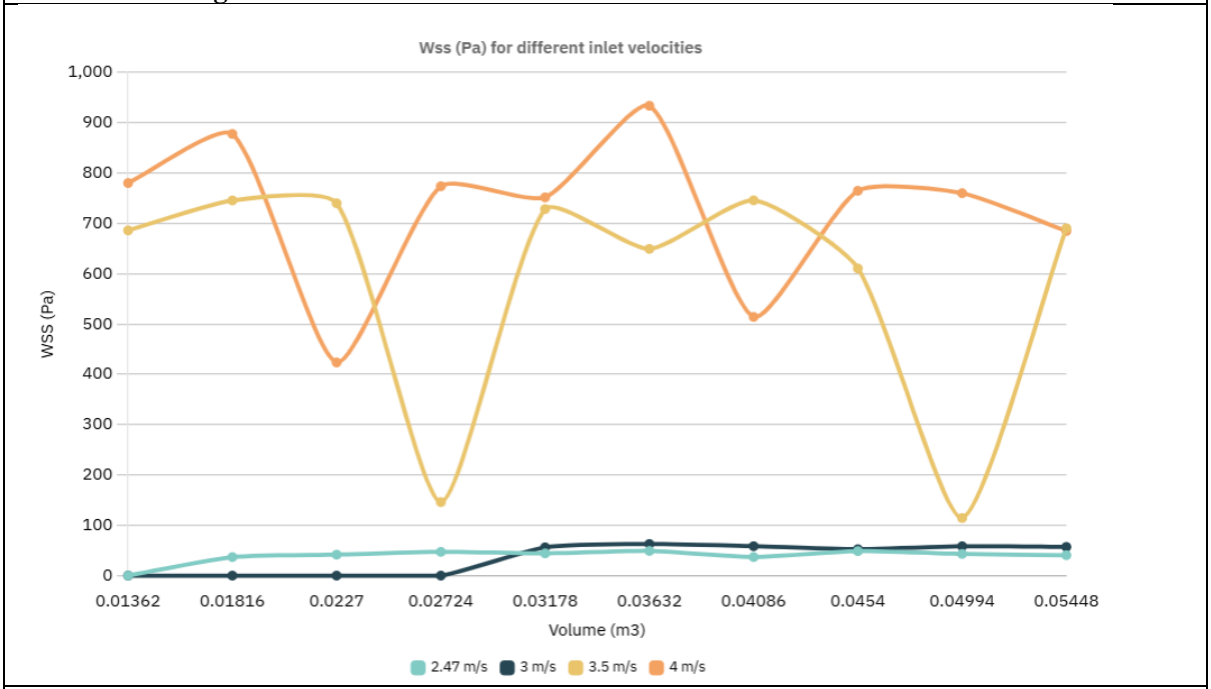

Figure 35: Wall Shear Stress vs Volume for different inlet velocities

Figure 34 and 35 show transient tracking of maximum boundary layer Wall Shear Stress for velocities between 1.5 m/s and 4.0 m/s. From 1.5 m/s to 3.0 m/s, the trendlines are flat and low, with peak stresses remaining strictly below 63 Pa. Between 3.0 m/s and 3.5 m/s, the

curve jumps by a factor of 12, surging to 745.81 Pa and peaking at 933.79 Pa for 4.0 m/s. This abrupt upward shift marks the breakdown of the near-wall hydrodynamic cushion. Beyond 3.0 m/s, surging kinetic energy forces the core jet through the slow-moving boundary buffer, causing direct fluid-wall friction that sets 3.0 m/s as the maximum safe operational velocity limit.

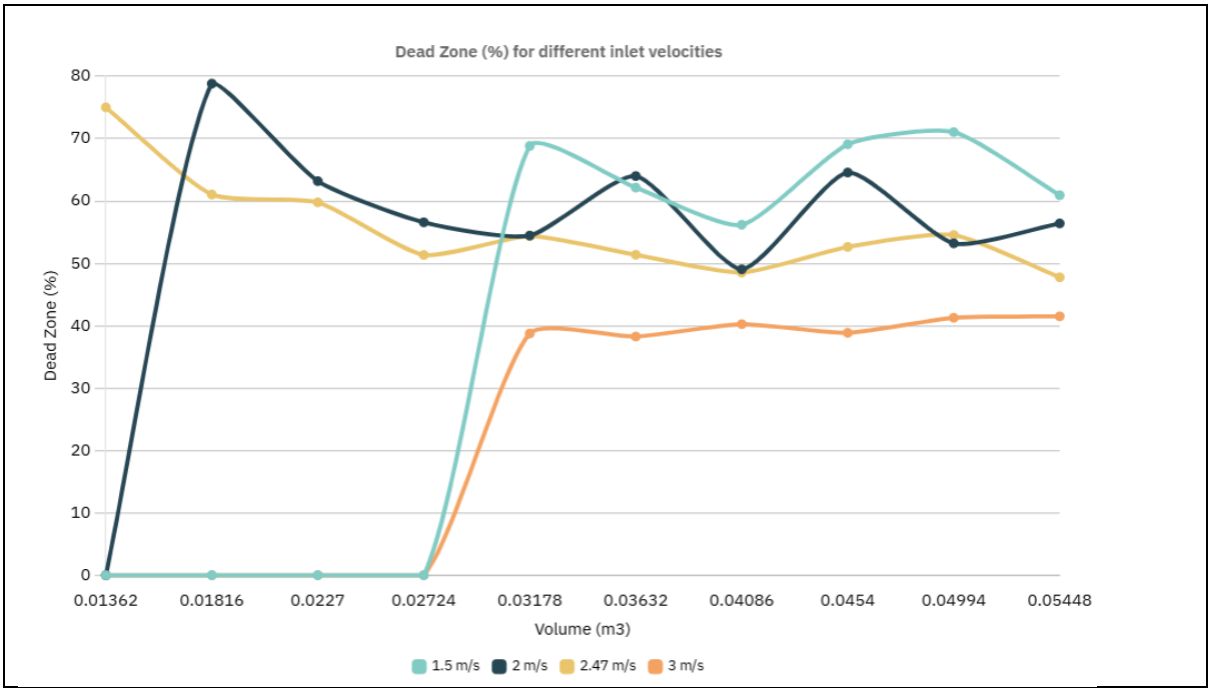

Figure 36: Dead Zone vs Volume for different inlet velocities

Figure 36 compares the volume of stagnant fluid over time across the different inlet velocities tested. At 1.5 m/s, the dead-zone fraction remains above 60% through nearly the entire filling cycle because the incoming jet lacks the momentum needed to reach and clear out the mould corners, creating a clear risk of cold shuts due to rapid conductive cooling. Increasing the inlet velocity shifts the curves downward, with the 3.0, 3.5, and 4.0 m/s cases stabilizing within a narrow range between 38.17% and 41.50%. While higher speeds improve bottom circulation, the marginal reduction in stagnant volume above 3.0 m/s shows clear diminishing returns that do not justify the sharp increases in surface splashing and refractory wall shear stress observed at 3.5 and 4.0 m/s.

4.5.2 Boundary Layer past 3.0 m/s

Beyond the 3.0 m/s threshold, at 3.5 and 4.0 m/s, the system undergoes a marked hydrodynamic transition [64]. Increasing velocity from 3.0 to 3.5 m/s produces only a modest, predictable linear rise in mass throughput (133.60 to 155.87 kg/s), yet triggers a sudden, roughly twelve-fold increase in localised Wall Shear Stress from 62.86 Pa to 745.81 Pa.

This abrupt jump indicates a fundamental change in boundary layer structure [66]. Below 3.0 m/s, the symmetrical fluid upwelling forms a stable, low-velocity recirculation buffer along the vertical walls that shields the refractory faces from the jet's high-velocity core [13]. Once velocity crosses the 3.0 m/s threshold, the increased kinetic energy flux collapses this protective buffer [30]: the core of the vertical jet breaks through the boundary layer and interacts directly with the solid mould walls, producing the sharp rise in localised friction [58].

At the maximum tested velocity of 4.0 m/s, the kinetic energy flux reaches 1425.12 W nearly nineteen times the flux at 1.5 m/s and drives the peak transient vertical splash (M4) to 553.89 mm. This surge overtops the mould's initial boundary-layer safety margin and triggers substantial entrained air pocket formation [60]; deep air entrapment metrics show the trapped atmospheric gas fraction spiking to 2.85%.

This level of entrainment promotes rapid re-oxidation at the exposed liquid steel interface, producing a high concentration of macroscopic oxide-film defects that compromise the structural integrity of the final ingot [10, 51]. On this basis, the velocity sensitivity matrix establishes a practical upper operational boundary of 3.0 m/s for 90° perpendicular runner layouts, to prevent severe mould wear and air entrainment defects [12].

Chapter 5: Concluding discussions

This chapter summarizes the main findings from the numerical simulations, reviews how each research objective was addressed, and discusses the overall fluid flow behaviour in uphill ingot casting. Transient, multiphase CFD simulations were performed in OpenFOAM using the Volume of Fluid (VOF) method and the standard k– ε turbulence model to examine how varying the runner angle and inlet velocity affects initial mould filling. The analysis tracks key parameters including free-surface stability (evaluated through metrics M1, M2, and M4), wall shear stress, dead-zone volume fraction, and deep air entrapment. In addition to presenting the raw simulation data, these results are compared with previous CFD casting literature and linked back to the industrial casting problems outlined in Chapter 1 to provide practical gating design recommendations, especially where the observed flow behaviour diverged from traditional foundry practices.

5.1 Hydrodynamic Behaviour and Operational Trade-Offs

The parametric results show several non-intuitive trends that challenge common assumptions in gating design. Conventional practice generally assumes that changing the runner angle produces a steady, predictable change in flow quality that can be mapped using only a few test points. However, the simulation data showed a strongly non-monotonic response. As the runner angle decreases from the 90° perpendicular baseline, peak splashing intensity (M4) and peak wall shear stress initially rise, which fits the expected behaviour of an increasingly directional, angled jet. Rather than continuing smoothly, this trend peaks sharply at 55°. At this specific angle, the ingate geometry directs the core of the jet straight into the adjacent vertical mould wall rather than letting it strike the floor and lose momentum. This direct impingement drives M4 up to 425.77 mm and peak wall shear stress to 1763.11 Pa, which exceeds the mechanical yield limit for standard silica–alumina refractory bricks and creates a localized erosion risk. Because angles both above and below 55° perform significantly better, a designer testing only

a few widely spaced angles would miss this hazard completely, demonstrating that runner angle variations cannot simply be interpolated across broad intervals.

By comparison, the 45° runner gave the best overall performance among all eight geometries tested. Relative to the 90° baseline, it reduced final stagnant dead-zone volume by 40.1% (falling from 47.76% down to 28.60%) by establishing a stable toroidal recirculation loop across the mould floor. Free-surface waves also settled down faster, with the M1 and M2 trendlines reaching a steady state earlier in the filling sequence than in the baseline or intermediate angle setups. At the same time, peak wall shear stress remained at 741.35 Pa, safely below both the 55° peak and the 1000–1200 Pa refractory threshold. Although the 45° configuration generated a higher peak volumetric hump than the baseline (354.69 mm compared to 294.96 mm), it provided the most practical balance between bottom circulation, surface wave damping, and refractory protection.

The velocity tests on the 90° baseline showed that while the system handles low to moderate inlet velocities well, flow stability drops off sharply above roughly 3.0 m/s. This response is tied directly to the governing physics: while mass throughput increases linearly with inlet velocity, kinetic energy flux scales with the cube of the velocity (v^3). Increasing pouring velocity to raise throughput therefore introduces disproportionate instability into the mould. For instance, increasing the velocity from 3.0 to 3.5 m/s increased mass flow rate by only about 16.7% (from 133.60 to 155.87 kg/s), but caused an approximately twelve-fold spike in peak wall shear stress, jumping from 62.86 Pa to 745.81 Pa. This jump occurs because the protective low-velocity recirculation buffer near the refractory wall breaks down, allowing the high-velocity jet core to strike the wall directly. At 4.0 m/s, the flow becomes severely unstable, with deep air entrapment rising to 2.85% and M4 reaching 553.89 mm. Consequently, 3.0 m/s represents a clear physical upper operating threshold for 90° perpendicular systems.

Across all test cases, an inherent trade-off exists between encouraging bulk circulation to eliminate dead zones and limiting localized wall shear stress to prevent refractory erosion. Angling the runner to drive fluid across the mould floor breaks up stagnant regions, but delivering more momentum along solid surfaces inevitably raises wall shear stress somewhere in the mould. Because no single geometry simultaneously minimized every metric, selecting an operating setup requires balancing the risk of stagnation-related inclusion defects against refractory maintenance costs. The 45° runner was selected because it substantially reduces stagnant zones while keeping refractory wear well within safe limits, though facilities with

different refractory materials or cleanliness standards can use the dataset in Chapter 4 to adjust this trade-off accordingly.

5.2 Practical Design Guidelines for Bottom-Pouring Systems

These findings translate into several direct design guidelines for large octagonal bottom-poured ingots. Where tooling and layout allow, foundries should adopt a 45° runner angle, as it redirects incoming momentum horizontally across the floor to form a steady recirculation pattern that improves filling uniformity without damaging the lining. Conversely, runner angles between approximately 55° and 75° should be avoided in new moulds due to the direct jet impingement that occurs in this range; existing tooling operating within this band should be prioritized for modification because refractory erosion accumulates over time. If a foundry must keep a 90° perpendicular setup due to existing tooling investments, the inlet velocity should be capped at 3.0 m/s. Operating above this speed requires either upgrading to higher-grade refractory bricks or adding flow-conditioning devices like ceramic foam filters or swirl blades to dissipate jet momentum.

During casting operations, process monitoring should focus heavily on the first 30–60 mm of mould rise. The simulation data showed that this initial window produces the greatest free-surface volatility and the highest peaks for M1, M2, and M4 before the rising liquid metal dampens the incoming jet. Comparing configurations on a volume-normalized basis evaluating flow parameters against injected volume or equivalent fill height rather than run time proved essential for making fair comparisons across cases with differing flow rates and should be adopted in future comparative studies. Table 16 compiles these guidelines into a single reference format for direct use in gating design.

Table 16: Recommended Design and Operational Guidelines

Design/Operating Parameter	Recommended Value	High-Risk Zone to Avoid
Runner Angle	45°	55°–75°
Inlet Velocity (90° runner)	≤ 3.0 m/s (tested baseline: 2.47 m/s)	> 3.5 m/s
Expected Final Dead Zone	< 30%	> 45%
Peak Wall Shear Stress	< 800 Pa	> 1,500 Pa
Maximum Volumetric Hump (M4)	< 360 mm (45° design: 354.69 mm)	> 400 mm

Chapter 6. Conclusions

Evaluation of the M1, M2, and M4 hump metrics identified a dangerous, non-monotonic splashing peak at a 55° runner inclination, disproving conventional assumptions in casting literature that meniscus calm improves monotonically with runner angle.

45° angled runner was established as the optimal delivery geometry, providing superior free-surface damping, suppressing geyser hump height, and preventing violent wave collapse without necessitating structural modifications to existing mould tooling.

Meniscus violence was directly coupled to deep gas entrapment; severe wave breaking and high inlet velocities (3.5–4.0 m/s) drove deep air fractions up to 2.85%, whereas the calmer interfacial rise of the 45° runner effectively suppressed this entrainment pathway.

Wall shear stress mapping established explicit operational thresholds to prevent refractory erosion, identifying severe degradation hazards caused by direct jet impingement within the 55°–75° angle window and defining an upper velocity limit of 3.0 m/s in conventional 90° systems to prevent fluid buffer-layer collapse.

Implementing the 45° runner achieved a 40.1% relative reduction in stagnant volume fraction (< 0.05 m/s) relative to the 90° baseline, significantly enhancing convective core circulation and thermal homogeneity within the octagonal mould corners.

Demonstrating a cubic kinetic-energy scaling relationship with inlet velocity provides foundries with a grounded rule of thumb for evaluating throughput increases, while the discovery of the localized 55° peak proves that gating design requires dense parametric CFD sweeps rather than isolated single-point validations.

Findings are bounded by the planar half-symmetry assumption, the Standard k– ε turbulence closure, and independently decoupled sweeps (fixed velocity for angle; variable velocity on 90° only), identifying combined angle–velocity sweeps and non-symmetric pouring alignment as primary directions for future work.

Chapter 7: Sustainability and Future Work

The transition of material processing from controlled laboratory environments to large-scale industrial production necessitates a comprehensive evaluation beyond purely technical and economic performance. As engineering practices evolve to meet modern global challenges, the viability of any industrial process is intrinsically linked to its environmental footprint and ethical footprint. This chapter examines the broader ecosystem of the manufacturing process, analysing the lifecycle sustainability of the materials used, the ethical responsibilities inherent in industrial-scale engineering, and the long-term socioeconomic impacts on the global supply chain.

7.1 Sustainability and Environmental Impact

From an environmental standpoint, reducing casting defects has a direct sustainability benefit, as scrapped ingots must be remelted in an Electric Arc Furnace (EAF), consuming significant amounts of electrical energy and generating extra emissions. The standard 90° baseline setup exhibits poor bottom circulation, resulting in a dead-zone volume fraction of 47.76%, which increases the likelihood of cold shuts and rejected heats. Switching to a 45° runner reduces this stagnant volume to 28.60% (a 40.1% relative improvement), which promotes better thermal mixing across the mould. However, this gain in fluid circulation must be weighed against refractory wear. While the 90° design produces a very low peak wall shear stress of 49.05 Pa, the 55° configuration creates a severe spike of 1763.11 Pa that would likely erode the refractory lining and introduce ceramic inclusions into the melt. Mapping this non-monotonic behaviour demonstrates that adopting a 45° runner provides the most practical compromise: it enhances fluid circulation to cut scrap-related remelting, while staying safely below the severe wear region observed around 55°. Accurate, unbiased reporting of these trends is also essential from an engineering standpoint, ensuring that mould design is guided by complete data rather than linear assumptions that would completely miss the 55°–75° violence peak. In terms of operational safety, bottom-pouring operations involve high thermal risks related to liquid steel containment, mould overtopping, and flashing. The velocity sensitivity analysis on the 90° baseline establishes a clear safety boundary: increasing inlet velocity from the 2.47 m/s baseline to 4.0 m/s produces a linear increase in mass flow rate, but the cubic scaling of kinetic energy flux causes vertical splashing (M4) to jump from 294.96 mm to 553.89 mm, alongside an approximately twelve-fold spike in peak wall shear stress. Keeping the inlet velocity at or

below 3.0 m/s serves as a practical operational limit to avoid structural breakouts and splash hazards on the casting floor. While many high-alloy foundries continue to use 90° right-angle runners because standard refractory bricks are simpler and cheaper to manufacture and assemble, these simulation results provide the quantitative data needed to justify upgrading to angled geometries. In addition, these velocity and momentum limits can be incorporated into automated pouring logic, allowing slide-gates to throttle dynamically as the ferrostatic head in the ladle drops, keeping the flow within a stable operating window throughout the pour.

7.2 Future Work

Several areas could be explored in future work to build on the findings of this thesis. First, because the current VOF simulations are purely isothermal, coupling the flow model with heat transfer and solidification kinetics would be an important next step. This would help show whether the active bottom circulation from the 45° runner actually prevents premature freezing and uneven shell growth compared to the stagnant dead zones found in the 90° baseline. Second, experimental validation using a scaled water model equipped with Particle Image Velocimetry (PIV) would be very useful. PIV data and high-speed photography would provide direct physical measurements to verify the predicted jet angles, free-surface hump heights, and splash behaviour. Third, the inlet boundary condition could be made more realistic by accounting for the falling ferrostatic head in the ladle and slide-gate throttling over time, rather than assuming a constant inlet velocity throughout the pour. Finally, testing this runner design on moulds with more complex profiles such as corrugated or fluted ingot walls or in multi-ingate gating systems would show how well the redirected flow behaves in full-scale production geometries.

Chapter 8: Utilisation of AI Tools

Generative artificial intelligence (AI) tools were used as supplementary aids during the preparation of this thesis. Their use was mainly related to Python scripting, data post-processing, visualisation, and language editing. AI tools assisted in drafting and debugging scripts using libraries such as pandas, NumPy, and Matplotlib. These scripts were used to process data exported from ParaView, analyse selected regions of the mould, and calculate transient flow metrics, including free-surface parameters (M1, M2, and M4), dead zone fractions, and wall shear stress.

AI tools were also used to assist with the presentation of engineering results, including the formatting of plots, composite figures, and decision matrices. In addition, they were used for language editing and paraphrasing to improve clarity, correct grammatical errors, and reduce repetition in parts of the report.

The numerical simulations, interpretation of results, engineering analysis, and conclusions presented in this thesis remain the author's responsibility. AI-generated suggestions and code were used as supporting tools, and the resulting material was reviewed and adapted for the purposes of this study.

References

[1] World Steel Association, *World Steel in Figures 2025*, Brussels: worldsteel, 2025.

[2] EUROFER, *European Steel in Figures 2024: Statistical Handbook*, Brussels: European Steel Association, 2024.

[3] Jernkontoret, *Facts and figures: The Swedish steel industry*, Stockholm: Jernkontoret, 2024.

[4] Statbase, "Steel production in Sweden - yearly data and table," 2025.

[5] GMK Center, "Global steel production fell by 0.9% y/y in 2024," GMK Center Metallurgical Market Analysis, Jan.2026.

Available: https://gmk.center/en/news/global-steel-production-fell-by-0-9-y-y-in-2024/

[6] J. Yin, "A study of Mould flux entrapment and gas entrainment in an ingot casting process," Doctoral thesis, KTH Royal Institute of Technology, Stockholm, Sweden, 2021.

[7] A. Pola, M. Gelfi, and G. M. La Vecchia, "Comprehensive Numerical Simulation of Filling and Solidification of Steel Ingots," *Materials*, vol. 9, no. 9, 2016, Art. no. 726.

[8] J. Yin, L. Ragnarsson, M. Ersson, and P. G. Jönsson, "Numerical Study on the Influence of the Filling Angle on the Fluid Flow," *Steel Research International*, vol. 92, no. 8, Aug. 2021, Art. no. 2000554.

[9] J. Yin, L. Ragnarsson, M. Ersson, and P. G. Jönsson, "An Experimental and Numerical Study of the Free Surface in an Uphill Teeming Ingot Casting Process," *Steel Research International*, vol. 91, no. 10, Oct. 2020, Art. no. 2000100.

[10] L. Zhang and B. G. Thomas, "State of the Art in the Control of Inclusions during Steel Ingot Casting," *Metallurgical and Materials Transactions B*, vol. 37, no. 5, pp. 733–754, Oct. 2006.

[11] L. Ragnarsson, R. Eriksson, and P. G. Jönsson, "Flow pattern in ingot during mould filling and its impact on inclusion removal," *Ironmaking & Steelmaking*, vol. 37, no. 5, pp. 360–367, 2010.

[12] A. Kermanpur, S. Mahmoudi, and S. Hajipour, "Mathematical Modelling of the Initial Mould Filling in Bottom-Poured Steel Ingots," *ISIJ International*, vol. 48, no. 12, pp. 1711–1718, 2008.

[13] R. Eriksson and P. G. Jönsson, "Flow pattern in ingot during mould filling and its influence on inclusion distribution," *Ironmaking & Steelmaking*, vol. 29, no. 5, pp. 359–366, 2002.

[14] B. Zhang, M. Ersson, P. G. Jönsson, and M. Suzuki, "Teeming stream protection using an argon shroud during casting of steel ingots," *International Journal of Minerals, Metallurgy, and Materials*, vol. 24, no. 12, pp. 1386–1396, 2017.

[15] L. Hallgren, L. Ragnarsson, R. Eriksson, and P. G. Jönsson, "A first attempt to implement a Swirl blade in production of ingots," *ISIJ International*, vol. 50, no. 12, pp. 1763–1769, 2010.

[16] I. Hahn, C. Sturz, J. Lifka, and E. Flender, "Quality Prediction of Cast Ingots," in *Proceedings of the 1st International Conference on Ingot Casting Rolling and Forging (ICRF 2012)*, Aachen: MagmaSoft, 2012.

[17] Transvalor, *Improving the Ingot Quality by Understanding the Behavior of the Mould Flux*, 2024.

[18] J. Yin, L. Ragnarsson, M. Ersson, and P. G. Jönsson, "Mathematical Modelling of the Initial Mould Filling with Utilization of an Angled Runner," *Metals*, vol. 9, no. 6, 2019, Art. no. 696.

[19] Persistence Market Research, *Steel Ingots Market Size, Share & Growth Trends, 2033*, 2026.

[20] C. Chen and Y. Sun, "Numerical simulation of melt flow and heat transfer in casting filling process based on SPH," *Computers & Fluids*, vol. 280, 2024, Art. no. 106325.

[21] L. Hallgren, L. Ragnarsson, R. Eriksson, and P. G. Jönsson, "A first attempt to implement a Swirl blade in production of ingots," *ISIJ International*, vol. 50, no. 12, pp. 1763–1769, 2010.

[22] Vesuvius / Foseco, *Ingot Casting Solutions and Filters Product Data*, 2024.

[23] M. Bruna, J. Suchy, and M. Kuriš, "Casting Quality Improvement by Gating System Optimization," *Archives of Foundry Engineering*, vol. 21, no. 1, pp. 49–54, 2021.

[24] Magmasoft, *Ingot Casting Optimization with MAGMA 6.1. Technical Documentation*, 2026.

[25] ProCAST, *Advanced Ingot Casting Simulation and Design*, ESI Group, 2025.

[26] H. K. Versteeg and W. Malalasekera, *An Introduction to Computational Fluid Dynamics: The Finite Volume Method*, 2nd ed. London: Pearson Education, 2007.

[27] H. Jasak, "Error Analysis and Estimation for the Finite Volume Method with Applications to Fluid Flow," Ph.D. dissertation, Imperial College London, London, UK, 1996.

[28] J. Szekely, *Fluid Flow Phenomena in Metals Processing*, New York: Academic Press, 1979.

[29] D. C. Wilcox, *Turbulence Modeling for CFD*, 2nd ed. La Cañada: DCW Industries, 1998.

[30] H. Morvan, A. E. Holdø, and G. S. Srai, "Numerical modelling of the filling of a steel ingot," *Applied Mathematical Modelling*, vol. 25, no. 10, pp. 817–840, 2001.

[31] Y. Sahai and T. Emi, *Tundish Technology for Clean Steel Production*, Warrendale, PA: Iron and Steel Society, 1996.

[32] B. G. Thomas, "Modeling of the Continuous Casting of Steel—Past, Present, and Future," *Metallurgical and Materials Transactions B*, vol. 33, no. 6, pp. 795–812, Dec. 2002.

[33] T. Holzmann, *Mathematics, Numerics, Derivations and OpenFOAM*, 4th ed. Loeben: Holzmann CFD, 2017.

[34] S. V. Patankar, *Numerical Heat Transfer and Fluid Flow*, Washington, DC: Hemisphere Publishing Corporation, 1980.

[35] S. Ergun, "Fluid flow through packed columns," *Chemical Engineering Progress*, vol. 48, pp. 89–94, 1952.

[36] B. E. Launder and D. B. Spalding, "The Numerical Computation of Turbulent Flows," *Computer Methods in Applied Mechanics and Engineering*, vol. 3, no. 2, pp. 269–289, 1974.

[37] S. B. Pope, *Turbulent Flows*, Cambridge: Cambridge University Press, 2000.

[38] B. G. Thomas, Q. Yuan, S. Sivaramakrishnan, S. P. Vanka, and M. B. Assar, "Comparison of Turbulence Models for Continuous Casting of Steel," in *Proceedings of the ISS Process Technology Conference*, Baltimore, MD, 2001, pp. 117–130.

[39] W. P. Jones and B. E. Launder, "The prediction of laminarisation with a two-equation model of turbulence," *International Journal of Heat and Mass Transfer*, vol. 15, no. 2, pp. 301–314, 1972.

[40] J. O. Hinze, *Turbulence*, 2nd ed. New York: McGraw-Hill, 1975.

[41] L. Zhang and B. G. Thomas, "State of the Art in Numerical Simulation of Continuous Casting," *Journal of Metallurgy*, vol. 2003, 2003.

[42] F. R. Menter, "Two-equation eddy-viscosity turbulence models for engineering applications," *AIAA Journal*, vol. 32, no. 8, pp. 1598–1605, 1994.

[43] C. W. Hirt and B. D. Nichols, "Volume of fluid (VOF) method for the dynamics of free boundaries," *Journal of Computational Physics*, vol. 39, no. 1, pp. 201–225, 1981.

[44] H. Rusche, "Computational Fluid Dynamics of Dispersed Two-Phase Flows at High Phase Fractions," Ph.D. dissertation, Imperial College London, London, UK, 2002.

[45] H. G. Weller, "A New Approach to VOF-based Interface Capturing Methods for High Resolution Advection," OpenFOAM Documentation, OpenCFD Ltd., 2008.

[46] E. Berberović, N. P. van Hinsberg, S. Jakirlić, I. V. Roisman, and C. Tropea, "Drop impact onto a liquid layer of finite thickness: Numerical and experimental study," *Physical Review E*, vol. 79, no. 3, 2009, Art. no. 036306.

[47] V. R. Gopala and B. van Wachem, "A volume of fluid method for evaporating boundary layers," *Chemical Engineering Science*, vol. 63, no. 11, pp. 2932–2946, 2008.

[48] J. U. Brackbill, D. B. Kothe, and C. Zemach, "A continuum method for modeling surface tension," *Journal of Computational Physics*, vol. 100, no. 2, pp. 335–354, 1992.

[49] R. Scardovelli and S. Zaleski, "Direct Numerical Simulation of Free-Surface and Interfacial Flow," *Annual Review of Fluid Mechanics*, vol. 31, no. 1, pp. 567–603, 1999.

[50] S. S. Deshpande, L. Anumolu, and M. F. Trujillo, "Evaluating the performance of the two-phase flow solver interFoam," *Computational Science & Discovery*, vol. 5, no. 1, 2012, Art. no. 014016.

[51] J. Campbell, *Castings*, 2nd ed. Oxford: Butterworth-Heinemann, 2003.

[52] K. C. Mills, *Recommended Values of Thermophysical Properties for Selected Commercial Alloys*, Cambridge: Woodhead Publishing, 1994.

[53] *Internal Simulation Case Setup: Gating System Geometry and Symmetry Plane Definitions*, Corporate/Internal Documentation, 2026.

[54] C. J. Greenshields, *OpenFOAM User Guide*, OpenFOAM Foundation, 2024.

[55] N. B. Vargaftik, *Tables on the Thermophysical Properties of Liquids and Gases*, 2nd ed. Washington, DC: Hemisphere Publishing Corporation, 1975.

[56] J. Campbell, *Complete Casting Handbook: Metal Casting Processes, Techniques and Design*, 2nd ed. Oxford: Butterworth-Heinemann, 2015.

[57] S. T. Hsu and M. R. Jolly, "A study of the fluid flow in the gating system of a casting," in *Proceedings of the 4th International Conference on Modeling of Casting, Welding and Advanced Solidification Processes*, 2000, pp. 87–94.

[58] X. Cui, J. Li, C. Yuan, and Z. Liu, "Numerical simulation of mould erosion in sand casting based on a modified shear stress model," *Journal of Materials Processing Technology*, vol. 254, pp. 341–352, 2018.

[59] J. G. Sylvia, *Cast Metals Technology*, Des Plaines, IL: American Foundrymen's Society, 1972.

[60] M. R. Barkhudarov and C. W. Hirt, "Tracking defects in castings with simulation," *Foundry Management & Technology*, vol. 126, no. 8, pp. 42–46, 1998.

[61] ASME, *Standard for Verification and Validation in Computational Fluid Dynamics and Heat Transfer*, ASME V&V 20-2009, 2009.

[62] I. B. Celik, U. Ghia, P. J. Roache, C. J. Freitas, H. Coleman, and P. E. Raad, "Procedure for Estimation and Reporting of Uncertainty Due to Discretization in CFD Applications," *Journal of Fluids Engineering*, vol. 130, no. 7, 2008, Art. no. 078001.

[63] P. J. Roache, "Perspective: A Method for Uniform Reporting of Grid Convergence Studies," *Journal of Fluids Engineering*, vol. 116, no. 3, pp. 405–413, 1994.

[64] M. R. Barkhudarov, "Erosion Model for Flow-3D," Flow Science Inc., Santa Fe, NM, Tech. Note FSI-04-TN64, 2004.

[65] H. Hu, S. X. Long, and H. L. Tsai, "Numerical simulation of mould filling in casting processes," *Journal of Materials Processing Technology*, vol. 139, no. 1–3, pp. 89–95, 2003.

[66] F. M. White, *Fluid Mechanics*, 7th ed. New York: McGraw-Hill, 2011.

[67] B. R. Munson, D. F. Young, T. H. Okiishi, and W. W. Huebsch, *Fundamentals of Fluid Mechanics*, 7th ed. Hoboken, NJ: Wiley, 2013.

Appendix A: Models and Raw Transient Datasets

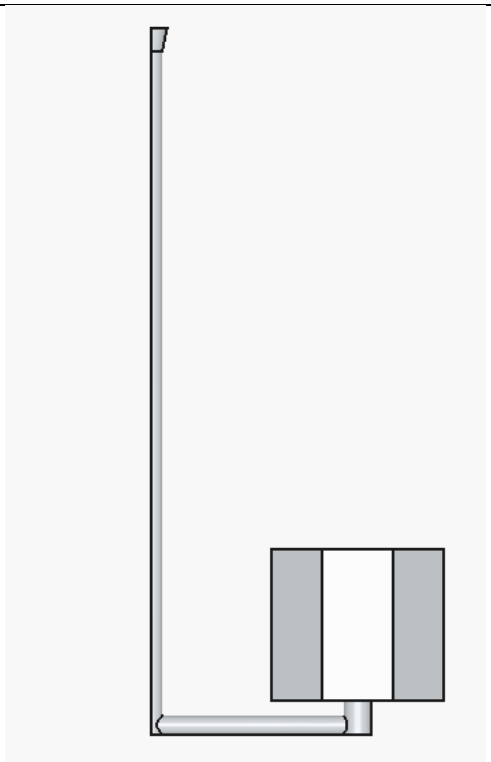

Image A.1 Side view of the 90° Runner Model.

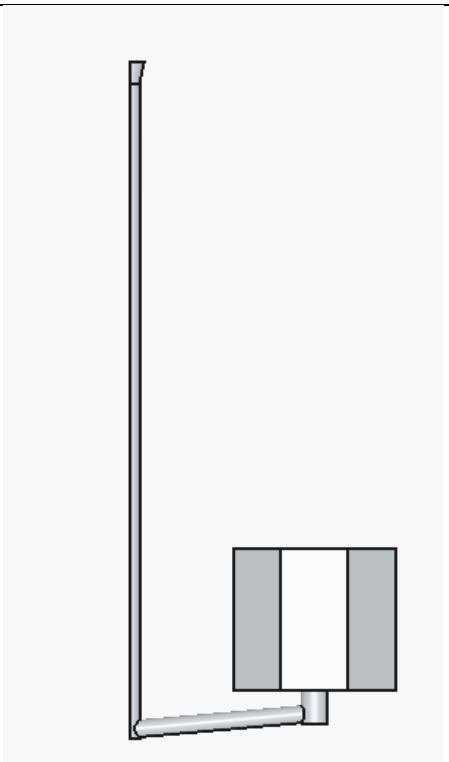

Image A.2 Side view of the 85° Runner Model.

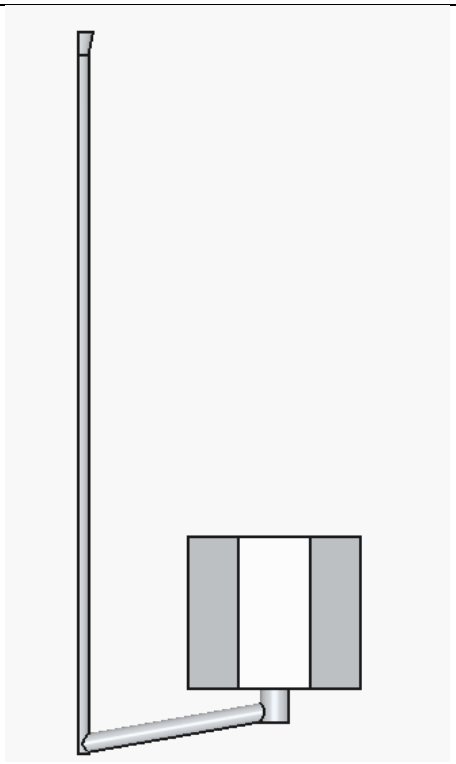

Image A.3 Side view of the 80º Runner Model.

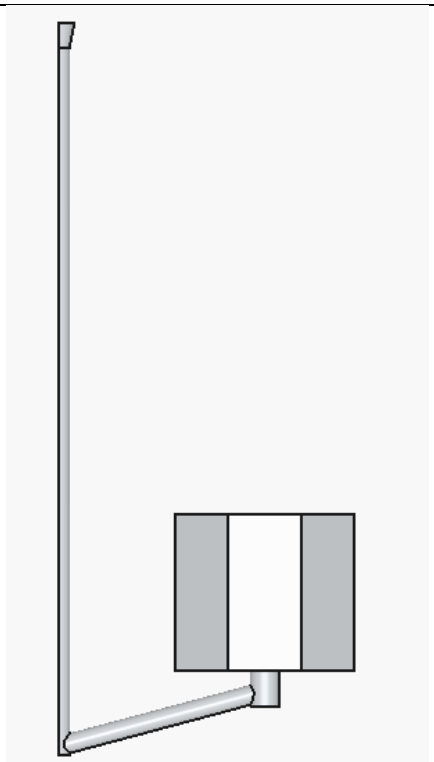

Image A.4 Side view of the 75º Runner Model.

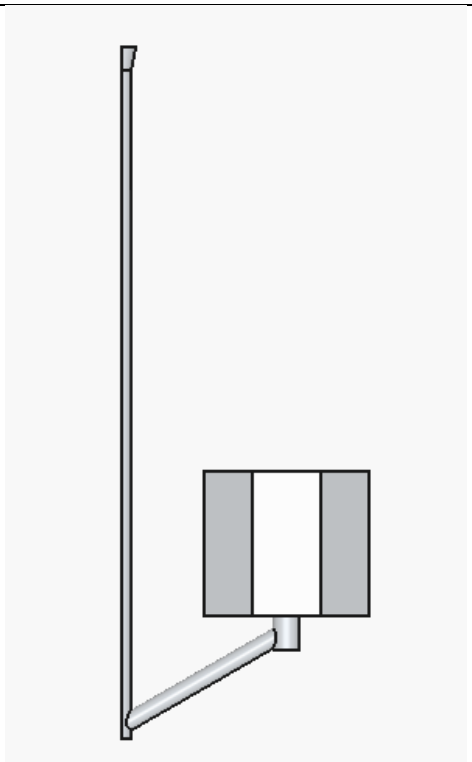

Image A.5 Side view of the 60º Runner Model.

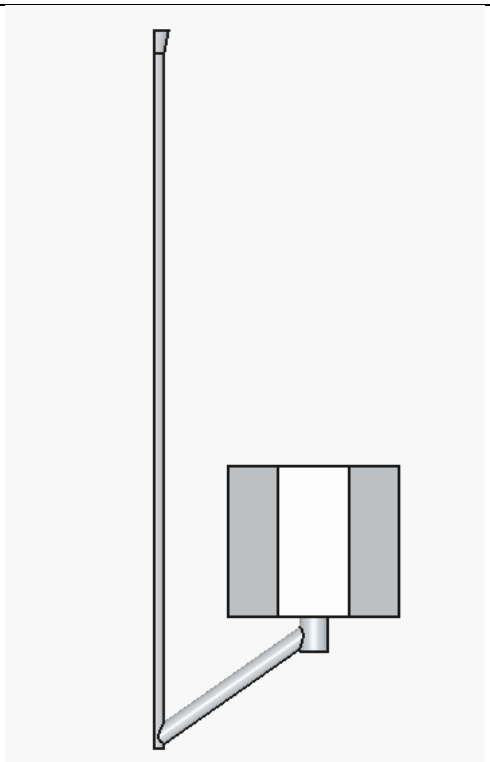

Image A.6 Side view of the 55º Runner Model.

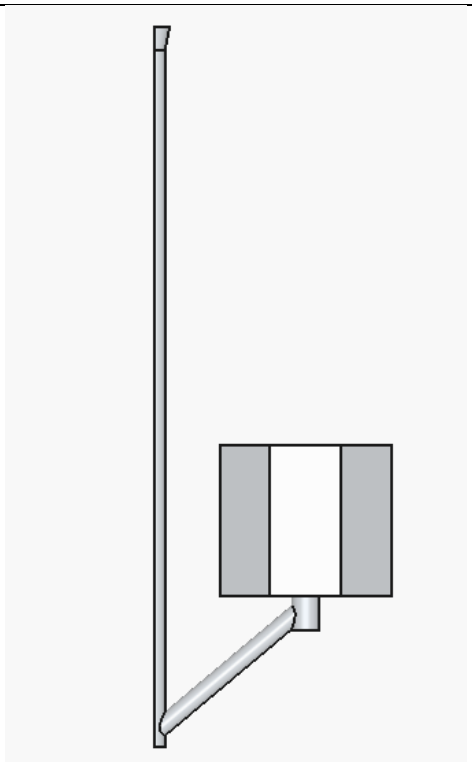

Image A.7 Side view of the 50º Runner Model.

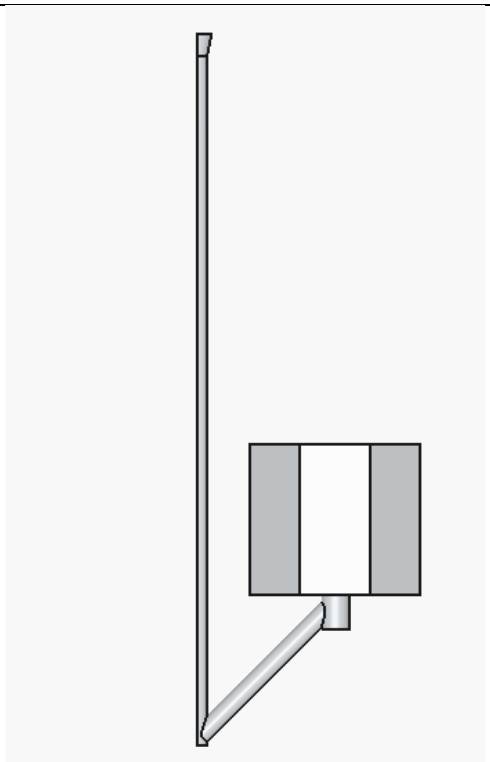

Image A.8 Side view of the 45º Runner Model.

A.1 Table Template and Common Vector Metrics

For all geometric variants, data points were extracted at matching stationary reference fill volumes (V_{ref}) rather than uniform time increments to isolate pure geometric acceleration from mass flow accumulation.

Table A.1: Transient Filling Metrics for the 90° Perpendicular Baseline Model

Volume (m3)	M1 (mm)	M2 (mm)	M4 (mm)	Exit Angle (°)	Max Wall shear stress (Pa)	Dead Zone (%)	Air Pct (%)
0.0137	99.86	159.84	284.76	90	0	75	46.25
0.0182	95.42	155.4	274.9	−3.50	36.84	61.03	46.76
0.0227	91.71	181.69	294.96	−4.62	41.7	59.78	52.65
0.0311	87.37	177.26	276.43	18.66	47.24	51.34	50.81
0.0367	114.92	174.94	264.2	2.12	44.24	54.36	42.41
0.0406	104.91	194.93	285.64	47.87	49.05	51.37	47.94

0.0495	98.46	158.47	236.06	22.58	36.98	48.52	46.26
0.0544	89.54	179.53	255.17	40.4	48.7	52.63	46.84
0.0577	115.58	175.58	247.9	16.7	43.13	54.54	45.5

A.2 Modified Angle: 85° Runner Configuration

Table A.2: Transient Filling Metrics for the 85° Runner Model

Volume (m3)	M1 (mm)	M2 (mm)	M4 (mm)	Exit Angle (°)	Max WSS (Pa)	Dead Zone (%)	Air Pct (%)
0.0134	94.57	154.6	280.55	20.4	0	72.6	38.64
0.0182	92.73	182.73	299.92	42.93	24.37	61.65	32.86
0.0222	89.51	179.49	291.1	−16.95	28.47	60.23	34
0.0271	114.6	204.6	310.29	5.61	41.29	50.89	43.89
0.0312	111.77	171.77	271.36	79.57	66.58	53.91	39.76
0.0368	159.5	189.5	288.96	70.04	593.61	57.42	31.52
0.0407	130.74	190.74	280.42	9.83	62.28	48.27	41.54
0.045	181.72	241.72	330.87	36.21	60.77	52.11	33.16
0.0542	121.38	181.38	250.69	28.76	42.26	46.54	38.69

A.3 Modified Angle: 80° Runner Configuration

Table A.3: Transient Filling Metrics for the 80° Runner Model

Volume (m3)	M1 (mm)	M2 (mm)	M4 (mm)	Exit Angle (°)	Max WSS (Pa)	Dead Zone (%)	Air Pct (%)
0.0135	119.21	209.21	340.18	2.78	300.76	56.61	32.61
0.019	117.05	207.05	328.24	17.52	489.86	55.65	25.02
0.0229	144.63	204.63	319.51	27.32	161.54	49.86	29.19
0.0278	136.68	226.68	338.74	35.86	135.72	44.36	29.99
0.032	193.21	283.21	389.53	8.2	597.77	43.19	33.61
0.036	153.76	243.76	350.66	7.7	757.34	45.94	36.54
0.0407	178.24	238.24	340.32	68.69	582.38	41.16	35.55

0.0456	141.01	201.01	299.63	50.74	466.23	51.13	40.12
0.0497	137.84	197.84	290.54	55.38	393.54	52.05	10.8

A.4 Modified Angle: 75° Runner Configuration

Table A.4: Transient Filling Metrics for the 75° Runner Model

Volume (m3)	M1 (mm)	M2 (mm)	M4 (mm)	Exit Angle (°)	Max WSS (Pa)	Dead Zone (%)	Air Pct (%)
0.0133	126.87	216.86	355.72	34.24	819.98	56.46	34.53
0.0181	152.41	242.41	375.08	77.1	1049.75	50.13	35.74
0.0226	147.8	177.8	305.25	47.87	861.43	46.05	35.99
0.0228	138.63	228.63	364.86	25.67	1347.47	40.1	34.11
0.0318	133.84	193.84	315.05	28.74	1312.97	37.74	33.19
0.0367	125.46	185.46	304.13	23.59	970.98	37.3	32.26
0.0405	152.48	212.48	325.89	19.59	1044.82	35.32	15.59
0.0453	150.81	180.81	285.29	39.02	1077.12	34.86	14.45
0.0494	147.25	177.25	276.12	23.91	1172.62	35.37	13.27

A.5 Modified Angle: 60° Runner Configuration

Table A.5: Transient Filling Metrics for the 60° Runner Model

Volume (m3)	M1 (mm)	M2 (mm)	M4 (mm)	Exit Angle (°)	Max WSS (Pa)	Dead Zone (%)	Air Pct (%)
0.0131	209.15	269.15	401.23	58.54	0	56.16	16.07
0.0187	204	249	373.86	51.93	865.13	60.28	28.85
0.0225	169.97	229.97	350.43	34.98	644.73	49.08	30.7
0.0274	165.99	225.99	339.6	36.39	592.26	45.58	24.96
0.0313	160.98	220.98	330.97	39.83	539.58	40.71	27.12
0.0362	157.28	217.28	320.27	25.51	361.1	37.51	21.15
0.0401	151.08	211.08	311.65	17.68	607.11	36.19	22.01

0.0456	174.65	204.65	299.5	21.28	1197.9	34.92	26.94
0.0489	172.17	232.17	322.26	23.93	780.09	33.67	28.38

A.6 Modified Angle: 55° Runner Configuration

Table A.6: Transient Filling Metrics for the 55° Runner Model

Volume (m3)	M1 (mm)	M2 (mm)	M4 (mm)	Exit Angle (°)	Max WSS (Pa)	Dead Zone (%)	Air Pct (%)
0.0133	175.88	310.88	425.77	54.79	629.05	66.81	24.89
0.0186	135.43	225.43	339.09	48.9	482.31	65.69	20.67
0.0227	127.25	187.26	300.07	59.14	856.64	52.73	21.7
0.0276	146.57	206.57	319.11	46.91	1763.11	44.07	33.43
0.0311	163.93	238.93	341.48	54.46	738.7	41.61	23.46
0.0376	165.88	180.88	282.23	70.31	711.42	40	29.15
0.0406	152.69	182.69	290.58	70.8	892.67	38.23	30.54
0.0452	181.88	226.88	340.34	38.42	1012.15	37.07	10.98
0.0498	194.6	224.6	330.3	52.71	833.65	37.04	13.06

A.7 Modified Angle: 50° Runner Configuration

Table A.7: Transient Filling Metrics for the 50° Runner Model

Volume (m3)	M1 (mm)	M2 (mm)	M4 (mm)	Exit Angle (°)	Max WSS (Pa)	Dead Zone (%)	Air Pct (%)
0.0139	149.78	239.77	359.44	59.21	0	72.45	29.98
0.0181	145.37	205.36	320.13	15.68	477.91	75.3	37.7
0.0224	201.7	261.7	370.58	1.66	519.47	62.81	36.14
0.0276	110.89	200.87	299.26	1.6	482.52	40.96	31.27
0.032	148.43	208.44	304.52	22.98	860.64	39.65	29.88
0.0363	161.51	221.52	310.09	10.1	325.11	38.48	20.61
0.0402	141.76	186.79	271.47	6.31	272.11	34.31	29.11

0.0456	145.41	175.42	259.6	29.8	714.91	33.15	22.63
0.0494	144.33	219.33	296.23	11.8	464.15	31.17	19.35

A.8 Modified Angle: 45° Runner Configuration

Table A.8: Transient Filling Metrics for the 45° Runner Model

Volume (m3)	M1 (mm)	M2 (mm)	M4 (mm)	Exit Angle (°)	Max WSS (Pa)	Dead Zone (%)	Air Pct (%)
0.0132	175.69	235.69	350.93	35.45	593.22	71.08	45.88
0.0183	197.55	242.55	354.69	14.89	533.6	58.58	38.17
0.0227	166.65	196.65	300.02	3.26	741.35	46.59	34.23
0.0276	163.51	238.51	334.2	3.22	416.73	39.34	32.28
0.0316	173.95	248.95	340.39	5.43	641.41	37.1	21.32
0.0361	161.38	206.38	285.58	14.15	714.43	33.79	22.16
0.0404	157.99	187.99	260.94	17.22	729.9	31.21	23.27
0.0456	183.11	228.11	294.5	14.48	442.53	30.18	25.82
0.0493	182.08	197.08	256.31	20.44	531.19	29.38	26.07

Appendix B: Raw Transient Datasets – Velocity Sensitivity Suite

B.1 Transient Filling Metrics at a Reduced Velocity of 1.5 m/s

Table B.1: Transient Filling Metrics for the 90° Runner Model at a Reduced Velocity of 1.5 m/s

Volume (m3)	M1 (mm)	M2 (mm)	M4 (mm)	Exit Angle (°)	Max WSS (Pa)	Dead Zone (%)	Air Pct (%)
0.0136	101.51	161.61	284.98	90	0	0	58.52
0.0185	99.03	159.13	274.14	90	0	0	69.71
0.023	94.79	154.86	264.38	90	0	0	64.85
0.0272	87.03	177.1	285.01	90	0	0	58.48
0.0315	83.69	173.76	275.65	13.92	25.28	68.82	57.52

0.0363	79.76	169.65	265.11	−23.00	33.89	62.14	62
0.0406	74.9	194.75	285.67	26.33	31.16	56.18	52.95
0.0453	101.31	191.32	275.24	−13.68	26.07	69.08	55.81
0.0506	96.88	186.88	263.6	52.47	22.4	71.04	57.94

B.2 Transient Filling Metrics at a Reduced Velocity of 2 m/s

Table B.2: Transient Filling Metrics for the 90° Runner Model at a Reduced Velocity of 2 m/s

Volume (m3)	M1 (mm)	M2 (mm)	M4 (mm)	Exit Angle (°)	Max WSS (Pa)	Dead Zone (%)	Air Pct (%)
0.0138	97.02	187.09	314.62	90	0	0	53.53
0.0188	91.96	182.06	303.48	−20.52	35.46	78.81	57.57
0.0221	85.99	176.06	296.26	−5.94	466.61	63.18	53.53
0.0274	83.63	143.73	254.6	18.35	40.03	56.57	48.78
0.0315	108.96	228.97	335.65	−9.45	47.16	54.45	50.59
0.0375	104.35	194.36	292.45	−2.26	36.64	63.99	55.38
0.0408	71.16	161.01	255.08	45.15	37.75	49.04	51.87
0.0451	100.78	160.8	245.75	59.44	29.01	64.56	48.2
0.0498	96.04	186.03	265.36	−5.02	23.79	53.2	54.93

B.3 Transient Filling Metrics at a baseline Velocity of 2.47 m/s

Table B.3: Transient Filling Metrics for the 90° Runner Model at baseline Velocity of 2.47 m/s

Volume (m3)	M1 (mm)	M2 (mm)	M4 (mm)	Exit Angle (°)	Max WSS (Pa)	Dead Zone (%)	Air Pct (%)
0.0137	99.86	159.84	284.76	90	0	75	46.25
0.0182	95.42	155.4	274.9	−3.50	36.84	61.03	46.76
0.0227	91.71	181.69	294.96	−4.62	41.7	59.78	52.65
0.0311	87.37	177.26	276.43	18.66	47.24	51.34	50.81
0.0367	114.92	174.94	264.2	2.12	44.24	54.36	42.41

0.0406	104.91	194.93	285.64	47.87	49.05	51.37	47.94
0.0495	98.46	158.47	236.06	22.58	36.98	48.52	46.26
0.0544	89.54	179.53	255.17	40.4	48.7	52.63	46.84
0.0577	115.58	175.58	247.9	16.7	43.13	54.54	45.5

B.4 Transient Filling Metrics at increased Velocity of 3 m/s

Table B.4: Transient Filling Metrics for the 90° Runner Model at increased Velocity of 3 m/s

Volume (m3)	M1 (mm)	M2 (mm)	M4 (mm)	Exit Angle (°)	Max WSS (Pa)	Dead Zone (%)	Air Pct (%)
0.0135	156.44	231.44	375.32	90	0	0	40.45
0.0184	148.93	238.93	364.55	90	0	0	35.05
0.0226	85.26	145.15	265.33	90	0	0	42.55
0.0273	113.63	203.64	314.8	90	0	0	39.05
0.0312	110.23	170.25	276.36	−5.34	56.21	38.75	39.12
0.037	104.19	194.19	293.61	0.62	62.86	38.26	44.96
0.0406	101.33	191.33	285.54	4.97	58.4	40.24	42.86
0.0452	95.99	185.97	275.53	3.89	52.48	38.86	39.95
0.0497	121.96	181.96	265.51	−18.53	58.37	41.27	43.49

B.5 Transient Filling Metrics at increased Velocity of 3.5 m/s

Table B.5: Transient Filling Metrics for the 90° Runner Model at increased Velocity of 3.5 m/s

Volume (m3)	M1 (mm)	M2 (mm)	M4 (mm)	Exit Angle (°)	Max WSS (Pa)	Dead Zone (%)	Air Pct (%)
0.0144	114.57	174.56	313.37	75.85	686.09	69.5	31.21
0.0182	204.67	264.67	394.89	70.86	745.55	67.62	31.14
0.0216	150.13	180.13	297.38	74.18	740.03	67.58	32.59
0.0276	117.21	207.21	314.19	44.9	146.12	45.08	31.5
0.0317	172.87	232.87	335.21	−1.65	728.44	42.99	34.71

0.0368	135.04	195.04	293.96	15.42	649.31	42.99	30.2
0.04	132.58	192.58	286.86	37.72	745.81	39.62	29.44
0.0458	153.43	213.43	304.17	17.18	610.49	36.59	44.35
0.0503	113.91	173.91	264.1	9.24	114.43	37.77	16.69

B.6 Transient Filling Metrics at increased Velocity of 4 m/s

Table B.6: Transient Filling Metrics for the 90° Runner Model at increased Velocity of 4 m/s

Volume (m3)	M1 (mm)	M2 (mm)	M4 (mm)	Exit Angle (°)	Max WSS (Pa)	Dead Zone (%)	Air Pct (%)
0.0141	338.21	398.21	553.89	16.14	780.17	65.77	22.76
0.0182	113.1	203.1	334.91	47.41	877.74	65.84	18.54
0.0223	167.39	238.19	355.83	71.56	423.59	63.48	18.81
0.0278	170.85	230.85	343.72	7.28	773.81	47.52	21.48
0.0315	105.46	165.46	275.72	−7.57	751.74	44.97	17.12
0.0363	164.49	224.49	324.99	27.45	933.79	44.55	16.11
0.0403	185	245	346.29	54.13	514.18	40.65	25.03
0.0455	117.5	177.5	274.73	30.71	764.76	40.83	16.13
0.0501	172.16	232.16	324.72	48.36	760.09	36.71	7.5

Appendix C: Computational Post-Processing and Metric Extraction Methodology

To ensure complete computational transparency and reproducibility, this section documents the mathematical filtering algorithms and automated Python/ParaView extraction logic used to compute each performance metric from the raw OpenFOAM multiphase fields.

C.1 Domain Isolation Framework

Before evaluating any fluid metrics, the computational domain was strictly partitioned to isolate internal mould physics from the runner system using a spatial coordinate boundary mask:

$$\Omega_{mould} = \{(x, y, z)\ \Omega \subset \mid x \geq 0.4\ mm\}$$

Any cells or points located below this coordinate plane ($x < 0.4$ mm) were dropped from the active array to prevent runner flow profiles from altering mould metrics.

C.2 Mathematical Isolation of Performance Metrics

1. Free-Surface Topography (M1, M2 and M4)

The phase interface location was tracked using the Volume of Fluid (VOF) phase indicator field (α_{metal}). The free-surface boundary layer was isolated using a strict intermediate contour array range:

$$\Omega_{interface} = \{x \in \Omega_{mould}\} \text{ middle}| \ 0.05 < \alpha_{metal}(x) < 0.95\}$$

M1 Metric (Perimeter Peak Height): Calculated by extracting the 99th percentile of the vertical coordinate array (z) within $\Omega_{interface}$ to filter out unphysical single-cell numerical spray artifacts.

M2 Metric (Core Interface Height): Evaluated as the spatial arithmetic mean height (*z) of the isolated interface boundary:

$$*z = 1/N \sum \{x \in \Omega_{interface}\} \ z(x)$$

M4 Metric (Transient Jet Splashing Overshoot): Calculated by measuring the absolute maximum coordinate peak of the interface array against the theoretical planar fill height (H_{theo}) dictated by total mass conservation:

$$M4 = z_{max}(\Omega_{interface}) - H_{theo}$$

2. Boundary Layer Interaction (Max WSS)

Because wall shear stress maps are not outputted natively by OpenFOAM's default multi-phase solver pipelines, a local turbulence evaluation loop was executed across the solid boundary faces (A_{walls}). The active liquid phase interface was masked where $\alpha_{metal} \geq 0.9$ to isolate true fluid friction:

$$\tau_w = \max (0.3 \times \rho_{metal}\} \times k) \ \forall \ x \in A_{walls} \cap \{\alpha_{metal} \geq 0.9\}$$

Where $\rho_{metal} = 7000$ kg/m³ and k represents local Turbulent Kinetic Energy (m²/s²).

3. Circulation Efficiency (Dead Zone %)

The dead zone calculation tracks the total volume fraction of developed liquid metal that has stalled below operational mixing parameters. It isolates the pure metal core ($\alpha_metal \geq 0.9$) and computes the cell-volume-weighted percentage of components falling below a critical velocity threshold:

$$\text{Dead Zone [\%]} = \sum V_i \cdot I(|U_i| < 0.05 \text{ m/s}) / \sum V_i \} \times 100 \; \forall \; i \in \{\alpha_{metal} \geq 0.9\}$$

Where V_i is individual cell volume, $|U_i|$ is velocity magnitude, and I is a binary indicator function matching the condition.

4. Cleanliness Risks (Air Entrainment %)

Air entrainment tracks air pockets trapped deep beneath the active fluid surface. The algorithm filters cells located spatially below a safety distance (50 mm) relative to the current mean free-surface height (z*) and measures the volume fraction where air content dominates ($\alpha_{metal} < 0.5$):

$$\text{Air Pct [\%]} = \{\sum V_j \cdot I\,(\alpha_metal, j\} < 0.5)\} \; \{\sum V_j\} \times 100 \; \forall \; j \in \{z_j < (\{z\} - 0.05 \text{ m})\}$$

C.3 Automated Python Extraction Script Example

The automated python routine utilized to batch-process the export data frames is provided below:

```
# Appendix C.3: Automated Metric Processing Script Snippet

import pandas as pd

import numpy as np


def process_simulation_appendix_dataframe(csv_filepath, theoretical_vol, mold_area=0.454):
```

```
df = pd.read_csv(csv_filepath)

# Apply Mold Spatial Mask (X >= 0.4m)
mold = df[df['Points_0'] >= 0.4].copy()

# Phase Classification
metal = mold[mold['alpha.Metal'] >= 0.9]
interface = mold[(mold['alpha.Metal'] > 0.05) & (mold['alpha.Metal'] < 0.95)]

# Calculate Mean and Baseline Height Reference
avg_z = interface['Points_2'].mean() if not interface.empty else 0
h_theo = (theoretical_vol / mold_area) * 1000  # Convert to mm

# Extract Topography Parameters
m1 = interface['Points_2'].quantile(0.99) * 1000 if not interface.empty else 0
m3 = m1 - (avg_z * 1000)
m4 = (interface['Points_2'].max() * 1000) - h_theo if not interface.empty else 0

# Extract Kinetic and Friction Parameters
max_wss = (0.3 * metal['rho'] * metal['k']).max() if not metal.empty else 0
dead_zone_pct = (len(metal[metal['U_Magnitude'] < 0.05]) / len(metal)) * 100 if not metal.empty else 0

return {
    "H_theo": h_theo, "M1": m1, "M3": m3, "M4": m4,
    "Max_WSS": max_wss, "Dead_Zone": dead_zone_pct
}
```

Appendix D: Graphical Compendium of Transient Hydrodynamic Simulations

D.1 Metrics vs Volume graphs for different angled runners

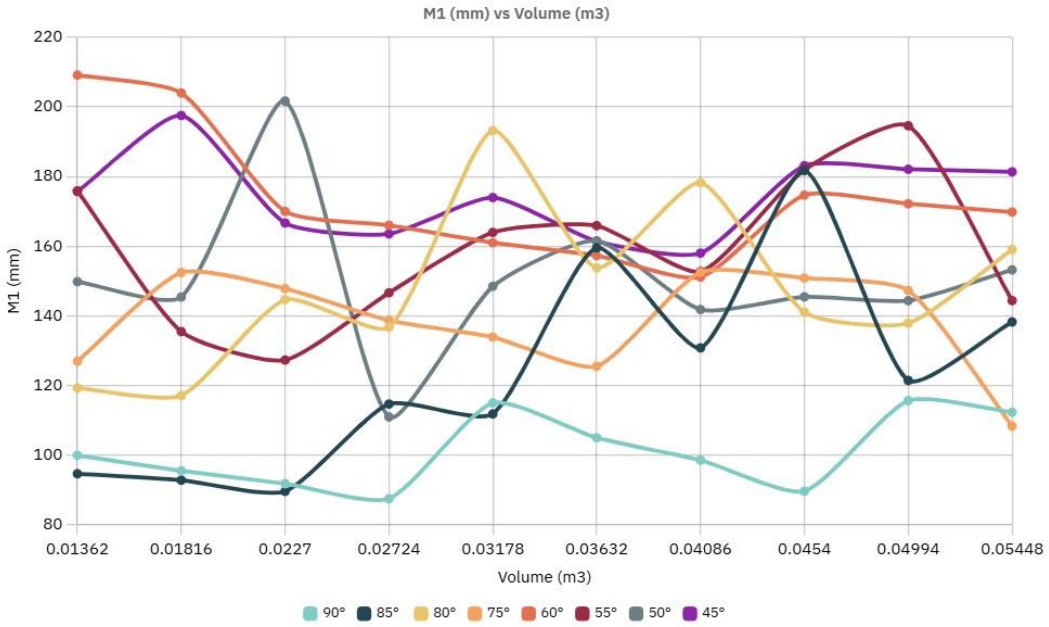

Graph D1: M1 vs Volume

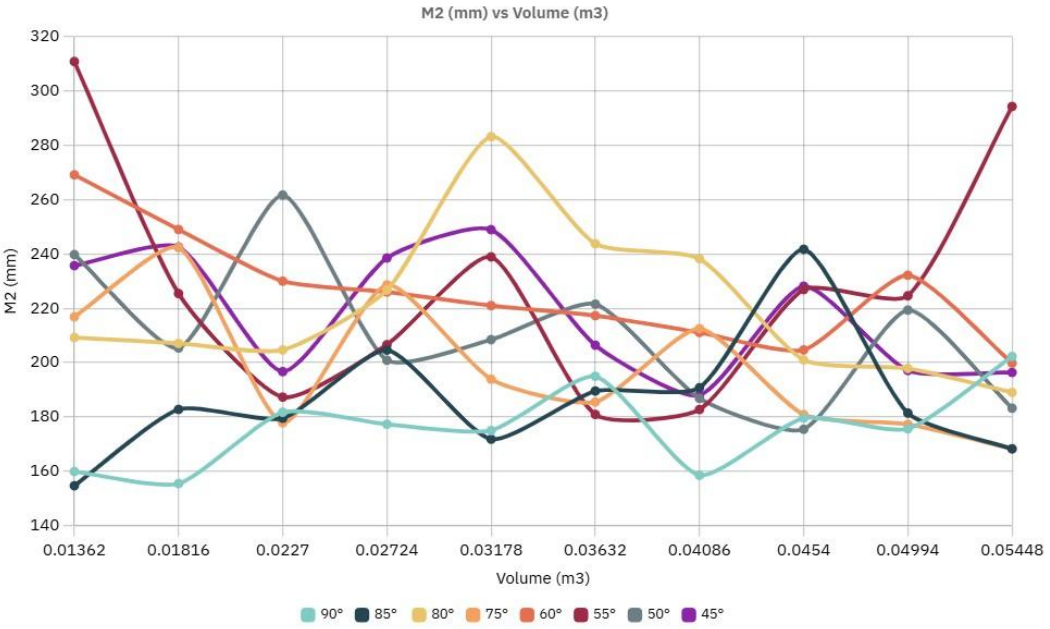

Graph D2: M2 (mm) vs Volume (m^3)

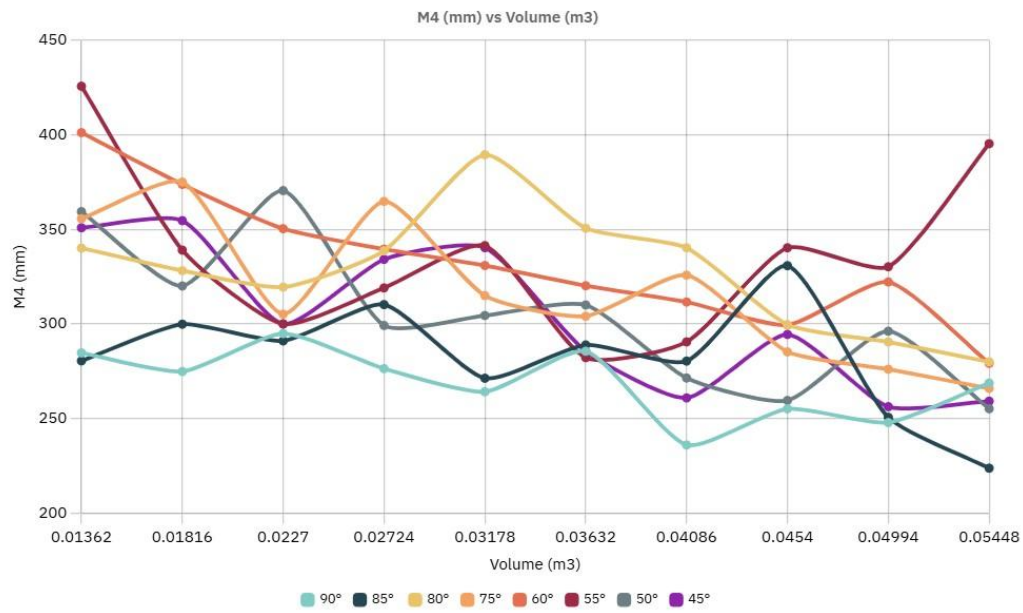

Graph D3: M4 (mm) vs Volume (m^3)

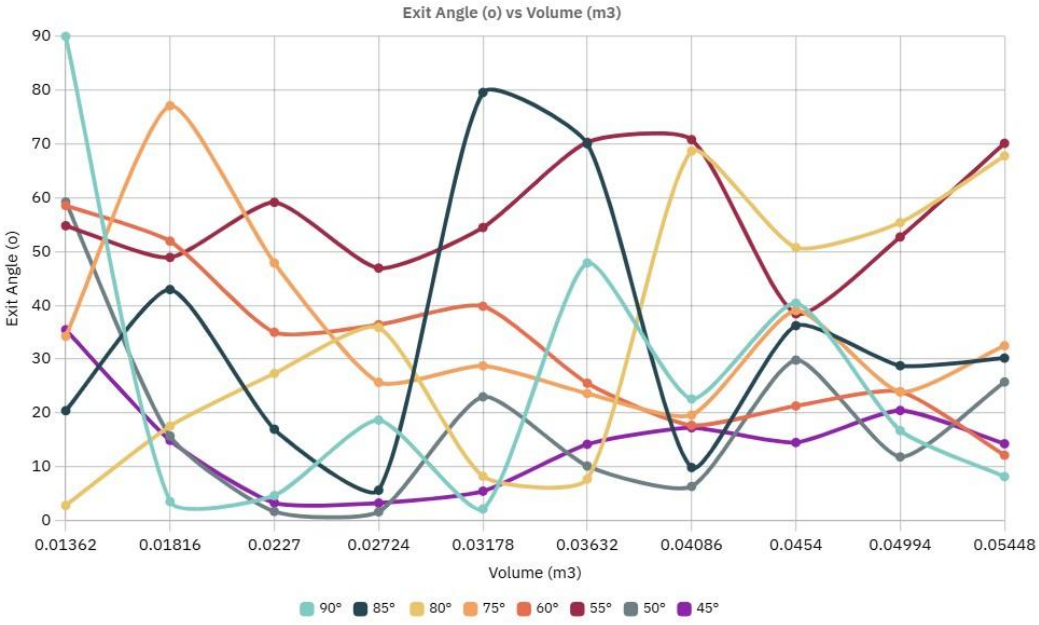

Graph D4: Exit Angle (^{o}) vs Volume (m^3)

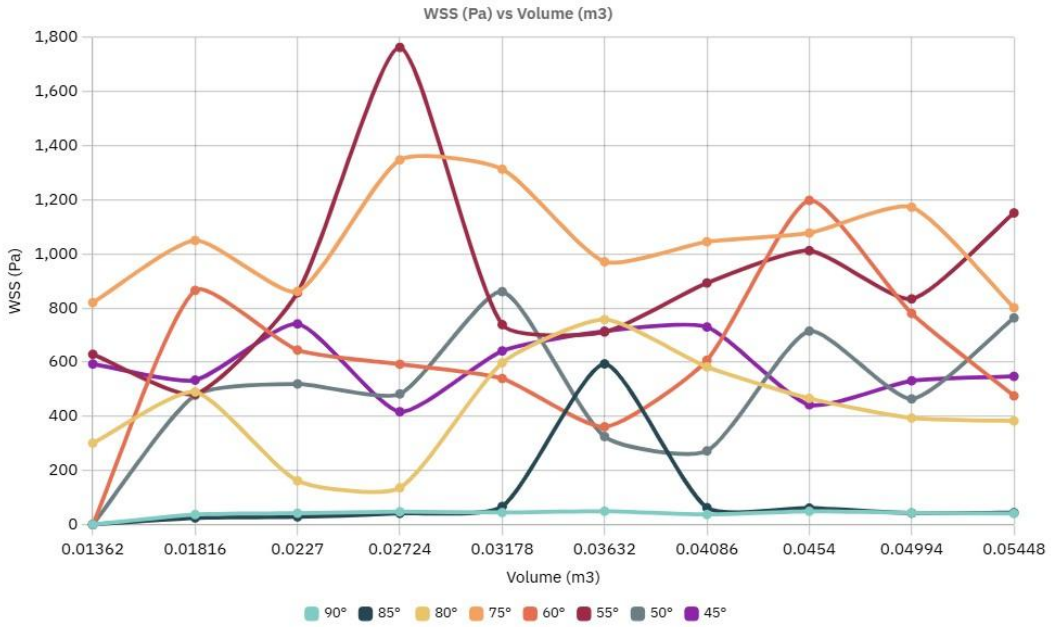

Graph D5: Wall Shear Stress (Pa) vs Volume (m^3)

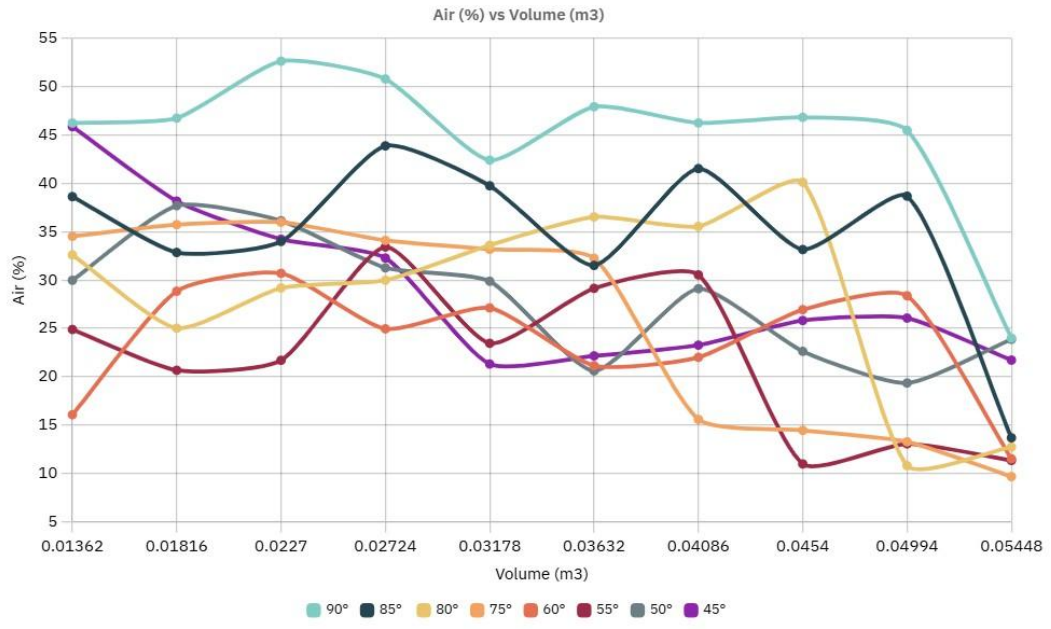

Graph D6: Air (%) vs Volume (m^3)

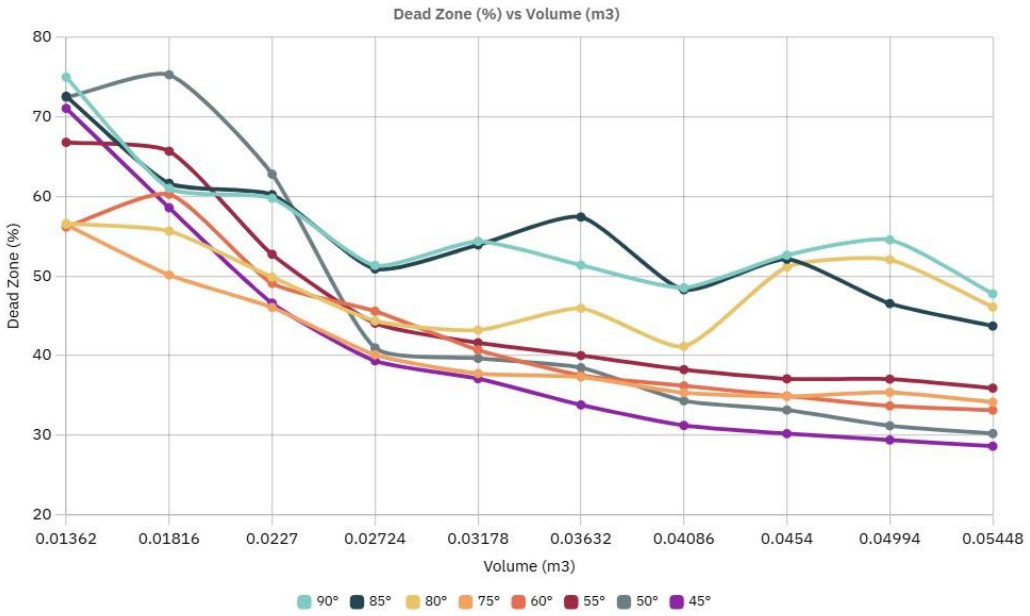

Graph D7: Dead Zone (%) vs Volume (m^3)

D2. Metrics vs volume for different Inlet Velocities

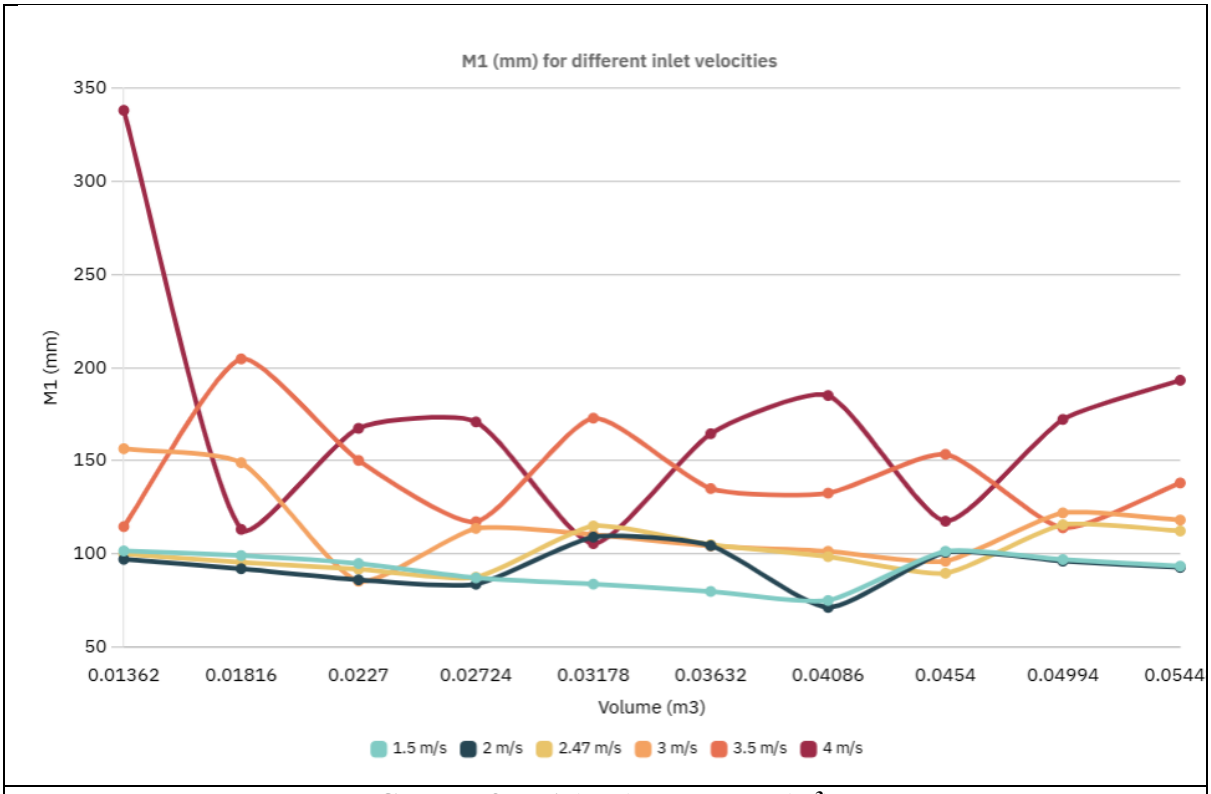

Graph D8: M1 (mm) vs Volume (m^3)

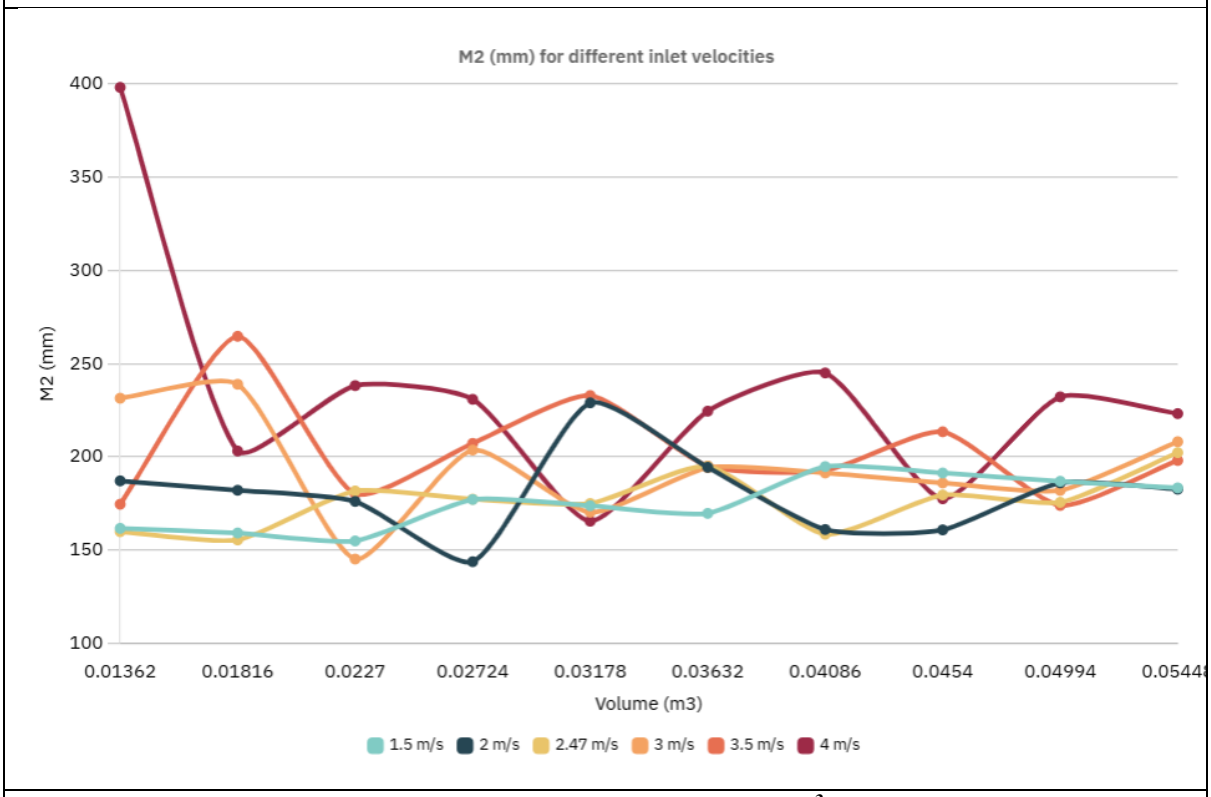

Graph D9: M2 (mm) vs Volume (m^3)

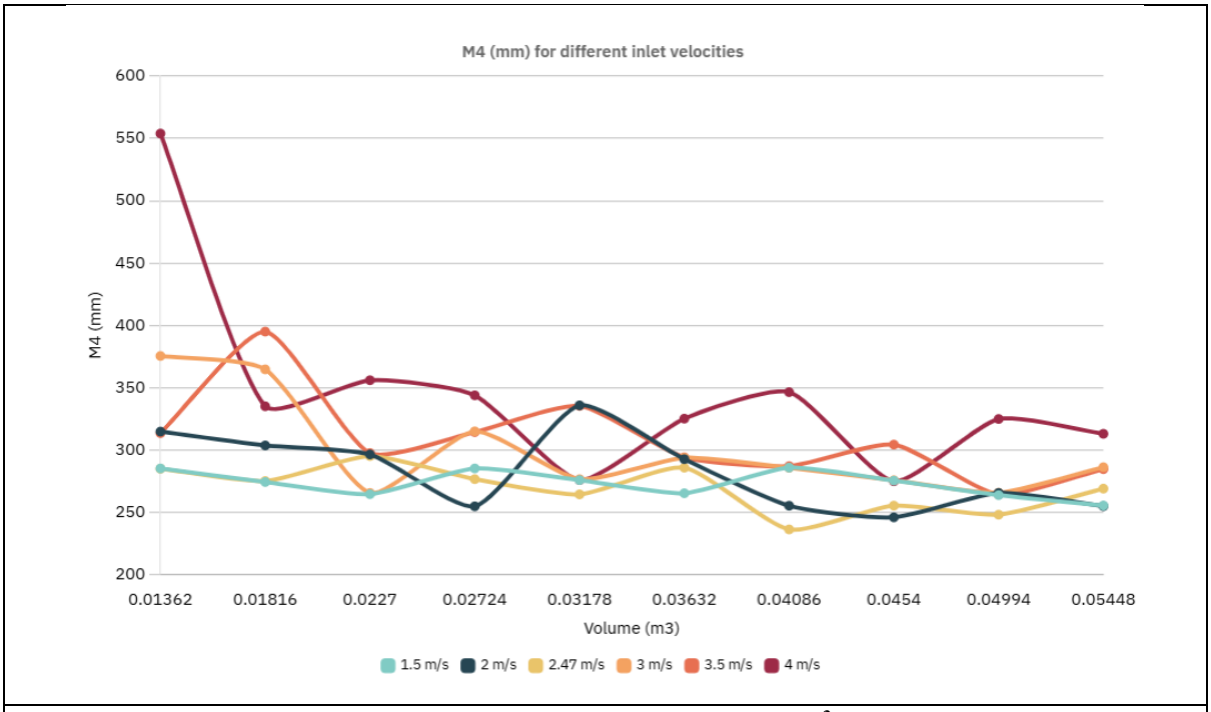

Graph D10: M4 (mm) vs Volume (m^3)

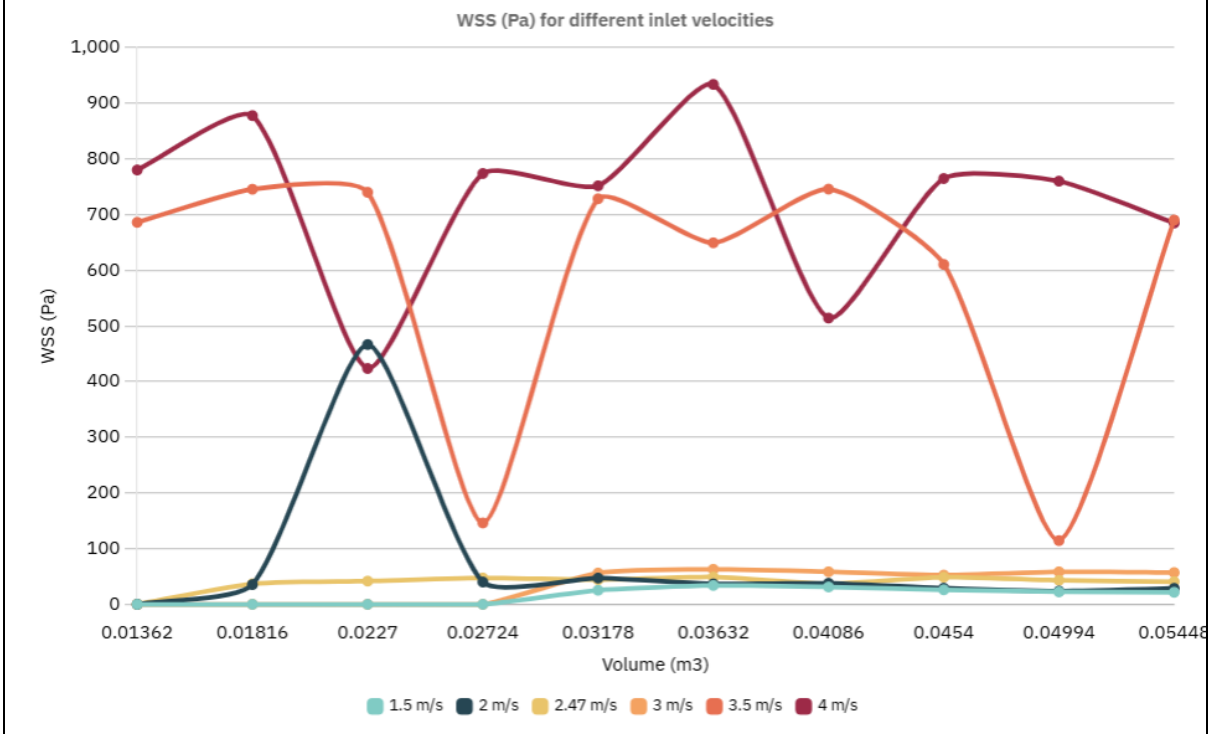

Graph D11: Wall Shear Stress (Pa) vs Volume (m^3)

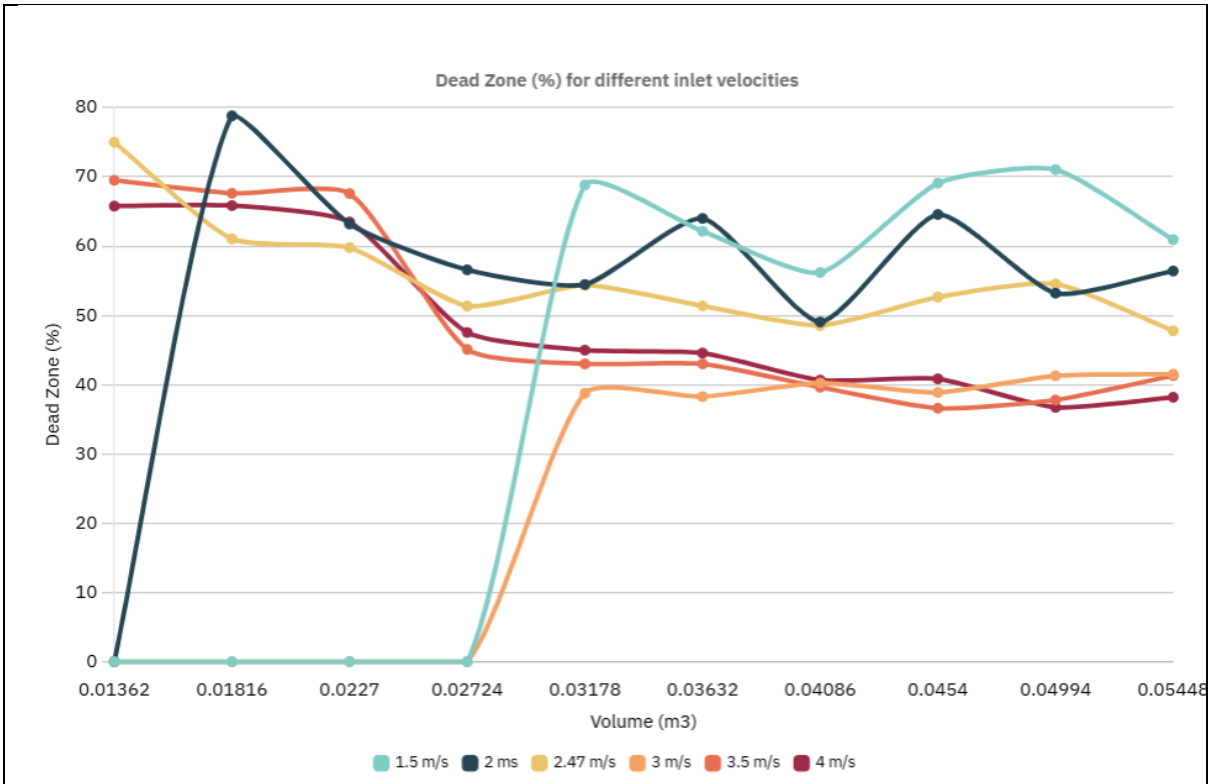

Graph D12: Dead Zone (%) vs Volume (m^3)

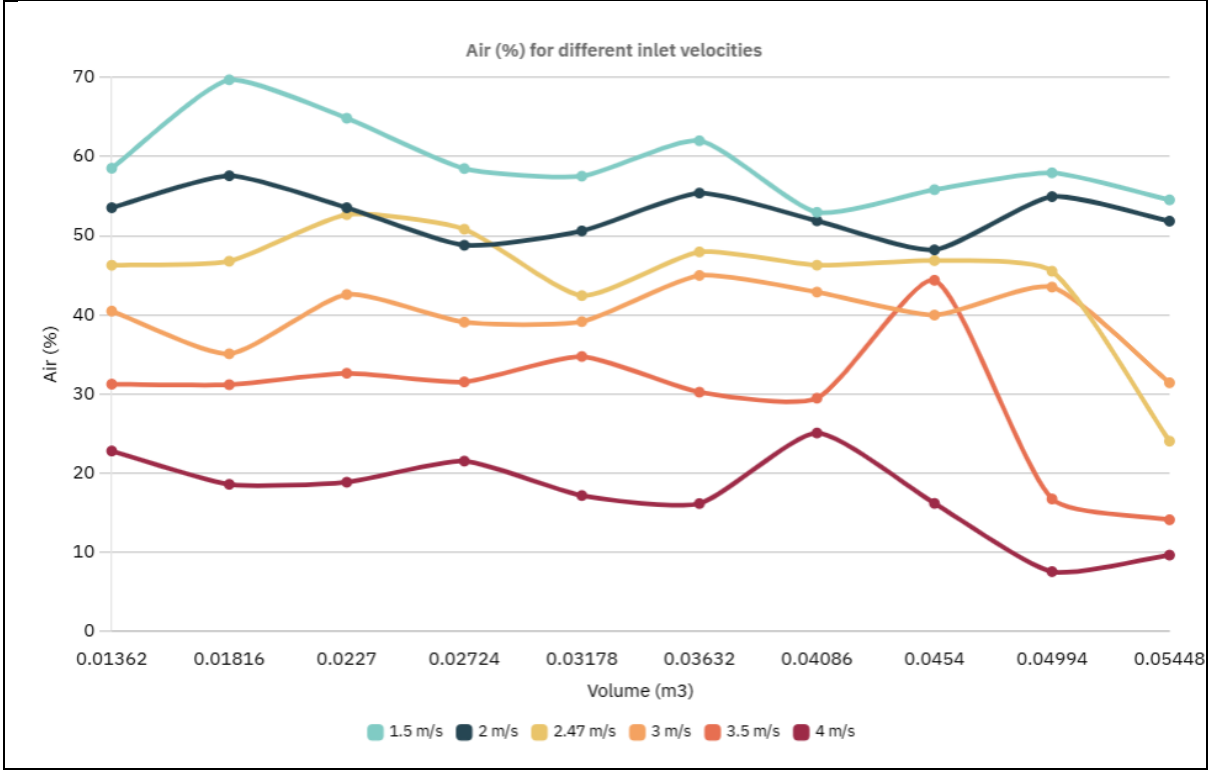

Graph D13: Air (%) vs Volume (m^3)